

See discussions, stats, and author profiles for this publication at: <https://www.researchgate.net/publication/276294882>

Metal-assisted chemical etching of silicon and the behavior of nanoscale silicon materials as Li-ion battery anodes

ARTICLE *in* NANO RESEARCH · MARCH 2015

Impact Factor: 7.01 · DOI: 10.1007/s12274-014-0659-9

CITATIONS

4

READS

60

3 AUTHORS:



William Mcsweeney
University College Cork

9 PUBLICATIONS 23 CITATIONS

[SEE PROFILE](#)



Hugh Geaney
University College Cork

41 PUBLICATIONS 579 CITATIONS

[SEE PROFILE](#)



Colm O'Dwyer
University College Cork

166 PUBLICATIONS 1,484 CITATIONS

[SEE PROFILE](#)

Metal-assisted chemical etching of silicon and the behavior of nanoscale silicon materials as Li-ion battery anodes

William McSweeney^{1,2,3,4}, Hugh Geaney^{1,4}, and Colm O'Dwyer^{1,4} (✉)

¹Department of Chemistry, University College Cork, Cork, Ireland

²Department of Physics and Energy, University of Limerick, Limerick, Ireland

³Materials and Surface Science Institute, University of Limerick, Limerick, Ireland

⁴Micro & Nanoelectronics Centre, Tyndall National Institute, Lee Maltings, Cork, Ireland

Received: 27 August 2014

Revised: 26 November 2014

Accepted: 30 November 2014

© Tsinghua University Press
and Springer-Verlag Berlin
Heidelberg 2014

KEYWORDS

silicon,
Li-ion battery,
nanostructures,
nanowires,
electrochemistry,
energy storage,
etching

ABSTRACT

This review outlines the developments and recent progress in metal-assisted chemical etching of silicon, summarizing a variety of fundamental and innovative processes and etching methods that form a wide range of nanoscale silicon structures. The use of silicon as an anode for Li-ion batteries is also reviewed, where factors such as film thickness, doping, alloying, and their response to reversible lithiation processes are summarized and discussed with respect to battery cell performance. Recent advances in improving the performance of silicon-based anodes in Li-ion batteries are also discussed. The use of a variety of nanostructured silicon structures formed by many different methods as Li-ion battery anodes is outlined, focusing in particular on the influence of mass loading, core–shell structure, conductive additives, and other parameters. The influence of porosity, dopant type, and doping level on the electrochemical response and cell performance of the silicon anodes are detailed based on recent findings. Perspectives on the future of silicon and related materials, and their compositional and structural modifications for energy storage via several electrochemical mechanisms, are also provided.

1 Introduction

Lithium-ion batteries (LIBs) typically consist of an anode, a cathode, and an electrolyte, with a separator electronically separating the anode and cathode. Upon charging of the battery, lithium (Li) ions are extracted

from the cathode and stored in the anode. When the battery is being discharged, the Li ions are extracted from the anode and stored in the cathode. One of the major benefits of this process is that it can be repeated, allowing the development of rechargeable batteries. LIBs have benefits over other electrochemical energy

Address correspondence to c.odwyer@ucc.ie

storage processes, such as supercapacitors, since they provide high energy density as well as high power density [1–3]. Silicon (Si) has attracted much research interest owing to its applications in integrated circuits, solar cells, and now as an anode material for next-generation LIBs. However, bulk Si pulverizes upon Li insertion and extraction as a result of large volume changes and mechanical stresses within the Si associated with the accommodation of a large amount of Li-ions [4].

Nanostructured Si has been investigated as a possible solution to the pulverization of Si upon Li insertion and extraction. One method of fabricating nanostructured Si is metal-assisted chemical (MAC) etching, which creates Si nanowires (NWs) from a top-down process on a Si wafer. The NWs formed by MAC etching depend on parameters such as the orientation of the Si, the doping density of the Si, and the etching conditions under which the NWs are formed [5]. The performance of Si anodes for LIBs was shown to improve with the addition of carbon (C) and other elements. This article will review various topics relating to the nanostructuring of Si for LIB applications. Advances in Si property control and recent new advances in analytical methods such as single-nanostructure anode investigation, with a comparison to corresponding bulk silicon lithiation, will also be addressed. Initially, the use of MAC etching for the formation of nanostructured Si will be reviewed. This section will explore the fundamental etching processes, compare NWs formed using top-down and bottom-up approaches, before examining pore formation, orientation control, and the use of etching masks. Following this, the fundamental processes associated with the lithiation of non-nanostructured (bulk) Si will be discussed along with its performance for LIB applications. This will be followed by a thorough review of the use of Si nanostructures for LIB applications with emphasis on nanopowders, top-down- and bottom-up-grown NWs, and core-shell structures. This section will also discuss the role of conductive additives and doping in determining LIB performance, and assess future directions for silicon anode nanostructures. A particular emphasis is placed on the influence of the electronic and physical properties of silicon in addition to size reduction or

discrete compositional variation as primary drivers of modern Li-ion anode research using silicon and its derivatives.

2 Metal-assisted chemical etching of Si

The controlled formation of porosity and roughness in Si [6–8] has attracted substantial attention, and nanoscale Si in the form of nanocrystals [9], NWs, and mesoporous analogues have been successfully applied [10] to LIBs [11], photovoltaics [12], sensing [13], and optoelectronics. Si NWs can be grown using bottom-up approaches [14] in addition to top-down etching protocols, and have been shown to be effective building blocks in nanoelectronic devices [15]. Porous semiconductor formation through electrochemical and chemical means, is now very well known [10, 16–21], and the fundamental basics of electrochemical and related methods for isotropic and crystallographically controlled etching of silicon and other semiconductors have been established. The discovery of light-emitting nanoporous Si [8, 22, 23] propelled investigations into pore formation in III–V [24–30] and other group IV semiconductors [31, 32] and II–VI materials [33, 34]. The low cost and simplicity of etching routes allow Si to be fabricated with various structure-dependent properties useful in various applications in optical [35] and photovoltaic materials [36–38], micro- and optoelectronics [39, 40], and chemical and biological sensors [13, 41], owing to its biocompatibility. For thermoelectric devices based on Si [42, 43], the engineering of its structure to alter phonon dispersion via confinement, surface scattering, and other processes is useful for controlling thermal conductivity [44].

Etching can be divided into two primary types: Dry etching and wet etching. Wet etching can be simply carried out in a beaker in a fume hood within a standard laboratory, or on dedicated wet-etch benches in an industrial setting, whereas dry etching typically requires a vacuum, plasma generation, or ion optics. The cost associated with dry etching is also comparatively higher than that of wet etching. An undesirable effect of a dry etching is damage to the sidewalls of the semiconductor structures [45], which leads to degradation of carrier mobility. Dry etching does not have an in-built limiting condition

that defines and allows maximal porosity formation within a semiconductor. By comparison, wet etching using MAC etching or by potential-driven electrochemical means (which is sensitive to illumination, the redox potential, Fermi level position, doping, etc.) can allow etching to occur at higher etch rates on planes in numerous directions (for example, {100} planes in silicon) until the depletion region overlaps the limited charge transfer, thus ending the etching (in the dark), resulting in porous or nanostructured silicon. Such characteristics are useful benefits of wet etching protocols for silicon-based electrode formation.

The ability to control the morphology and shape of Si nanostructures by chemical etching in the presence of a redox couple in solution or using a metal/ion (MAC etching) [46–50] gives alternative routes toward complex Si structures, where roughness and porosity within the nanostructures contribute to exploitable properties in device development. Many MAC etching methodologies have been developed that can produce Si NWs with uniform diameters and packing densities [51, 52]. This section will introduce the MAC etching process, and it will discuss the advantages of MAC-etched Si NWs over Si NWs formed via different methodologies, as well as the influence of doping on MAC-etched Si NWs and the varying orientation of the Si NWs.

2.1 MAC etching process

MAC etching involves metal deposition on a Si substrate from a metal ion containing a HF solution. Figure 1 shows a Ag particle deposited on the Si surface prior to etching. Metal deposition in this manner is a localized chemical redox process in which both anodic and cathodic processes occur simultaneously at the Si

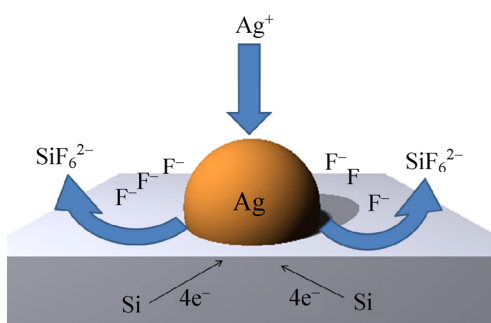


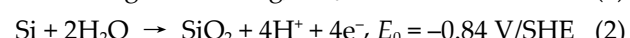
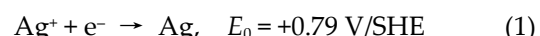
Figure 1 A schematic of the electroless metal deposition process.

surface. The major advantage associated with this method is the control over the growth direction and doping levels of the Si NWs formed—the doping level is set by the substrate growth and not graded from bulk to surface.

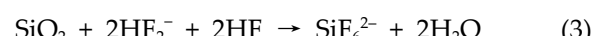
The field of MAC etching has recently been reviewed by Huang et al. [53] and Li [54], showing the interest that this subject attracts. The Si NWs produced can be tuned in length from a few nanometers to several tens of micrometers, and it has been shown that Si NWs that were MAC etched using the HF/AgNO₃ recipe have a wide diameter distribution [55] when compared to vapor–liquid–solid (VLS)-grown Si NWs [45]. The cores of these Si NWs can be single crystalline with the growth direction having a defined relationship with the surface orientation of the Si wafer used [56].

The first demonstration of MAC etching of Si was reported in 1997 [57]. Porous Si was fabricated by etching an aluminum (Al)-covered Si substrate in a HF solution. The MAC etching method was first investigated in detail by Li and Bohn [58], who found that a metal (e.g., Au or Pt) on the surface of a Si substrate catalyzed the etching of Si in a HF solution, resulting in pores or columns etched into the Si.

The cathodic reaction for Ag⁺ reduction and the anodic reaction for Si oxidation are as follows [59]



Si oxides are etched by HF and dissolved in aqueous solution



The etching mechanism proposed by Peng et al. [60] begins with the electroless deposition of Ag particles on the Si substrate. This occurs via two simultaneous electrochemical processes on the Si surface. Firstly, Ag⁺ ions close to the surface of the Si capture electrons from the valence band of the Si and are deposited in the form of Ag nuclei. Secondly, the Si directly beneath the deposited metal particles is oxidized and forms the Si hexafluoride anion (SiF₆²⁻), which is soluble in HF. The metal particles then etch through the Si and the remaining sidewalls form the Si NWs as shown in Fig. 2.

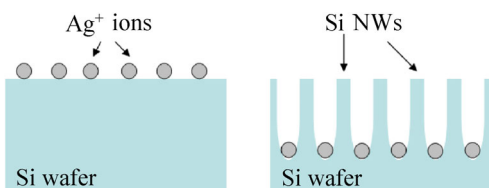


Figure 2 A schematic of Ag^+ ion etching into a Si surface, reducing to metallic Ag^0 in the process. The remaining sidewalls form the Si NWs.

It is generally believed that metal nanoparticles (NP) adhered on a Si surface with a higher electronegativity than Si can attract electrons from Si to become negatively charged (Fig. 3(a)). These metal NPs could then act as local micro-cathodes and enhance the cathodic reaction as a result of their catalytic activity [61, 62]. It has been shown that Ag has a superior etching performance over other elements (Au, Pt, Cu, or Fe) [63]. Accumulation of holes on the Si surface occurs under anodic bias and accumulation of electrons on the Si surface under cathodic bias. In the absence of a bias, band bending in the space charge region (SCR) [64], as shown in Fig. 3, pushes holes to the surface of n-type Si, whereas it pushes electrons to the surface of p-type Si. Schematics of the band diagrams at the Si-electrolyte interface are shown in Figs. 3(b) and 3(c). These schematics also illustrate the difference in the work function between the n-type Si and p-type Si with reference to the electrolyte [65].

However, MAC etching of this sort cannot be viewed as a simple redox surface reaction. As Kolasinski [65] points out, HF appears to oscillate between dissociated and undissociated forms and a contact ion pair in

which both H^+ and F^- are bound strongly on either side of a water molecule [65]. HF (aq) not only contains solvated H^+ and F^- , but also complex ions such as HF_2^- and H_2F_3^- , which may also contribute to the reaction mechanism.

The first chemical change that occurs in the etching of Si in a fluoride solution is the replacement of a chemisorbed H atom with a chemisorbed F atom. Immediately after oxide removal, the Si surface will have an F termination. It was initially suggested that the near-perfect chemical stability of a HF-treated Si surface was due to the F passivation, an argument that was supported by the fact that the Si–F bond strength is far greater than that of the Si–H bond. Trucks et al. [67] have argued that this is not the case. The Si–F bond is not only very strong, but it is also very ionic. The ionic nature of this bond polarizes the Si back bond. This polarization allows the insertion of HF into the Si–Si bond, leading to fluorination of the surface Si and hydrogenation of the second-layer Si. This sequence is shown in Fig. 4.

At the beginning of the etching process, the Si wafer is H-terminated. As Si has a band gap of greater than 0.5 eV, electrochemical dissolution requires the presence of holes at the surface and the initiation step of the MAC etching mechanism is the injection of valence band holes. The role of the valence band holes in controlling the anodic oxidation of Si was first recognized by Uhlir [68]. However, holes can be injected from an oxidant as occurs in electroless etching. For example, in Ag catalyzed MAC etching, millions of nanometer-sized metal nuclei, acting as local cathodes, oxidize

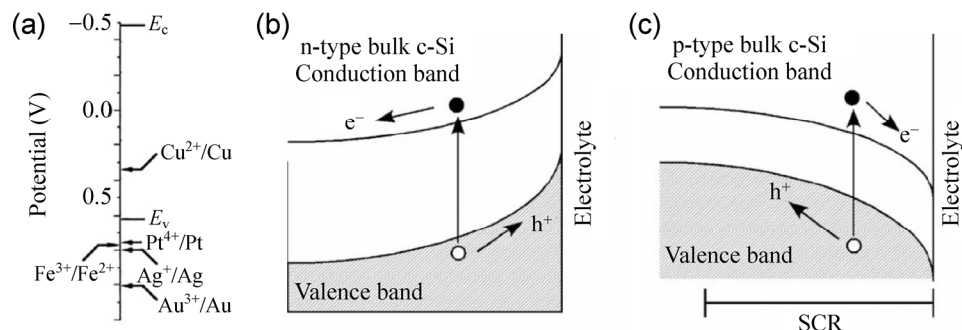


Figure 3 (a) Qualitative diagram of a comparison between the electrochemical electron energy levels of Si band edges (E_c and E_v are the conduction and valence band energies, respectively) and Ag^+/Ag , as well as four other redox systems in HF solution. Reproduced with permission from Ref. [66], © 2006 WILEY-VCH Verlag GmbH & Co. KGaA, Weinheim. (b) and (c) Band bending and the motion of electrons (e^-) and holes (h^+) under the influence of the SCR. The bands bend upward in (b) n-type Si and downward in (c) p-type Si. Reproduced with permission from Ref. [65], © 2009 Elsevier B.V.

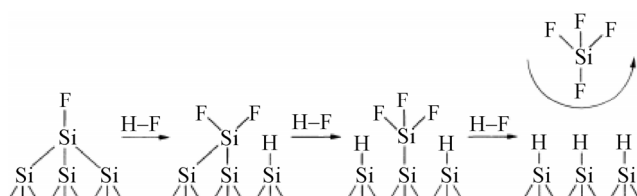


Figure 4 Schematic representation of the mechanism of H passivation. Reproduced with permission from Ref. [67], © 1990 American Physical Society.

the Si beneath, which is then dissolved by the HF etchants.

2.2 Typical HF/AgNO₃ cell

The HF/AgNO₃ cell was described in detail by Huang et al. [53]. A galvanic cell can be established by immersing Si into a HF/AgNO₃ solution because the electrochemical potential of Ag⁺/Ag is more positive than the Fermi energy of the Si (Fig. 3(a)). The Si surface is then oxidized by hole injection from the Ag⁺ particles, while the Ag⁺ particles themselves become reduced to Ag as a result of the injection of electrons from the valence band of Si. The Si oxide underneath the Ag particles is then removed by the HF and the Ag particles sink into this void, as was shown in Fig. 2.

2.3 Bottom-up vs. top-down NW fabrication

The fabrication of Si NWs can be divided into two main categories. The first of these approaches is defined as top-down and includes the various etching methods previously described in this review. The alternative approach is to form the NWs using bottom-up methods. The most common of these methods involves the use of a metal catalyst to initiate a VLS growth method [69, 70]. The Si NWs are formed by introducing a Si vapor source (typically silane) with the resultant NW diameters determined by the size of the liquid metallic NP catalyst.

The advantage of MAC-etched Si NWs over Si NWs formed by different methods, e.g., VLS, is that the MAC-etched Si NWs are the remaining etched features of the starting substrate and each Si NW is electrically connected to the current collector so that all the NWs can contribute to the electrochemical reactions, e.g., the specific capacity, if the NWs were being used as an anode for an LIB. Additionally, the NW crystal orientation and doping density mimic the

underlying substrate, while VLS NWs preferentially grow in the [111] and [112] directions can vary with NW dimension and synthetic growth conditions [71, 72]. Moreover, doping of VLS Si NWs uses harsh chemicals such as phosphine that are not ideal [73]. It has also been shown that the orientation of VLS Si NWs depends on the diameter of the Si NWs [74] and that VLS Si NWs tend to have cylindrical shape whereas MAC etching can produce structures with higher surface-to-volume ratios [75, 76], caused by surface roughness, hierarchical etching length scales (etched structures on etched structures, etc.), and a maximum degree of internal porosity. VLS Si NWs can also produce different morphologies within the same sample, leading to non-uniformity of said samples [77].

Electrochemical methods of producing Si NWs do not require lithography and are particularly interesting for producing larger volumes of Si NWs, owing to the advantages of large scale, low fabrication cost, and the relative simplicity of processing [7]. It has also been reported that NWs prepared via VLS and oxide-assisted growth methods are loosely attached and do not have a good electrical contact to the current collector [78]. The comparative performance of Si NWs for LIB applications formed using bottom-up and top-down approaches will be discussed in Section 4. Sample images of MAC-etched Si NWs are shown in Fig. 5. Figure 5(a) is a photograph of Si NWs fabricated on a 2-inch substrate showing the anti-reflective nature of the NWs [79]. Figure 5(b) is a high-resolution transmission electron microscopy (HRTEM) image of a MAC-etched Si NW with an electron diffraction pattern inset showing the single crystalline nature of the Si NW, which can now be grown with a high degree of uniformity in length and sidewall morphology over large-area wafers [59]. A cross-sectional scanning electron microscopy (SEM) image of MAC-etched Si NWs (Fig. 5(c)) shows the uniform length of the Si NWs and the characteristic clumping of the NWs at their tips [80]. Figures 5(d)–5(k) display plane views and cross-sectional SEM images of Si NWs etched from low-doped Si wafers and highly doped Si wafers, and it is becoming clear that in this MAC process, even without controlled illumination conditions, that doping type and concentration specifically influence the formation of porosity within the NWs—the analogy to

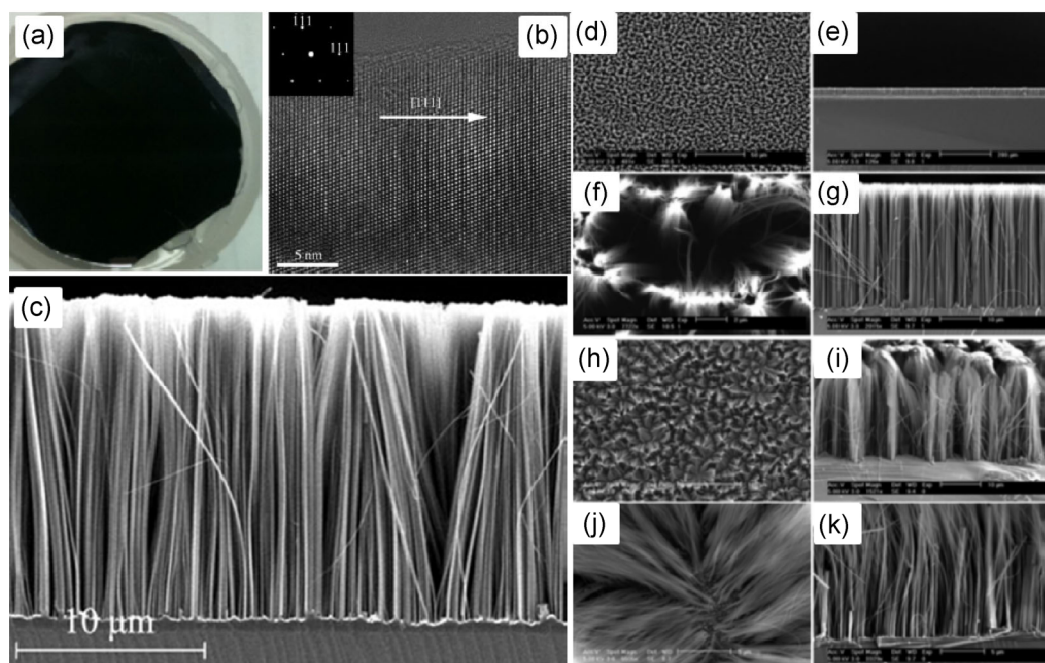


Figure 5 (a) Photograph of MAC-etched Si NWs on a Si wafer. Reproduced with permission from Ref. [79], © 2009 Royal Society of Chemistry. (b) HRTEM image of a Si NW and its electron diffraction pattern (inset). Reproduced with permission from Ref. [82], © 2006 WILEY-VCH Verlag GmbH & Co. KGaA, Weinheim. (c) Cross-sectional SEM image of Si NWs produced on p-type 7–14 Ω·cm Si (100) wafer. Reproduced with permission from Ref. [80], © 2008 WILEY-VCH Verlag GmbH & Co. KGaA, Weinheim. SEM images of Si NWs (d)–(g) from a lightly doped Si wafer and (h)–(k) from a heavily doped Si wafer. Reproduced with permission from Ref. [56], © 2008 American Chemical Society.

porous silicon is that the interpore regions are etched further, but in a controlled manner even in the case of MAC etching, without the further control of an applied potential bias [81].

2.4 Influence of doping density on the formation of MAC-etched Si NWs

Porous Si is a promising candidate for LIB anodes, because the pores within a Si structure can provide space for the Si to expand during Li insertion, which can help to prevent cracking of the Si structure and hence prevent a large loss in capacity.

Electrochemical etching can fine-tune the direction and size of pore growth, which defines the remaining skeletal material. MAC etching, however, can result in high sidewall roughness, and controlling this surface roughness and the transition to porosity [83] is a key challenge for reproducible large-scale formation of functional nanoscale Si.

The doping density of Si plays a major role in defining the type of etching [19, 84] and the resulting morphology for many of the parameters that affect the

electrochemistry and etching of Si [16, 17]. The final Si nanostructure generated can be controlled by the substrate doping type level [81, 85].

Porous Si via MAC etching is conventionally made from highly doped Si. It was found that, with the increasing doping level, the Si NWs resulting from the MAC etching process become rougher and eventually porous [42, 81]. A key requirement for electroless etching methods is the need to control porosity formation. These methods of pore formation usually give a simple structure with uniform pore size through the pore opening to the pore bottom, because the pore size formed by these methods is often regulated by the Ag or gold (Au) [86] used as a catalyst [87]. The morphologies of pores formed in Si are also affected by the different metal elements used in the etching process (and also by the size and shape of the metal particles) [88]. When Pt was used, the pores showed a tapered structure, while spherical Au particles led to the formation of straight pores and non-spherical Au led to pores with spiral sidewalls. It is suggested that the Au particle rotated as it etched into Si. The irregular

shape of the Au particle likely induced a spatial variation into the supply of positive holes to Si from the Au particle, leading to the different etching rate on the particle, thus providing a force to rotate the Au particle and cause the spiral etching [5].

More complex hierarchical structures can also be formed using MAC etching. By etching bulk Si powder, electrodes composed of porous Si NWs connected to large micron-sized cores can be formed. Nanoporous Si NWs of 5–8 μm in length and with a pore size of ~10 nm were formed in bulk Si particles [89].

Previous investigations demonstrated that the HF concentration influences the mechanism that results in porosification of the resultant Si NWs, for a given doping type and concentration [83, 90]. A hypothesis is that Ag particles disintegrate and redeposit randomly on Si NW walls and continue to etch into the Si NWs, causing porous Si NWs. This process is increased with higher temperatures and higher doping density because high carrier concentrations favor electron transfer [63, 81, 91, 92]. Qu et al. [93] have demonstrated the fabrication of porous Si NWs. They found that the concentration of H_2O_2 can determine whether the fabricated Si NWs will be porous or non-porous.

Similarly, when using the HF and H_2O_2 etching method, Chern et al. [91] showed that solid Si NWs

and porous Si NWs can be produced by simply tuning the HF: H_2O_2 ratio. Porosity of the Si NWs was found to be greater at the tip, which resulted in bending of the Si NWs [94, 95].

Si NWs formed via the MAC etching process from p-type Si with varying resistivities of 10, 0.01, and <0.005 $\Omega\cdot\text{cm}$ showed increased roughness with decreasing resistivity of the Si [85]. Figures 6(i)(a)–6(i)(d) show the increasing porosity of Si NWs with increasing doping density of the original wafer. Figure 6(ii) is a schematic of Si NW formation in Si with different doping densities, giving a visual representation of how porous Si NWs are formed from highly doped Si [92].

Chartier et al. [96] demonstrated that the composition of the etching solution is an important parameter in MAC etching. They showed that a large variety of Si morphologies can be produced by changing the HF: H_2O_2 ratio. The different structures formed included mesopores, cone-shaped macropores, and craters. During etching, Ag NPs at the roots of the Si NWs can be converted into Ag^+ ions by H_2O_2 [93]. At a low H_2O_2 concentration, the generated Ag^+ ions can be transformed back to Ag by extracting electrons from the Si by oxidation. A higher H_2O_2 concentration will lead to a higher number of Ag NPs being converted

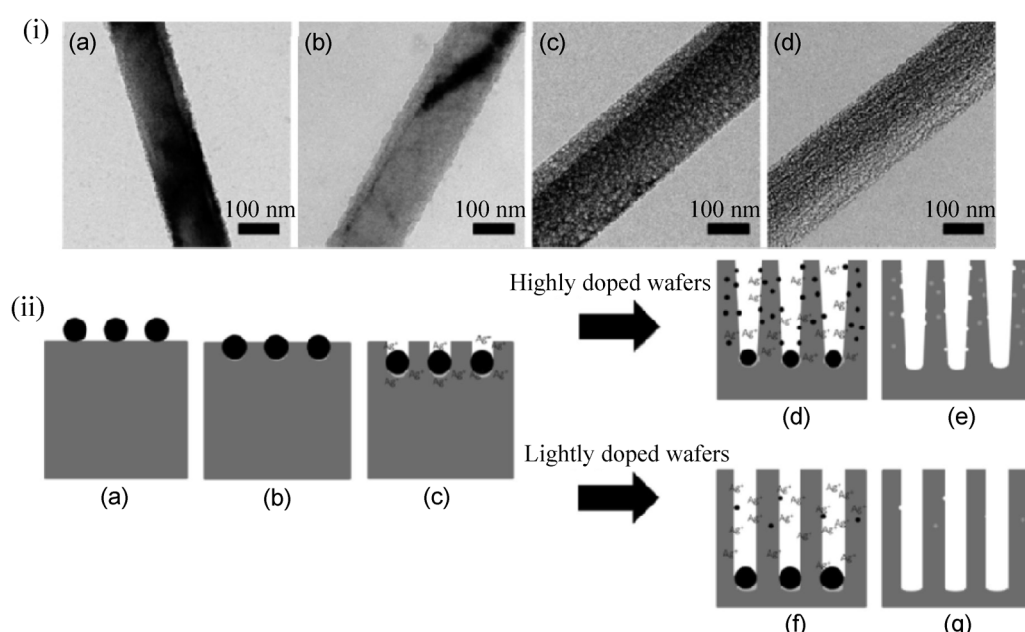


Figure 6 (i) TEM images of the Si NWs obtained from four types of wafers: (a) 1–5 $\Omega\cdot\text{cm}$ wafer, (b) 0.3–0.8 $\Omega\cdot\text{cm}$ wafer, (c) 0.008–0.016 $\Omega\cdot\text{cm}$ wafer, and (d) 0.001–0.002 $\Omega\cdot\text{cm}$ wafer. (ii) Schematic of the formation process for porous and nonporous Si NWs arrays through a MAC etching method for highly and lightly doped Si. Reproduced with permission from Ref. [92], © 2011 American Chemical Society.

into Ag^+ ions, increasing the number density of Ag^+ ions that can diffuse and nucleate on the sidewalls of the Si NWs to form new etching sites. Therefore, porous Si NWs can be achieved for lightly doped wafers at higher H_2O_2 concentrations [92, 97].

There have been few formal investigations of the influence of doping concentration and doping type on both roughness and porosity formation [98] within NWs.

2.5 Etching rates of Si NWs during MAC etching

It has been shown that the etching rate of Si using the HF/ AgNO_3 method increases with increasing AgNO_3 concentration, etching time [99], and temperature [100].

Zhang et al. [81] found that p-type Si etched more slowly than n-type Si of the same resistivity for both (100)- and (111)-orientated Si, while Lu and Barron [101] predicted that the etching rate increases with a higher concentration of HF in the etching process. They also demonstrated that a decrease in the [Ag] used in the etching process not only causes shorter structures but also decreases the diameter of the structures. The etching rate also increases with increasing AgNO_3 concentration [102]. The ideal conditions under which to form highly doped ($< 0.0035 \Omega\cdot\text{cm}$) Si NWs using MAC etching were investigated. In an etching solution that contained HF and H_2O_2 , it was found that the etching rate increased with increasing H_2O_2 concentration until the concentration reached 0.8 M, at which point the etching rate leveled out. When the concentration of HF was varied, it was found that the fastest etching rate was achieved at 8 M, with a lower etching rate above and below this value. Etching was conducted at 10, 25, and 40 °C and it was stated that for lower temperature reactions the HF and H_2O_2 concentrations should be increased to achieve equivalent reaction activity from the etchants [103]. The etching rate was shown to increase for samples with lower surface area [104]. It was shown that the etching rate of Si increased with the increasing thickness of an Au mesh that was deposited on the patterned Si surface prior to MAC etching. The faster etching rate was attributed to the Au mesh reducing the Si/Au Schottky barrier height and allowing an injection of holes from the Au into the Si, facilitating

a higher etching rate [105]. The use of masks on Si prior to etching and their influence on the etching process will be discussed in more detail in the next section.

2.6 The application of masks in conjunction with MAC etching

It may be useful for different devices and applications that rely on the structuring of Si, such as sensors, electrodes, and micro/nanoelectronics, to form Si NWs on specific areas of a Si wafer. MAC etching used in conjunction with various film patterning techniques has been demonstrated as a promising method for Si NW fabrication [80]. The orientation-controlled growth of Si NW arrays [106, 107] and the controlled growth of Si NWs in predetermined configurations [108] have been illustrated. Ultrathin anodic aluminum oxide (AAO) membranes have been utilized as versatile masks for fabricating 2D extended arrays of various functional nanostructures (microelectronics, optoelectronics, and sensing) [109] because of their unique ability to control the pore size and pore density. This method is cheap and repeatable, and AAOs with a range of pore diameters and interpore distances can be fabricated. MAC etching in combination with an AAO mask exhibits better control of the diameter, spacing, and density of Si NWs than etching without the AAO mask [105]. However, a trade-off exists with the utilization of an AAO mask possibly reducing the areal density of the Si NWs on a given surface area. Bottom-up growth of [100] Si NWs on Si (100) has been demonstrated by utilizing AAO as a template [89, 110].

The MAC etching process on a pristine Si wafer was compared to that on a Si wafer with a photoresist masking material, which confined the areas that could possibly be etched. It was found that the etching rate in the patterned Si was faster than that of the non-patterned Si. This was due to hexamethyldisilazane (HMDS), which is used in the deposition of the photoresist. The HMDS removed –OH groups from the Si surface and formed a hydrophobic surface that improved the etch rate [111].

Chang et al. [112] fabricated Si NWs using a combined approach consisting of MAC etching and block-copolymer lithography. They used critical point

drying (CPD) to significantly reduce the clustering at the top of the Si NWs. CPD is accomplished by heating a liquid in a closed system to reach the critical pressure at the critical temperature. The clumping in high-aspect-ratio etched NW bundles is dominated by capillary forces between NWs from the aqueous electrolyte solution. This force is described by $F = [\pi\gamma/(2L)](d_0\cos\theta)^2$, where γ is the surface tension, $2L$ is the center-to-center distance between neighboring NWs, d_0 is the diameter of the NW, and θ is the meniscus contact angle. Any variation in the spatial density of the wires and their separation or diameter will unbalance this force and lead to clumping and the development of island or crack-separated bundles on the substrate. During CPD, the liquid and gas states of the substance are no longer distinguishable at this initial point. The liquid within the specimen can therefore pass from the liquid to the gas phase with zero surface tension, greatly reducing the clumping of the formed NWs. Chang et al. [112] believed that Si NWs fabricated using this process would have applications in the creation of arrays of photonic and sensing devices. However, in spite of some success reported in the literature, crack formation is a measure of the randomness in NW dispersion caused by undefined Ag particle spatial control. This issue is directly addressed using masking approaches. Additionally, if the NWs are etched so that they exhibit internal porosity, their reduced rigidity implies a maximum aspect ratio that will allow CPD without clumping.

MAC etching was combined with pre-patterning of Si substrates to fabricate Si NWs on (100) Si wafers [113]. The diameter of the Si NWs was observed to decrease with increasing thickness of the metal film used in the etching. This was due to a closure effect of the pores in the metal film, which caused progressive shrinkage of the pore size in the metal film with increasing metal thickness. Si NW arrays with average diameters as small as ~8 nm and with a density of NWs as high as 10^{10} cm $^{-2}$ can be fabricated using this approach.

It has been shown that the combination of the growth of Si/Ge superlattices by molecular beam epitaxy (MBE), surface pre-patterning by AAO templates, and MAC etching can be successfully applied to fabricate Si NWs containing a Si/Ge superlattice.

Using this method, Si/Ge NWs with a diameter below 20 nm were obtained. The diameter could also be controlled via the pore diameter of the AAO template [94].

Figure 7(a) shows an SEM image of Si NWs after selective etching in conjunction with an AAO template. The dense array of Si NWs formed is capped by Au particles on their tops, which are orientated vertically, perpendicular to the surface of the Si (100) substrate. The average diameter of the NWs is ~60 nm, corresponding to the pore size in the AAO template [110].

An example of an AAO-based procedure is schematically illustrated in Fig. 7(b). First, an ultrathin AAO membrane/polystyrene composite was placed on a Si substrate (Fig. 7(b)(i)). Reactive ion etching (RIE) was performed to pattern the surface of the Si (100) substrate under SF₆/O₂, followed by removal of the ultrathin AAO mask (Fig. 7(b)(ii)). A thin layer of Ag or Au was deposited onto the patterned Si (100) substrate (Fig. 7(b)(iii)). Finally, arrays of vertically aligned Si NWs on the Si (100) substrate were obtained by performing MAC etching (Fig. 7(b)(iv)) [113].

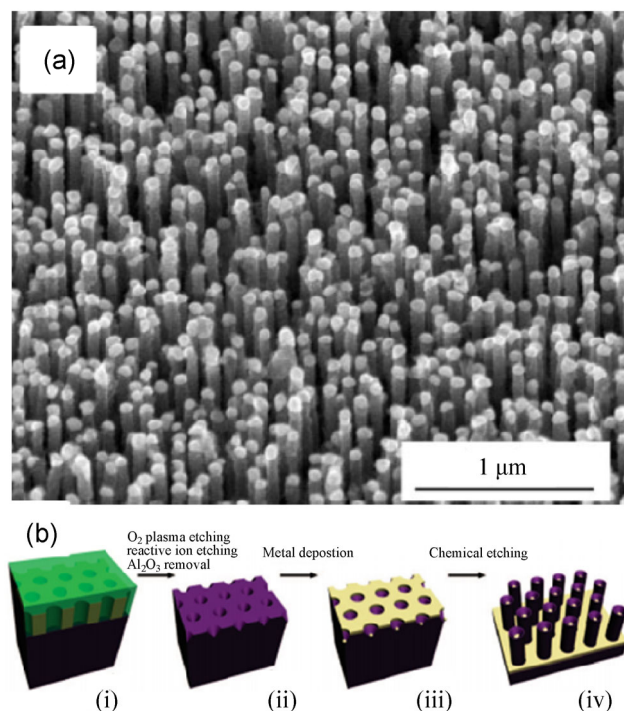


Figure 7 (a) Side-view SEM image with 60° tilt of Si NWs after selective etching of the AAO template. Reproduced with permission from Ref. [110], © 2007 WILEY-VCH Verlag GmbH & Co. KGaA, Weinheim. (b) Schematic of the MAC etching process in conjunction with the use of a photoresist mask. Reproduced with permission from Ref. [113], © 2008 American Chemical Society.

Another method was developed to fabricate high-density and well-aligned Si NWs through MAC etching using metal nanodots as a hard mask [114]. By fine-tuning the pore size of the AAO template used in the metal nanodot fabrication, the diameter of the Si NWs could be precisely controlled down to a precision of 10 nm.

Huang et al. [115] studied the MAC etching behavior of Si (110) substrates in conjunction with a metal film deposited using an AAO mask and found that the two preferred <100> etching directions can be suppressed by the presence of a metal film. Vertical or angled Si NWs relative to the substrate surface can be formed depending on the morphology of the film. Using this process, [110] Si NWs were formed with the diameter of the Si NWs being controlled by the pore diameter in the AAO template.

MAC etching of a Si (100) substrate using a gold mesh as a catalyst was used to fabricate Si NWs with varying orientations and morphologies, including zigzag Si NWs [111], Si NWs, and curved Si NWs [116]. It was found that the crystal orientation and morphology of Si NWs are controlled by the injection of holes (h^+) into the valence band and removal of oxidized Si by HF.

2.7 Orientation control of Si NWs using MAC etching

The direction of Si NWs relative to the substrate surface is important for Si-NW-based solar cells [117] and Si-NW-based field effect transistors [90, 91]. Initially, it was shown that etching in (100) and (111) Si occurred in the vertical direction only [59, 118]. However, more recently, contradictory reports have shown the formation of slanted NWs from substrates with these orientations [59, 80, 118–120]. Furthermore, non-(100) substrates have shown preferential etching in the (100) direction [59, 80, 118–120]. It was found that for (100) wafers with resistivities of 6–8 $\Omega\cdot\text{cm}$, vertical (100) Si NWs were formed at a volumetric ratio of 3:1 HF:H₂O₂, while (111) Si NWs were generated when the HF concentration was increased [91].

Chen et al. [121] prepared zigzag Si NWs with different turning angles via a MAC etching approach. This was made possible by controlling the spatial concentration of Ag NPs during etching. The shapes

of the zigzag Si NWs could be controlled via the orientation of the Si wafer, etching temperature, and etchant concentration. The orientation of the Si NWs produced could also be tuned by simply scratching the surface of the Si wafer; it was shown that the scratched area of the Si produced zigzag Si NWs, while the unscratched surface produced straight Si NWs. A selection of these Si NWs is shown in Figs. 8(a)–8(f). Variation of the etching direction in (111) n-type Si has also been illustrated through changes in the HF:AgNO₃ ratio and the etching temperature and time. The etching directions of the Ag particles were shown to be (111), (110), (211), (311), and zigzag depending on the etching conditions as shown in Figs. 8(g)–8(l) [122].

Oxidation-rate-dependent etching was observed in (111) and (110) Si substrates. In high oxidant concentration solutions, the etching occurs along the surface normal, but in low oxidant solutions the etching occurs in the <100> directions. Etching direction was also shown to change with a change in current density [104].

Figures 8(m)–8(p) show SEM images of Si NWs fabricated from (100) and (111) Si wafers. As shown in Fig. 8(m), Si NWs generated on Si (100) substrate were perpendicular to the etched surface. However, Si NWs formed from the Si (110) substrate were at an angle to the Si substrate, as shown in Fig. 8(n) and Fig. 8(o). The white arrows in Fig. 8(o) show the preferential [100] orientation of the Si NWs. This preferred etching direction is also shown in Fig. 8(p) [120].

Tsujino and Matsumura [123] showed that Ag particles etch in the (100) direction through Si (100) in a solution containing 5.3 M HF and 0.18 M H₂O₂, resulting in vertical pores. When etched for longer, it was shown that there were also horizontal pores emanating in the [0 1 0], [0 -1 0], [0 0 1], and [0 0 -1] directions, which are all crystallographically equivalent to the [100] direction. When the H₂O₂ concentration was reduced to 0.0018 M, the pores showed no preferred etching direction indicating that the etching direction may be related to the H₂O₂ concentration.

Vertically aligned zigzag Si NWs have been produced by etching a p-type Si (100) substrate twice [116]. The first etch was undertaken on a Si (100) wafer with an Au mesh in a solution of HF:H₂O₂ at a ratio of ~0.23,

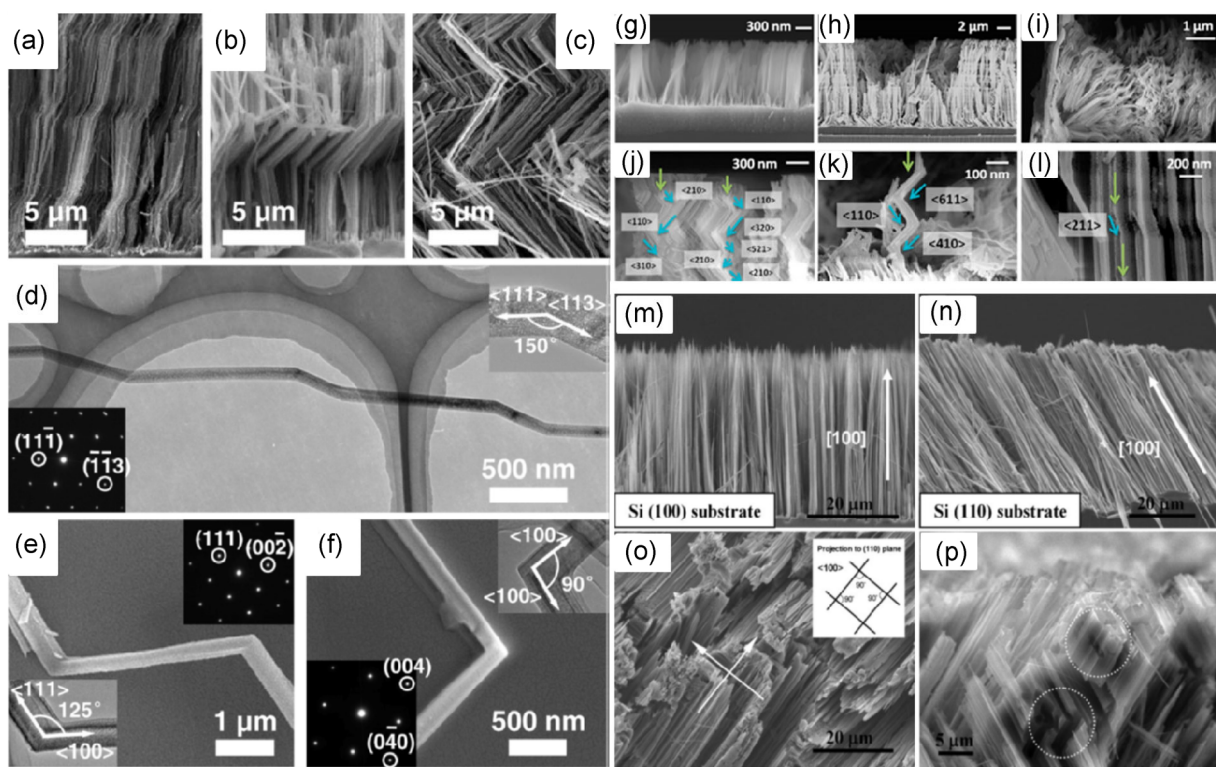


Figure 8 (a), (b), and (c) SEM images of three kinds of zigzag Si NW arrays on a Si wafer. (d) TEM and (e) and (f) SEM images of single zigzag NWs. Insets are TEM images and electron diffraction patterns of the turning points of the zigzag NWs, showing their growth directions alternating between (d) $\langle 111 \rangle$ and $\langle 113 \rangle$, (e) $\langle 111 \rangle$ and $\langle 100 \rangle$, and (f) two different $\langle 100 \rangle$ directions. Reproduced with permission from Ref. [121], © 2010 American Chemical Society. (g)–(l) Si NWs formed from n-type Si (111), (g) without and (h)–(l) with solution stirring. Reproduced with permission from Ref. [122], © 2013 American Chemical Society. (m) and (n) Cross-sectional SEM images of Si NWs formed on (m) a Si (100) substrate and (n) a Si (110) substrate. (o) Top-view SEM image of Si NWs on a Si (110) substrate. Inset is the projection of the Si NWs on the (110) plane. The orthogonal directions indicate the Si NWs oriented in the $[100]$ directions. (p) SEM image showing the branching pores on a Si (110) substrate. Reproduced with permission from Ref. [120], © 2008 WILEY-VCH Verlag GmbH & Co. KGaA, Weinheim.

and the second etch took place in a solution of HF:H₂O₂ at a ratio of ~23. While the HF:H₂O₂ ratio affected the morphology (porous NWs were formed at a lower HF:H₂O₂ ratio while nonporous NWs were formed at a higher ratio) of the Si NWs, the authors stated that it had no bearing on the etching direction. The etching temperature did, however, have an influence on etching direction, as would be expected from the high-rate generation and consumption of carriers or fast kinetics.

It was found that the etching direction of a given Si crystal orientation could be changed by varying etching conditions [63]. The MAC etching direction of Si (100) can be changed from $\langle 100 \rangle$ at room temperature to $\langle 110 \rangle$ at a higher temperature, depending on the H₂O₂ concentration. When the H₂O₂ concentration is ≤ 0.485 M, the etching always proceeds along the

$\langle 100 \rangle$ direction, but when the H₂O₂ concentration is increased to ≥ 0.727 M, the etching direction changes to $\langle 110 \rangle$ at a higher temperature.

The etching direction on Si (110) has also been shown to be related to the structure of the metal film deposited on the surface. A 5-nm-thick Ag film that was characterized as isolated patches with irregular shapes yielded slanted Si NWs, whereas a 10-nm-thick Ag film with randomly distributed pores yielded Si NWs perpendicular to the substrate [115]. Si (100) was etched using a solution of HF and H₂O₂, and while the vast majority of the etching took place perpendicular to the substrate surface, some etching parallel to the substrate surface was observed [124]. The hypothesis presented was that non-spherical Ag particles changed etching course in the crystallographically identical $\langle 100 \rangle$ direction.

To investigate the role of dopant type and substrate orientation in determining the orientation of Si NWs produced by MAC etching, Zhang et al. [81] etched p- and n-type Si (100) and p- and n-type Si (111) wafers. Independent of the doping type, it was found that both of the (100) wafers yielded NWs perpendicular to the substrate. The p-type Si (111) wafer yielded uniform Si NWs that were at an angle of 40° to the substrate surface in the <100> direction. The n-type Si (111) wafer resulted in NWs perpendicular to the substrate and a TEM investigation showed a (111) orientation for the NWs. It was also shown that in Si (111), Au particles etched at approximately 55° to the surface in the (100) direction [112].

Table 1 summarizes how the etching direction in Si can be changed by varying the etching temperature, HF:H₂O₂ ratio, and the HF:AgNO₃ ratio.

This section discussed MAC etching of Si NWs and the processes that enable etching. The advantages of MAC etching Si NWs in comparison with those formed via other methods, typically VLS, were discussed. Fundamentally, the doping level dictates the energetics of the semiconductor–solution interface and ultimately the rate of Li-ion insertion into the anode. The doping profile determines the depletion layer width, the relative redox potential–Fermi level shift, the Helmholtz and other double layer capacitances that influence ionic diffusion rates to the surface, the flat-band potential, and the electron density at the surface required to reduce Li⁺, among many other characteristics. Many of these characteristics are ill defined

in nanostructured silicon that is synthesized from precursors or through other bottom-up methods, an issue that is compounded by the lack of control of the spatial density of active dopants within nanostructures. Secondly, MAC etching and other electrochemical etching protocols for silicon, and by extension to Ge, may allow for phenomena such as depletion layer capacitance control of charge transfer that are not possible when nanoscale silicon is deposited on metallic current collectors. These phenomena, among others that influence reversible alloying with lithium, will be outlined in the next section.

The importance of porous Si NWs and how these porous Si NWs can be formed were investigated. This is typically done through the etching of highly doped Si but porous Si can also be formed from low-doped Si under the appropriate etching conditions. The application of AAO masks, block-co-polymer patterning, and other methods in conjunction with MAC etching to form Si NWs demonstrated some advantages of MAC etching for selective etching and site-specific NW growth. The various etching directions in the various orientations of Si wafers were discussed; typically, the etching direction is dependent on the wafer orientation but again this can be overcome by varying the etching parameters.

3 Si anodes for Li-ion batteries

Rechargeable LIBs are prevailing as the power source of choice for portable electronics and hybrid electrical

Table 1 A summary of how the etching direction in Si wafers can change by varying HF ratios and etching temperatures

Reference	Wafer orientation	Initial etching direction	Initial/final temperature	Initial/final HF:H ₂ O ₂ ratio	Initial/final HF:AgNO ₃ ratio	Final etching direction
Chern et al. [91]	(100)	<100>	—	2:1 / 3.5:1	—	<111>
	(110)	<100>	—	2:1 / 3.5:1	—	<111>
	(111)	<100>	—	2:1 / 3.5:1	—	<111>
Chen et al. [121]	(111)	<111>	15 °C / 75 °C	—	—	Zigzag
Bai et al. [122]	(111)	<110>	—	—	2.5:1 / 50:1	<111>
	(111)	<211>	10 °C / 20 + ≥ 30 °C	—	—	<311> +<111>
	(111)	<111>	—	—	250:1 / 50:1	Zigzag
Huang et al. [104]	(111)	<111>	—	46:1 / 2300:1	—	<100>
	(110)	<100>	—	11.5:1 / 4.6:1	—	<110>

vehicles [3, 125–128]. For mobile applications, high energy (per weight and volume) is the most important parameter, since it determines the usage time per charge [129]. Compared to other technologies, LIBs have high energy densities, good cycle life, and good power performance [1, 3, 125, 126, 130, 131]. LIB performance involves inter-related electrochemistry, phase transitions, and transport processes at the interfaces between electrodes and electrolytes [132].

To improve the performance of LIBs, an improved understanding of the behavior of active materials is sought. Bulk Li-alloy-type anodes comprising elemental Sn, Al, Ge, Si, or their alloys have demonstrated their functionality as LIB anodes with large specific and volumetric capacities [133]. Li would be the most favorable anode material for LIBs in terms of specific energy and electrode potential, but safety problems and loss of capacity upon cycling have prevented this [3, 134].

Si is an attractive anode material for LIBs because it has a relatively low potential range at which charging occurs, below 0.5 V [135], when reacting with Li. Si is known to incorporate a theoretical maximum of 4.4 Li atoms per Si atom [135], resulting in the highest known theoretical charge capacity ($\sim 4,200 \text{ mAh}\cdot\text{g}^{-1}$) [136], which is more than ten times higher than the capacity of conventionally used graphite ($\sim 372 \text{ mAh}\cdot\text{g}^{-1}$) and much higher than alternative oxide materials [54, 80, 119, 122, 137–140]. The discharge curve of Si during the electrochemical extraction of Li is relatively flat, very similar to that of graphite, allowing a constant energy and power delivery. In addition to its high capacity, Si is the second most abundant element in the earth's crust, is environmentally friendly, and is the focus of many worldwide corporations, which also makes it attractive when considering its use as an anode in LIBs. Rolled-up batteries based on Si NWs have even been demonstrated from silicon used in chips [141]. $\text{Li}_{15}\text{Si}_4$ is the highest lithiated phase achievable for the ambient temperature lithiation of bulk Si and corresponds to a capacity of $3,579 \text{ mAh}\cdot\text{g}^{-1}$ [142]. When bulk Si is fully lithiated to $\text{Li}_{15}\text{Si}_4$, it undergoes a volume expansion of 280% and has a maximum theoretical volumetric capacity of $2,190 \text{ mAh}\cdot\text{cm}^{-3}$. Unfortunately, Si electrodes pulverize as a result of the large expansion and contraction upon Li insertion and extraction and this causes the

electrode material to lose contact with the current collector, lower its conductivity, and result in a loss of capacity with cycling [71, 95, 133, 143–148]. Several Si structures have been investigated as viable anodes for LIBs, including Si thin films [149, 150] and Si powder [151, 152].

Recent work involving *in situ* TEM measurements of the crystalline to amorphous transition in silicon/Li-Si nanoparticles during reversible charge–discharge cycling suggested a critical size of $\sim 150 \text{ nm}$ for crystalline silicon [153] and a size of 870 nm for amorphous silicon [154], beyond which particles develop cracking and structural degradation to the point where the material breaks up. When considering realistic anode compositions, comprising densely packed nanoparticles and structures, the critical sizes for lithiation/delithiation-induced break-up might be different and are postulated to be smaller owing to nearest neighbor interactions [155]. However, electrolyte access to all particles is an assumption that is not strictly proven, and the influence of the crystal facet (known to strongly influence the insertion rate of Li ions into silicon for example), was not considered. For these influences, one must also consider the relative changes in electrical conductivity of the networked nanomaterial in silicon anodes designed to overcome adverse effects of volumetric changes on structures that are not perfectly spherical.

Recent theoretical investigations into the lithiation/delithiation mechanism in silicon, in parallel with experimental investigations into multistep amorphization of these Li-Si alloy phases, have suggested that porous structured silicon with nanoscale pores or other constructs with defined voids provide additional free space for volume expansion induced by lithium-ion insertion [156–159]. While this concept is somewhat obvious, the type, degree, and form of the porosity can influence the response to volumetric changes in some cases, which is influenced by the orientation of the crystal facets and by the nanoscale structure [157]. Some authors have demonstrated, through analytical modeling, that the effect of stresses and strains caused by insertion and extraction (dealloying in the case of silicon) reactions is dynamic, i.e., that the material, once lithiated, is no longer a simple crystalline silicon as modeled from the outset. Stresses and strains in Li-Si phases that undergo various amorphization

processes during insertion and removal of lithium compounds cause changes in the structure and also the original porosity designed to alleviate the expansion/contraction issue. Furthermore, significantly more effort is needed to consolidate all these effects with the variation in the rate of insertion and extraction at different facets, mediated by various doping levels, and the change in electronic band structure of Li–Si versus Si phases and their degree of crystallinity.

3.1 Si thin film behavior as a Li-ion battery anode

Thin films of Si may be more robust than bulk Si over repeated cycles of Li insertion and extraction, owing to their thin, uniform nature. As a result, many studies have examined their use as LIB anodes. More importantly, when developing a deeper understanding of the reversible lithiation behavior of nanoscale silicon and related materials with better physical properties (those from etching top-down rather than grown bottom-up) including metal–metalloid composites (Si–Sn, etc.), the response known for bulk-scale single crystals, thin films, and amorphous and compositionally graded silicon in LIBs is important to place an overview in context. Ohara et al. [160] vacuum-deposited Si films onto Ni foil. The Si film was expected to stick tightly to the Ni film even after volume expansion and contraction due to Li insertion and removal. The Si thin film retained its initial cyclic voltammetry (CV) curve for 500 cycles and the capacity of ~1,000 mAh·g⁻¹ after 1,000 cycles represented impressive cycling by the anode. They found that a

high rate of deposition of the Si onto the Ni foil was a factor in the rapid deterioration of capacity with cycling, while deposition that was considered to be too slow caused the Si to be inert to rapid Li insertion.

Amorphous Si thin films of 250 nm and 1 μm in thickness were sputter-deposited on Cu foil [145]. The reversible capacity of the 250 nm film was found to be ~3,800 mAh·g⁻¹ with a fade of 0.09% per cycle when cycled at a current density of ~C/2.5 while the reversible capacity of the 1-μm film was ~3,000 mAh·g⁻¹ with a capacity fade of 0.2% per cycle when cycled at the same current density. This shows that thinner Si films exhibit enhanced cycling ability in comparison to thicker Si films.

Unfortunately, this capacity retention was only maintained for ~20 cycles for the 1-μm-thick film and ~30 cycles for the 250-nm-thick film, as can be seen in Fig. 9(a). A possible reason for the decrease in capacity is the pulverization of the Si thin film, with cracking reducing electrical contacts to both the current collectors and the active material in plane. When the active material is pulverized as a result of expansion and contraction taking place in its crystal structure, the material can lose electrical contact with the current collector and hence reduce the capacity of the electrode by rendering some of the active material electrically (and thus electrochemically) inactive for charge storage. The cracking of the Si anode can be seen in Figs. 9(b) and 9(c) [145]. This is typical for a non-nanostructured alloy-type material reacting with Li. The cracking of the Si anode can be visually compared to the cracking of most brittle porous materials.

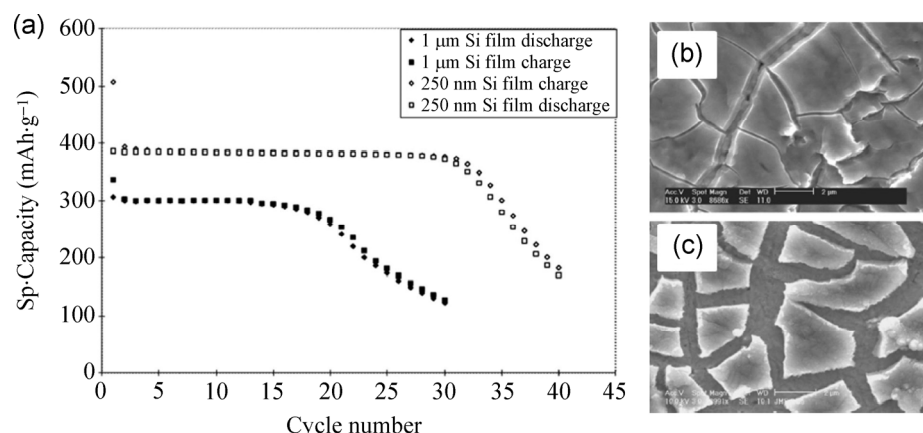


Figure 9 (a) Comparison of galvanostatic cycling of 250-nm- and 1-μm-thick Si films on Cu foils (both at a ~C/2.5 current density). (b) and (c) Plane-view SEM images of 250-nm-thick Si film cycled at ~C/2.5 for (b) 1 cycle and (c) 30 cycles. Reproduced with permission from Ref. [145], © 2006 ECS-The Electrochemical Society.

This effect was also shown in other Si thin films [146] and also in tin (Sn) alloys [133].

Si thin films have also been prepared by chemical vapor deposition (CVD). It was shown that an amorphous Si thin film could be cycled with a maximum discharge capacity of $\sim 4,000 \text{ mAh}\cdot\text{g}^{-1}$, but that the capacity faded rapidly after 20 cycles. However, by increasing the lower potential limit from 0 to 0.2 V and therefore limiting Li insertion, the capacity of the electrode was reduced to $400 \text{ mAh}\cdot\text{g}^{-1}$ but the electrode retained this capacity for ~ 400 cycles [149].

Using a similar method, Si was vacuum deposited onto Ni foils by Uehara et al. [161], Takamura et al. [162], and Ohara et al. [150]. It was found that thinner Si films retained capacity better than thicker Si films, that roughening the Ni foil improved capacity and that capacity of the Si films decreased with an increasing C-rate. Si films have also been deposited on different substrates, including graphene foam (via CVD), with the resulting anode achieving a reversible capacity of $1.4 \text{ mAh}\cdot\text{cm}^{-2}$. The authors claimed that the graphene foam provided a conductive pathway for charge transport and facilitated the expansion of the Si upon charging [163].

Zhao et al. [164] also electrodeposited a Si film on a Ni foam. The film showed an initial capacity of $\sim 4,830 \text{ mAh}\cdot\text{g}^{-1}$, which quickly decreased and plateaued at $2,800 \text{ mAh}\cdot\text{g}^{-1}$ for 80 cycles with a Coulombic efficiency (CE) of $> 95\%$ after the first cycle. For comparison, pristine Si NPs were also tested. The Si film exhibits much better performance than Si NPs, whose capacity fades quickly. From electrochemical impedance measurements, the diffusion coefficients of Li^+ in pristine Si NPs were found to be much slower than those of the Si film after the first cycle. This helps explain the improved performance of the Si film versus that of the NPs.

3.2 Si combined with other elements to form an anode

Composite Si electrodes were investigated and were shown to improve capacity retention compared to pure Si anodes. The additional elements often act as a buffer (preventing Si expansion) or as a conductive additive (increasing the conductivity of the anode). This section examines how these elements were incorporated.

A layered microporous Cu/Si/Cu electrode was fabricated and coated with polyethylene (PE) to stabilize the electrode during Li insertion. A schematic of this electrode is shown in Fig. 10(a) [165]. This electrode retained a capacity of $> 1,000 \text{ mAh}\cdot\text{g}^{-1}$ for over 120 cycles while retaining its pore structure. With the top and bottom Si surfaces blocked by Cu, Li insertion into Si primarily occurred at the Si sidewalls. It is believed that this led to a more uniform lithiation of the Cu/Si/Cu electrodes and hence resulted in the anode retaining its structure. A porous Si/Cu film was also investigated, and the porous nature of the anode allowed it to expand and contract without pulverization; the lack of pulverization aids in the capacity retention of the anode and it exhibited a capacity of $1,628 \text{ mAh}\cdot\text{g}^{-1}$ after 100 cycles. This report demonstrates the importance of potentially limiting Li insertion into Si anodes.

Hatchard et al. [166] produced SiAlSn films by combinatorial sputtering. They attained capacities of

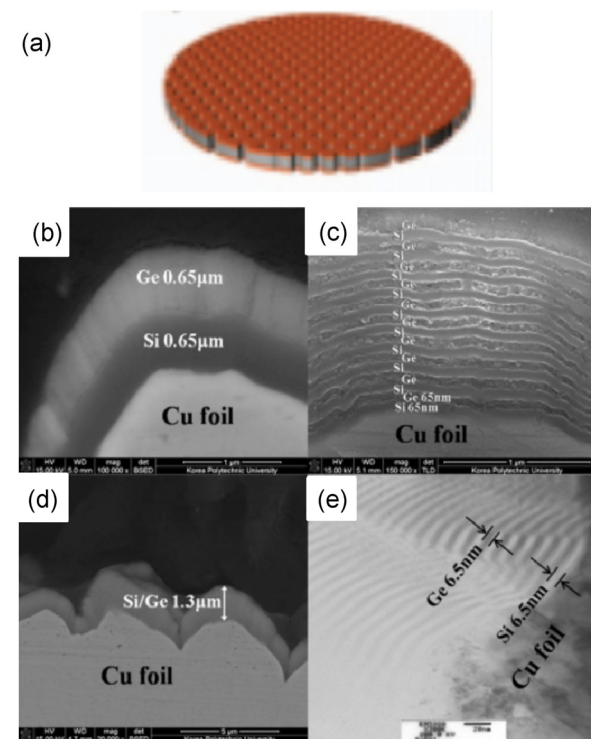


Figure 10 (a) The schematic depicting the encapsulated microporous device, Cu/Si/Cu. Reproduced with permission from Ref. [165], © 2013 The Electrochemical Society. (b)–(d) SEM cross-sectional images. Si and Ge were alternately deposited (b) once, (c) ten times, and (d) hundred times on a Cu current collector. (e) TEM image of the 100-layer electrode. Reproduced with permission from Ref. [167], © 2010 Elsevier B.V.

up to $1,800 \text{ mAh}\cdot\text{g}^{-1}$, as well as reversible capacities of over $1,500 \text{ mAh}\cdot\text{g}^{-1}$ when cycled between 1.2 and 0.1 V vs. Li for 10 cycles. They showed that capacity retention was best in amorphous areas of the film, while the capacity faded quickly when there was crystalline material present owing to the inhomogeneous nature of the expansion and contraction of the crystalline material.

Si has also been used in combination with other alloying materials in dually active composites. Si and Ge layers were deposited in sequence on a Cu current collector, with the number of layers being varied with the resulting structures electrochemically tested as anodes. A single Si/Ge layered electrode was fabricated with each layer being $0.65 \mu\text{m}$ thick, while more complex layered Si/Ge electrodes (10 layers with each layer being 65 nm thick and 100 layers with each layer being 6.5 nm thick) were also fabricated, as shown in Figs. 10(b)–10(e). Figures 10(b)–10(d) are SEM images of these three electrodes showing the alternating layers. Figure 10(e) is a TEM image of the 100-layer electrode showing the thicknesses of the alternating Si and Ge layers. After 100 cycles, the 10-layer Si/Ge electrode had a capacity of $\sim 1,000 \text{ mAh}\cdot\text{g}^{-1}$, while the 100-layer and mono-layer Si/Ge electrodes both had capacities of $\sim 500 \text{ mAh}\cdot\text{g}^{-1}$. It was proposed that the Ge acted as a buffer to volume changes during Li insertion and extraction. However it was noted that the performance for the 100-layer electrode decreased, since the film could not endure the plastic deformation due to that electrode having the highest expansion/contraction rate of the three electrodes [167].

While the anodes do not achieve their theoretical maximum capacity, the limiting of Li insertion would lead to a better cycling performance of the Si anodes. The additional elements also help to prevent the full expansion of the Si, hence reducing the degradation of the anode. The additional elements also improve the conductivity of the Si anodes.

3.3 Si powder anodes

Si electrodes with Si powders were prepared and had partial success in alleviating the volume change associated with Li insertion and extraction [168–170]. Si powders were also fabricated as composites to improve the conductivity and hence to improve

capacity retention with cycling [171–177].

Electroless deposition of Cu has been used to enhance the electrical conductivity of Si powder [178]. The Si was etched before the Cu deposition. The resulting Cu-deposited Si powder electrodes exhibited improved cycleability compared to bare Si anodes. For different samples, which had different electrical conductivities, the first discharge capacity was larger and the capacity retention improved with an increase in the conductivity of Si powders.

Kim et al. [179] investigated the formation of C-coated Si/graphite powders as anode materials. A TEM image of C-coated Si powder is shown in Fig. 11(a). This anode showed a high reversible capacity of over $600 \text{ mAh}\cdot\text{g}^{-1}$ for 15 cycles. They compared a C-coated Si/graphite anode and a pristine Si/graphite anode and, although an initial discharge capacity of $750 \text{ mAh}\cdot\text{g}^{-1}$ could be obtained for the two anodes, the C-coated Si/graphite composite anode showed better cycling performance compared with the pristine

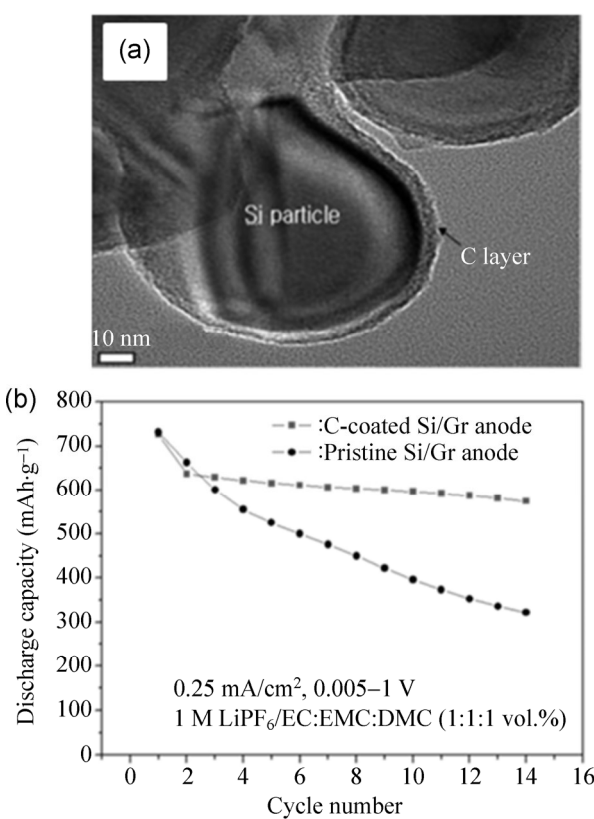


Figure 11 (a) TEM image of C-coated Si powder and (b) the cycle performance of a C-coated Si/graphite electrode vs. an uncoated Si/graphite electrode. Reproduced with permission from Ref. [179], © 2008 Korean Chemical Society.

Si/graphite anode, as shown in Fig. 11(b). It was also shown that reducing the Si particle size improved the capacity retention of the Si anode.

In a similar approach, a 3D C-coated porous Si (PS) powder was fabricated. The CV response of the C-coated Si exhibited higher currents than that of the raw Si, indicating a much larger surface area for electrochemical reaction. The raw nonporous Si had an initial capacity of $> 3,000 \text{ mAh}\cdot\text{g}^{-1}$ but this fell quickly to $\sim 250 \text{ mAh}\cdot\text{g}^{-1}$ after 10 cycles. The C-coated Si also exhibited an initial capacity of $> 3,000 \text{ mAh}\cdot\text{g}^{-1}$, however the capacity after 10 cycles was $\sim 1,500 \text{ mAh}\cdot\text{g}^{-1}$ and after 100 cycles the capacity was shown to be $\sim 665 \text{ mAh}\cdot\text{g}^{-1}$. The improvement in capacity retention was ascribed to a shorter Li^+ diffusion length in the porous powder and a greater surface area when compared to the raw Si.

The failure modes of Si powder as an anode were investigated by Ryu et al. [152]. It was found that capacity fading occurs primarily in the delithiation stage. The electrodes displayed a marked increase in resistance during the delithiation process, owing to loss of contact between the Si and C in the anode, which prevented complete delithiation. Si anodes then degraded with Li ions still remaining within the anode structure because delithiation was not completed for each cycle.

Si powders were investigated as anodes for LIBs and it was shown that the addition of other elements (Cu), the incorporation of conductive additives (C), and the formation of porous Si powder all improved the capacity retention of the Si anodes. These results show the importance of additives in Si anodes.

3.4 The influence of doping and conductivity on the performance of Si anodes

There is limited information in the literature concerning the influence of Si crystal orientation, carrier concentration, and dopant type on Li insertion and extraction processes. An important characteristic of Si is its doping density, which is directly related via its carrier mobility to its conductivity. The conductivity of Si anodes is typically varied by introducing a conductive additive (often carbon) [181–184], which is often required for intrinsically doped Si or materials and structures with low conductivities [185].

The few studies that do exist on the lithiation of doped Si in nanostructured form are on dispersed powder mixtures, often involving amorphous Si [186] or polycrystalline nanoscale Si-graphite mixtures [187] and related nanoscale Si analogues. The doping contribution to conductivity and Li uptake (the reduction of Li upon insertion at the cost of an electron) is difficult to separate from the enhanced electrical conductivity of the entire material matrix, which becomes continually hole-doped while changing its structure, composition, and electrical nature. This is further complicated by changes in active material contacts within the matrix, the random, uneven distribution of conductive additives in powder materials, and the inconsistency in rational doping of some forms of Si.

Doping type and density modify the Li insertion and extraction processes, and in nanoscale systems all of the abovementioned parameters, including doping control, can vary from nanostructure to nanostructure [188]. Etching of bulk wafers is one method to improve doping control, orientation, and electrical contact. Peng et al. [78] and Xu et al. [189, 190] reported Si NW anodes fabricated by MAC etching of Si wafers. This method has the potential for precise control of the doping of the NWs [78, 191, 192]. Density functional theory and related modeling have confirmed the influence of crystal orientation on Li insertion in a variety of materials [193], leading to prediction of cell potentials, favored facets for higher rates of insertion, and links between the Li uptake and the crystallographic phase change. Amorphization, morphology changes, and secondary electrolyte interphases can occur during reversible lithiation. A first principles study suggests that dopants can have an effect on the binding energy of Li with Si [194]. A systematic examination of doping on many aspects of Li insertion and removal in Si is still required.

Long et al. [195] showed the effects of boron (B) and phosphorus (P) dopants on the lithiation of crystalline Si. By using Raman scattering spectroscopy, they were able to identify differences in Li insertion potentials for the different dopant types. The B dopant moves the lithiation potential higher relative to the undoped Si, whereas the P dopant lowers the insertion potential, as shown in Figs. 12(a) and 12(b). The different Fermi

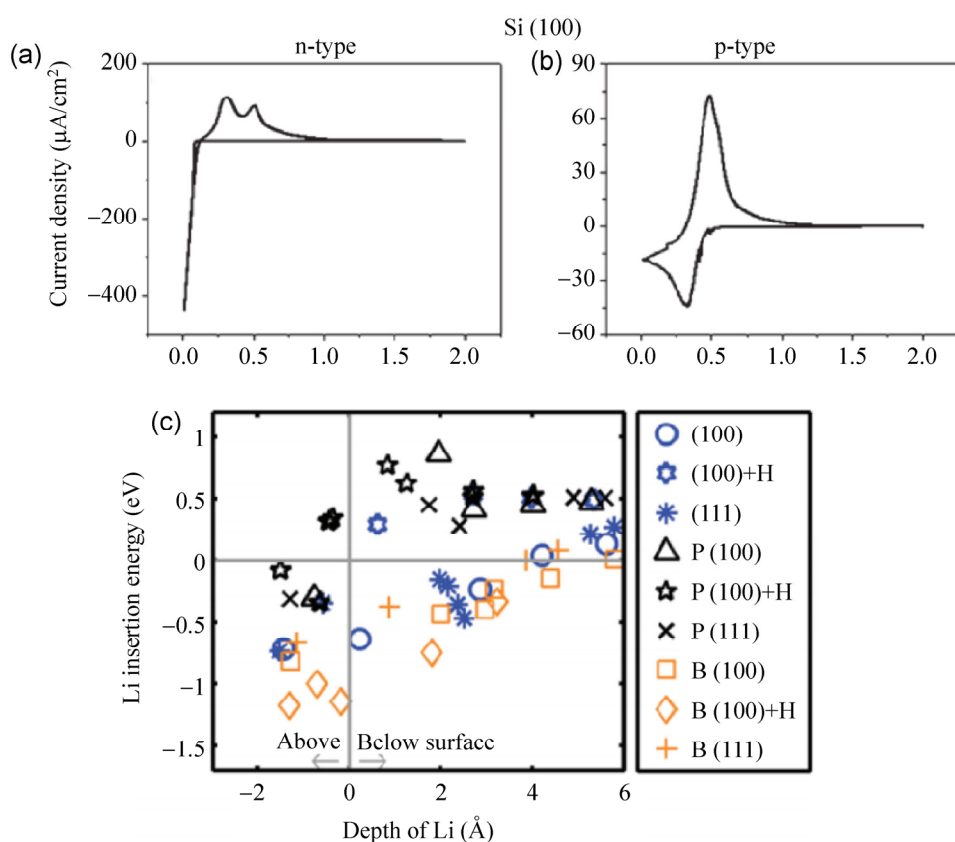


Figure 12 (a) and (b) CVs of (a) n-type and (b) p-type Si (100). (c) Single Li insertion energy relative to bulk Li for B- and P-doped Si (100) and (111) surfaces. For the (100) surface, results with hydrogen passivation on the top surface are also shown. Reproduced with permission from Ref. [195], © 2011 American Chemical Society.

levels in heavily B- and P-doped surfaces affect the Li insertion energies by respectively lowering and raising the energies of states available to the electron accompanying the Li^+ . This explains the higher initial Li insertion potential for the p-type Si when compared to n-type Si. The Li insertion energy as a function of Li depth is shown in Fig. 12(c) for both doped and undoped Si, with different orientations and with H passivation. Surface lithiation on both p-type and n-type Si surfaces is energetically favorable, whereas Li insertion below the surface (depth > 0) is favorable only on p-type Si surfaces. For subsurface lithiation of n-type Si surfaces, dilute Li insertion into the subsurface is not possible, but higher Li-content silicides may be formed. In contrast, initial Li insertion into the subsurface layers of p-type Si surfaces occurs at 0.5–1 V. Figure 12(c) provides an explanation for the observation that Li insertion into a p-type Si surface occurs at a higher voltage than into the corresponding n-type Si surface.

B-doped Si particles were prepared by high-energy ball-milling of B and Si powders in varying ratios [196]. The two electrodes were prepared with the following nominal B concentrations (atoms per mole of Si): 0 and 10^{21} , (equivalent to 0 and 0.167 at.% B, respectively). The B21 anode was shown to be less resistive than the B0 anode but, contrary to other reports, it was shown here that the doping has little to no influence on the electrochemical performances of the two anodes. It was stated that the high relative resistance of Si does not play a key role in the poor electrochemical performance of Si-based electrodes.

In a study examining the impact of n-type doping on electrochemical performance, intrinsic Si thin films and n-type conductive Si thin films deposited on Ni current collectors were compared electrochemically [150]. It was shown that not only the specific capacity but also the cycle performance of the conductive Si were much improved when compared with those of the intrinsic Si film. The initial charge/discharge



efficiency was improved from 65% to 88%. It was concluded that the electrical conductivity of the deposited film plays an important role in providing a favorable performance for the Li insertion/extraction reaction.

Separate investigations on the influence of doping levels and doping type (where the majority of charge carriers are holes rather than electrons for Li reduction), have shown that different conduction types of silicon (n- or p-type) can influence the degree to which Li is intercalated and the associated mechanism of amorphization. Raman scattering mapping and X-ray photo-electron spectroscopy of n- and p-type silicon after lithiation conclusively showed that highly doped n-type Si (100) surface regions retain Li as a silicide and convert to an amorphous phase during early cycles via a polycrystalline phase as a two-step phase conversion process [197].

While doping of Si influences the resistivity and the Li insertion potentials of the Si anodes, some confusion remains as to whether or not the doping of Si has a role to play in the improvement of the capacity and capacity retention of Si anodes.

3.5 Composites of silicon

Pure Si anodes exhibit poor cycleability owing to the stresses in the Si caused by large volume changes upon Li insertion and removal. One method to overcome this is to place the active Si material within a “buffering” inactive material. The inactive material would not contribute to the capacity of the anode but it would, however, prevent the Si anode from expanding fully and hence improve the cycleability of the anode. These types of Si anodes are often called composite anodes as they often contain two or more different elements.

A composite electrode architecture, a (Ba–Fe–Si/C composite) was synthesized by mechanical ball milling [180]. It was shown that the Ba–Fe–Si/C composite not only possessed a reversible capacity of $420 \text{ mAh}\cdot\text{g}^{-1}$, but also exhibited very stable capacity retention with very little capacity decay after 25 cycles. The Ba–Fe–Si/C composite also retained capacity better than a pure Si anode and a Ba–Fe–Si alloy despite having a lower initial capacity, as shown in Fig. 13(a).

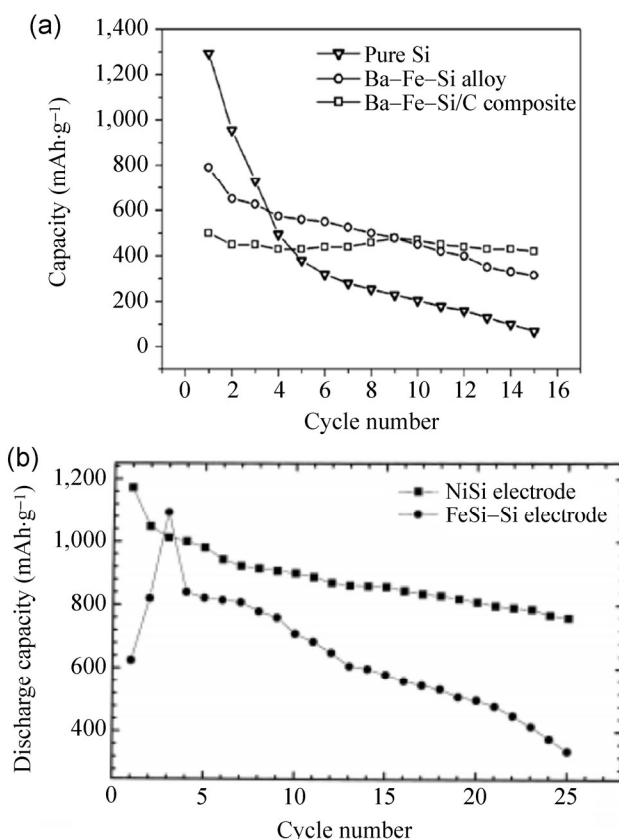


Figure 13 (a) A comparison of the cycling performances of pure Si, Ba–Fe–Si alloy, and the Ba–Fe–Si/C composite electrode at a constant current of $100 \text{ mA}\cdot\text{g}^{-1}$. Reproduced with permission from Ref. [180], © 2003 Elsevier B.V. (b) Discharge capacities of NiSi and FeSi–Si. Reproduced with permission from Ref. [198], © 2000 Elsevier Science S.A.

Another synthetic approach involved the preparation of NiSi and FeSi alloy powders by high-energy ball-milling [198]. Both electrodes achieved a capacity of $>1,000 \text{ mAh}\cdot\text{g}^{-1}$; however, the rate of capacity decrease for the FeSi electrode was found to be faster than that of the NiSi electrode, as shown in Fig. 13(b). The capacity of the NiSi electrode fell to $\sim 800 \text{ mAh}\cdot\text{g}^{-1}$ whereas the capacity of the FeSi electrode fell to $<400 \text{ mAh}\cdot\text{g}^{-1}$, which was possibly due to the presence of large unalloyed particles of Si that formed in the FeSi electrode but not in the NiSi electrode.

Alternative composites, such as one consisting of Si/Ni alloy/graphite, were probed as an anode material [147]. In addition to NiSi₂ and NiSi phases, the graphite also accommodated the large volume changes of Si during cycling. The reversible capacity of $780 \text{ mAh}\cdot\text{g}^{-1}$ and good cycleability showed that Si/Ni alloy and graphite composite (6:4 by weight ratio) retained

capacity better than the 7:3 ratio, the 5:5 ratio, and the Si–C (5:5) composite ratio. The cycleability of Si/Ni alloy and graphite composites is greatly improved in comparison to Si–C composite.

A Si composite material was fabricated by mixing Si powder with carbon black (CB) at different weight ratios through manual grinding in air [169]. The Si composite was compared electrochemically with a pristine Si powder. The capacity at the first cycle for the two anodes was similar ($\sim 2,700 \text{ mAh}\cdot\text{g}^{-1}$). With cycling, the capacity of the composite was retained better than that of the pristine Si powder. When the discharge of the composite anode was limited to 0.8 V, the capacity retention of the anode also increased as a result of a limitation on the delithiation and therefore on the volume change of the Si particles. Zuo et al. [199] investigated Si/C anodes with sodium carboxymethyl cellulose/styrene butadiene rubber (CMC/SBR) and poly(vinylidene fluoride) (PVDF) as binders. They showed that the electrode with CMC/SBR binder had a lower capacity decrease after 40 cycles. They attributed the better retention of capacity to the better maintenance of the anodes' integrity by the CMC/SBR binder. The role played by binders in determining cell performance will be discussed in greater detail in Section 4.1.

Figure 14 shows the superior capacity retention of Si nanostructures compared to bulk Si and it also shows the cycling of graphite over 50 cycles. There is

an immediate and extreme loss of capacity for the bulk Si anode, resulting in its capacity falling below $0.3 \text{ Ah}\cdot\text{g}^{-1}$ after only 5 cycles whereas the Si nanofilm and nanocrystals have capacities of $\sim 1.7 \text{ Ah}\cdot\text{g}^{-1}$ and $0.5 \text{ Ah}\cdot\text{g}^{-1}$ after 50 cycles respectively. Si NWs have also been shown to have a much better cycling performance than Si nanocrystals [200].

Section 3 overviewed the use of bulk Si anodes for LIBs. The use of Si thin films was investigated and it was found that thinner Si films retain capacity better than thicker Si films. However, a limitation with thin films is that the film thickness is usually a few hundred nanometers, which leads to a limited specific charge capacity of $\sim 0.1 \text{ mAh}\cdot\text{cm}^{-2}$ and is insufficient for viable applications [201]. Amorphous Si was found to exhibit superior cycling capability compared to crystalline Si. The addition of other elements was found to improve the capacity retention of Si anodes, either by acting as a buffer to alleviate stresses during expansion or to improve the conductivity of the anode. The doping profile of Si anodes was also shown to be one method to influence the Li insertion potential into Si anodes but there are contradictory reports of whether or not the doping of Si anodes improves their performance as a LIB anode.

Si nanostructures are now well known to cycle much better than bulk Si, but the comparison is often too limited in the literature. Affecting the ambipolar conductivity for ions and electrons is a primary motivator for choosing lower dimensional silicon, but this affects the conductivity, doping profile, and the surface reactivity. Comparing bulk to nanoscale silicon should ideally involve the many aspects of the silicon–electrolyte interface that go beyond simple size reduction effects, and form a basis set for examining the many benefits, and limitations, that nanoscale LIB materials made from semiconductors possess. The knowledge, even at bulk scale, of the influence of Si–metal composites on the capacity, structural changes, Li insertion and alloying metallurgy, and charge rate variation, among other characteristics, is important when making direct comparison to, and predictions of, nanoscale silicon composite materials as LIB anodes. The next section will deal with a variety of shapes, sizes, crystal structures, and composite Si nanostructures as anodes in LIBs.

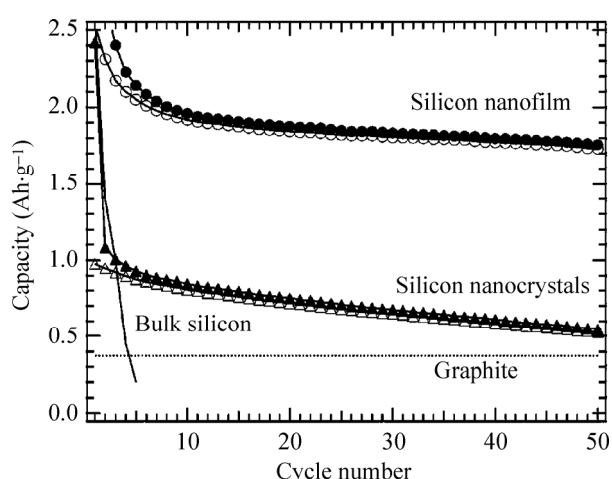


Figure 14 The capacity of Si nanocrystals and a Si nanofilm over 50 cycles. The theoretical specific capacity of graphite and the measured capacities for bulk Si are also included. Reproduced with permission from Ref. [200], © 2003 ECS-The Electrochemical Society.

4 Nanostructured Si anodes for Li-ion batteries

This section focuses on a wide range of Si nanostructures, such as Si NWs, Si nanopowders, and core–shell nanostructures for use as anode materials for LIBs. In addition, the influence of doping and conductive additives on their performance will be discussed. Various Si nanostructures have been investigated as viable anode materials for LIBs, including Si nanopillars [202], Si NWs [203–205], Si nanowall structures formed via lithography [206], core–shell Si NWs [207, 208], Si inverse opal structures, Si spheres [209], Si nanotubes [210], Si NPs [184], pomegranate-inspired Si nanostructures [211], and Si NWs decorated with Si NPs [212]. Considerable progress has been made regarding nanostructured Si as an active (insertion) and passive (scaffold) anode material [72, 213, 214] and the viability of the approach looks promising [215]. Laboratory-scale results obtained thus far indicate that nanostructured Si might meet the majority of battery requirements; the ubiquitous supply of high-quality bulk and nanoscale silicon and the need for greener, recyclable batteries will promote

its development. Recent investigations have focused on the quality and development of ordered nanoscale wire and pore arrays in Si for use in LIBs [196, 216].

The advantage of Si nanostructures over bulk Si material is that low-dimensional nanostructures can accommodate the > 400% volume change upon Li^+ insertion and extraction in Si without pulverization (Fig. 15(a)). They also provide good electronic contact and conduction and display short Li^+ insertion distances. The nanostructures also have a higher surface area accessible to the electrolyte, which allows more of the electrolyte to react with the electrode, hence increasing capacity, but sometimes at the expense of a greater fraction of charge associated with stable solid electrolyte interface (SEI) formation on a greater surface area. Figure 15(b) shows the improved capacity of Si NWs over Si nanocrystals and graphite over 10 cycles and Figs. 15(c)–15(f) display Si NWs during the first Li insertion, through TEM and electron diffraction, showing the transition from crystalline Si to amorphous Si.

This Si NW nanostructured anode showed great promise as an anode for an LIB as it attained the theoretical capacity of Li in Si ($\sim 4,200 \text{ mAh}\cdot\text{g}^{-1}$) and exhibited a 75% capacity retention over the first 10

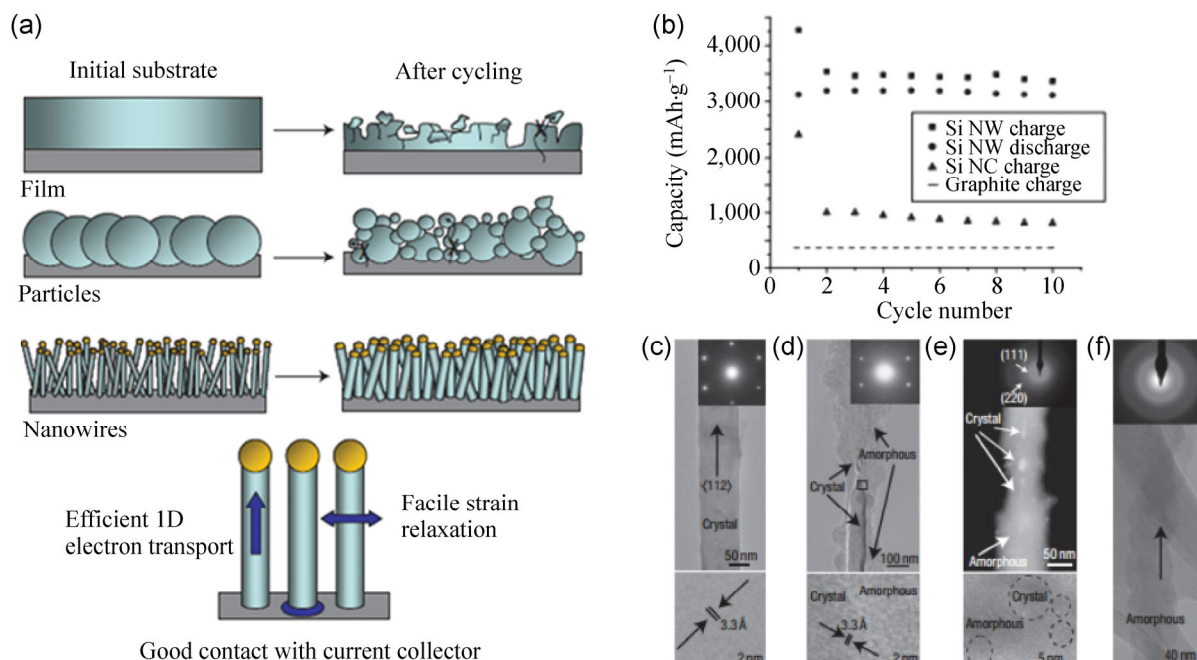


Figure 15 (a) Schematic of the cycling behavior of bulk Si, Si particles, and Si NWs. (b) Capacity versus cycle number for Si NWs at the C/20 rate. The charge data for Si nanocrystals (triangles) and the theoretical capacity for lithiated graphite (dashed line) are shown as a comparison to show the improvement in capacity when using Si NWs. (c)–(f) The transition of a crystalline Si NW to an amorphous Si NW via TEM and electron diffraction when the NW was charged to 10 mV. Reproduced with permission from Ref. [71], © 2008 Nature Publishing Group.

cycles. This was the first example of Si NWs being utilized in an LIB anode and likely stimulated research into the use of Si nanostructures as LIB anodes.

4.1 Si nanopowder anode materials

One problem with Si NW electrodes grown via CVD is the relatively low mass loading. A Si-NP-decorated Si NW network was fabricated [212] to investigate ways of increasing active mass loading of silicon. The Si NPs were electrically connected to Si NWs to increase the mass loading of the Si NW electrode and a thin layer of Si deposited by a CVD method overcoats the entire network to ensure excellent electrical conduction between Si NPs and Si NWs, along with the stainless steel substrates, as shown in Fig. 16(a). It was shown that this process increased the areal capacity of Si-NW-based electrodes, from ~ 0.6 to ~ 2.5 $\text{mAh}\cdot\text{cm}^{-2}$. The anodes exhibited good cycling performance and maintained the decorated, porous network structures after charging-discharging cycles.

Binders are essential for composite anodes by providing adhesion between the anode materials and current collectors. Generally, the adhesion that the binder provides keeps the particles together in the particle-based anodes and makes them adhere to the current collector. Some methods involve precursor synthesis of silicon containing phosphazenes that allow nanostructured powder formation directly on conducting substrates, including conductive carbon additive formation through polymer decomposition [217, 218]. This is particularly important in Si anodes, which expand and contract by $> 400\%$ upon insertion and extraction of Li^+ ions.

Wagner et al. [219] proposed the use of binders that should be able to stabilize the electrode composite during cycling. They proposed that the key requirements of a binder are:

- good binding properties;
- no extensive swelling in polar organic electrolytes;
- electrochemical stability; and
- processability.

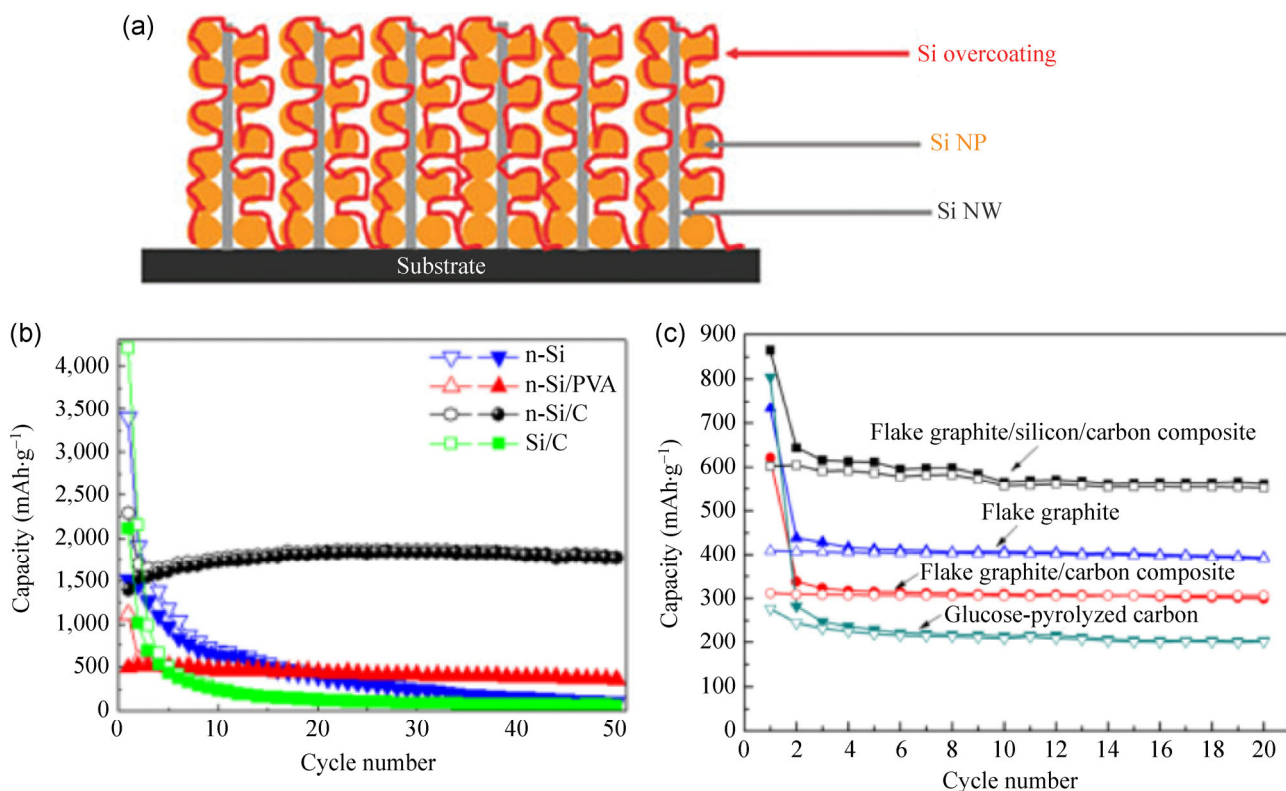


Figure 16 (a) Schematic of Si NPs adhered to Si NWs to increase mass loading of the anode. Reproduced with permission from Ref. [212], © 2010 Royal Society of Chemistry. (b) Comparison of the cycleability of nano-Si, nano-Si/PVA, and nano-Si/C electrodes at a constant current of $100 \text{ mA}\cdot\text{g}^{-1}$. Reproduced with permission from Ref. [222], © 2012 Elsevier Ltd. (c) Charge/discharge capacities of flake graphite, glucose-pyrolyzed C, flake graphite/C composite, and flake graphite/Si/C composite electrodes as function of cycle number. Reproduced with permission from Ref. [224], © 2012 Elsevier B.V.

Wu et al. [220] created an electrode by mixing nanosized Si and micrometer-sized Si and using poly(9,9-dioctylfluorene-co-fluorenone-co-methylbenzoic ester) (PFM) as a binder. The electrode retained a capacity of $\sim 2,500 \text{ mAh}\cdot\text{g}^{-1}$ after 30 cycles, which is a marked improvement on an electrode where they used acetylene black in place of the nanosized Si. They attributed the improved performance (both in terms of initial capacity and capacity retention) to the ability of the nanosized Si to prevent severe agglomeration of the micron-sized Si, which led to a significant reduction of the stress induced by the large volume change of the macro-Si during the Li insertion/extraction process. C-rate experiments were also carried out on the electrode with the C/25 rate exhibiting a capacity of $\sim 3,000 \text{ mAh}\cdot\text{g}^{-1}$ and the 2C rate exhibiting a capacity of $\sim 2,200 \text{ mAh}\cdot\text{g}^{-1}$. The key role played by binders in determining the performance of LIB anodes based on Si particles was shown by using a binder consisting of β -cyclodextrin (or β -CDp). When examined as a binder for Si anodes, the β -CDp was found to have a self-healing effect where even Si particles that lost contact with the anode could be recovered by the binder. These particles could then contribute to the capacity of the anode again [221].

A core-shell-structured nano-Si/C electrode was fabricated using a Si nano-powder core and an amorphous C shell [222]. This electrode was compared to the nano-Si/PVA electrode with PVA acting as a binder. The initial charge capacity was $2,300 \text{ mAh}\cdot\text{g}^{-1}$ for the core-shell anode compared to $1,200 \text{ mAh}\cdot\text{g}^{-1}$ for the PVA anode. Four electrodes were cycled for 50 cycles: Nano-Si, nano-Si with PVA, nano-Si with a C shell, and micron-sized Si with a C shell. After the 50 cycles, the nano-Si with the C shell electrode had a capacity of $\sim 1,500 \text{ mAh}\cdot\text{g}^{-1}$, whereas the other three electrodes had capacities of $< 500 \text{ mAh}\cdot\text{g}^{-1}$, as shown in Fig. 16(b). This shows the importance of the C shell and the size of the Si particles to the performance of the electrode. The behavior of core-shell structures will be dealt with in a later section.

Kuksenko and Konovalenko [223] stated that a reduction in the size of Si, with transition to the nano-scale, improves the structural strength of Si electrodes against cracking upon large changes in volume, due to lithiation and delithiation of Si anodes. Thus, they

fabricated hybrid electrodes using two different synthetic graphites (KS6 and MAG) and Si nanopowder and three different binders. The KS6/nano-Si/PVDF electrode exhibited an initial discharge capacity of $930 \text{ mAh}\cdot\text{g}^{-1}$, whereas the initial discharge capacity for the MAG/nano-Si/((sodium carboxymethyl-cellulose, butadiene-styrene) Na-CMC, BSC) electrode was $354 \text{ mAh}\cdot\text{g}^{-1}$. This study showed how the use of different carbons and binders can greatly influence the performance of the Si anodes. In a similar approach, a flake graphite/Si/C composite anode was prepared [224]. The initial capacity was shown to be $\sim 850 \text{ mAh}\cdot\text{g}^{-1}$, which decreased to $552 \text{ mAh}\cdot\text{g}^{-1}$ after the 20th cycle. The initial capacity was much lower than that of a raw nano-Si electrode ($\sim 3,250 \text{ mAh}\cdot\text{g}^{-1}$); however, the capacity of the raw Si electrode fell to $\sim 160 \text{ mAh}\cdot\text{g}^{-1}$ after 20 cycles showing the importance of the inclusion of graphite and C in the Si anode. A comparison of the electrochemical performance of various graphite/C/Si anodes is shown in Fig. 16(c).

4.2 Methods of fabricating Si NWs: Vapor-liquid-solid growth

The VLS growth mechanism [69, 70] is a well-known process for growing NWs that exploits the eutectic region in a binary phase diagram. One of the elements acts as a catalyst for nucleating the NWs while the other is supplied as a vapor and ultimately forms a solid NW. After the growth, each NW has the catalyst as its tip. For Si, a common catalyst is gold (Au); the Au catalyst is heated above the eutectic temperature (363°C) and SiH_4 is introduced and allowed to decompose into Si. The Si dissolves in the Au particle and forms a eutectic droplet. Upon reaching supersaturation, nucleation of a single-crystalline Si NW occurs. A continuous supply of Si vapor results in continued axial growth of the NW [225], as shown in the schematic in Fig. 17(a). This alloying process can be depicted as an isothermal line in a phase diagram (Fig. 17(b)). SEM (Figs. 17(c) and 17(d)) and TEM (Figs. 17(e) and 17(f)) images of VLS-grown Si NWs on a stainless steel substrate are shown in Figs. 17(c)–17(f). The VLS growth mechanism is a versatile synthetic approach that allows the formation of NWs directly on a variety of substrates and as a result is well suited to the formation of Si-NW-based LIB anodes.

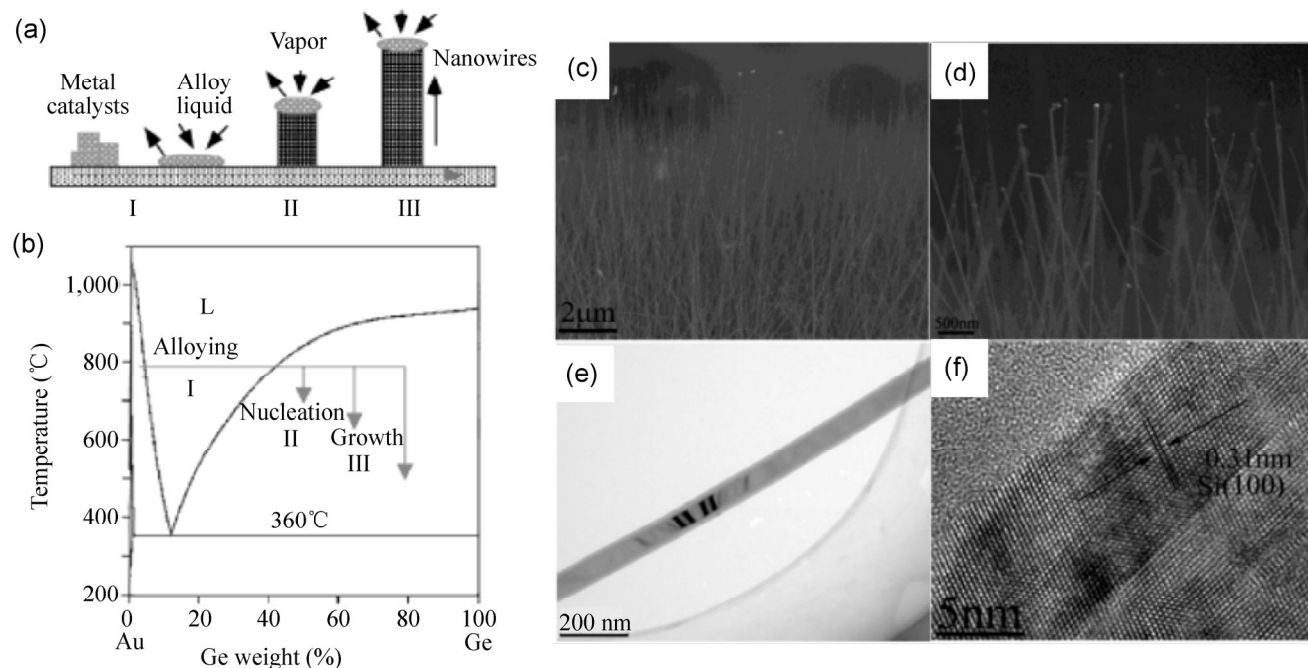


Figure 17 (a) Schematic illustration of the VLS NW growth mechanism showing the three stages of (I) alloying, (II) nucleation, and (III) axial growth. (b) The three stages are projected onto the conventional binary phase diagram to show the compositional and phase evolution during the NW growth process. Reproduced with permission from Ref. [227], © 2001 American Chemical Society. (c) and (d) SEM images, (e) TEM image, and (f) HRTEM image of grown Si NWs. Reproduced with permission from Ref. [228], © 2012 Elsevier B.V.

Si NWs grown on current collectors [71, 226] by VLS growth have shown some promise in circumventing the pulverization issues suffered by bulk and thin-film Si anodes, as they can expand and contract without pulverizing. They also inherently reduce the Li insertion distances.

Chan et al. [225] performed galvanostatic cycling on VLS-grown Si NWs and reported that the capacities quickly degraded with each cycle, suggesting that the process is not reversible over many cycles. They reported that the “trapping” or irreversible alloying of Li^+ with Au may be a possible cause for the capacity fading observed in the VLS-grown Si NWs.

In contrast with this report, a full electrochemical investigation was conducted on Au catalyzed Si NWs grown on stainless steel and the quick decline in capacity mentioned above did not occur [71]. The observed capacity during the first charge was $4,277 \text{ mAh}\cdot\text{g}^{-1}$. Both charge and discharge capacities remained nearly constant for subsequent cycles, with little fading up to 10 cycles. A C-rate analysis on the Si NWs at rates between C/20 and 1C was conducted. The C/20 rate obtained the largest capacity of

$\sim 3,600 \text{ mAh}\cdot\text{g}^{-1}$ while the 1C rate had a capacity of $\sim 2,100 \text{ mAh}\cdot\text{g}^{-1}$.

The use of AAO masks in conjunction with top-down MAC etching to form Si NWs was discussed in Section 2.7. The use of AAO masks and bottom-up approaches have also been examined for Si-NW-based anodes and were shown to influence the performance of these Si NW anodes. Cho and Picraux [229] reported the fabrication of Si NWs using a combination of the VLS technique and the application of an AAO mask. The AAO mask was employed to prevent the formation of Si islands on the anode. It was stated that stress can build in these Si islands, causing cracking of the Si NWs and hence a reduction in capacity of the anode. When the electrode was cycled at 0.5C, a capacity of $> 1,000 \text{ mAh}\cdot\text{g}^{-1}$ was achieved for over 1,100 cycles after an initial capacity of $> 3,000 \text{ mAh}\cdot\text{g}^{-1}$. The authors also showed a decrease in capacity with increasing C-rate, with a 1C rate having a capacity of $\sim 3,000 \text{ mAh}\cdot\text{g}^{-1}$ while a 10C rate had a capacity of $< 1,000 \text{ mAh}\cdot\text{g}^{-1}$. They attributed the impressive performance of the anode to the absence of the Si islands.

The synthesis of Si NWs was demonstrated via

hot-filament chemical vapor deposition (HFCVD) [228]. CV scans at $0.5 \text{ mV}\cdot\text{s}^{-1}$ showed an increase in current with cycling owing to an activation effect for each subsequent cycle. Constant current charging and discharging at 0.05C showed an initial capacity of $\sim 3,670 \text{ mAh}\cdot\text{g}^{-1}$, falling to $\sim 3,440 \text{ mAh}\cdot\text{g}^{-1}$ after 20 cycles. At a C-rate of 0.05C , the NWs had a capacity of $3,650 \text{ mAh}\cdot\text{g}^{-1}$, while at 1C they retained a capacity of $2,200 \text{ mAh}\cdot\text{g}^{-1}$. The thickness of the gold layer deposited played an important role in determining the morphology of the Si NWs. A thick layer resulted in ordered NWs while a thin layer resulted in disordered NWs. This study examined the influence of a pre-deposited metal on the formation of Si NWs.

An investigation into the influence of diameter distribution of Si NWs on the performance of LIBs was carried out by Gohier et al. [230]. They also grew NWs using the HFCVD method. They showed the first lithiation capacities were $5,698 \text{ mAh}\cdot\text{g}^{-1}$, $3,678 \text{ mAh}\cdot\text{g}^{-1}$, and $3,681 \text{ mAh}\cdot\text{g}^{-1}$ for Si NWs with diameters of 65 nm, 210 nm, and 490 nm, respectively, at a C/10 rate. However, they noted that the CE is lower for the smaller diameter NWs owing to the increased surface area. It was found that smaller diameter NWs exhibit the best capacity retention when varying the C-rate between C/5 and 5C. NWs with smaller diameters provide a shorter Li diffusion path and would seem the most promising for LIB applications.

While the VLS mechanism is straightforward and reasonably controlled, the Si NWs produced are generally intrinsically doped and therefore not very conductive. Controlled doping methodologies, which are difficult to implement for VLS wire growth on the scale required by commercial batteries, or the use of conductive additives, are required to improve conductivity and electrical addressing in the active materials [78] for the entirety of the active material, even under compression in an assembled cell. The inclusion of conductive additives and binders to Si NW anodes increases the weight and the cost of LIBs, also increasing production time and the number of production steps necessary to form the anodes. It would thus be beneficial to the cost of the anode to remove these steps and use an anode that is exclusively Si. VLS NWs also require the use of a catalyst (e.g., Au) that in some cases can react irreversibly with Li and

add significant inactive mass to the resultant devices. VLS NWs also have a non-uniform doping density [231], which makes it difficult to predict the resistance of the anode in electrochemical testing; it is essential to have uniform doping throughout every NW for electrochemical testing. Thus, the ideal Si anode for LIBs is a Si NW anode that does not require the use of binders or conductive additives, that has uniform doping density throughout the NWs, and does not contain a sufficient quantity of catalyst material with which Li ions can irreversibly react with.

More recently, solution-based growth methods have been examined as more cost-effective alternatives that allow the formation of Si NWs at higher yields than typically afforded by CVD processes [232–236]. These reports also highlight the negative impact of Au as a catalyst material for LIB applications and proposed the use of either Sn [233, 236] or In [237] as electrochemically active catalyst materials, which led to improved performance compared to Au-containing electrodes. Si NWs have also been grown in porous C via a supercritical fluid–liquid–solid (SFLS) method [238]. The percentages of Si NWs in the varying porous C electrodes were 54.5%, 71.4%, and 80%, respectively. The initial charge capacity was shown to be $3,398$, $2,863$, and $2,204 \text{ mAh}\cdot\text{g}^{-1}$ for the 80%, 71.4%, and 54.5% samples, respectively. However, the CE was highest for the highest percentage of C, indicating the importance of C to CE. After 100 cycles, the 80% Si NW electrode exhibited the highest capacity while the 54.5% Si NW electrode exhibited the lowest capacity.

Figure 18(i) shows the changing nature of Si NWs as various points in a CV cycle in a Li half-cell configuration. The NW can be seen to change through various crystalline and amorphous phases at different potentials owing to Li insertion and extraction. Figure 18(ii) shows the change (via STEM and electron diffraction) from an amorphous Si NW ($a\text{-Li}_x\text{Si}$) to a crystalline Si NW ($c\text{-Li}_{15}\text{Si}_4$) when x (the number of Li atoms per Si atom) reaches 3.75. Also shown in Fig. 18(ii) is the atomic arrangement of the amorphous and crystalline Li_xSi . Figure 18(iii) shows, via STEM images and elemental mapping, that (Figs. 18(iii)(a)–(d)) the lithiated $a\text{-Li}_x\text{Si}$ shell around the pristine Si core contains no crystalline phases. This remains true as x approaches 3.75 (Figs. 18(iii)(e)–(h)). With further

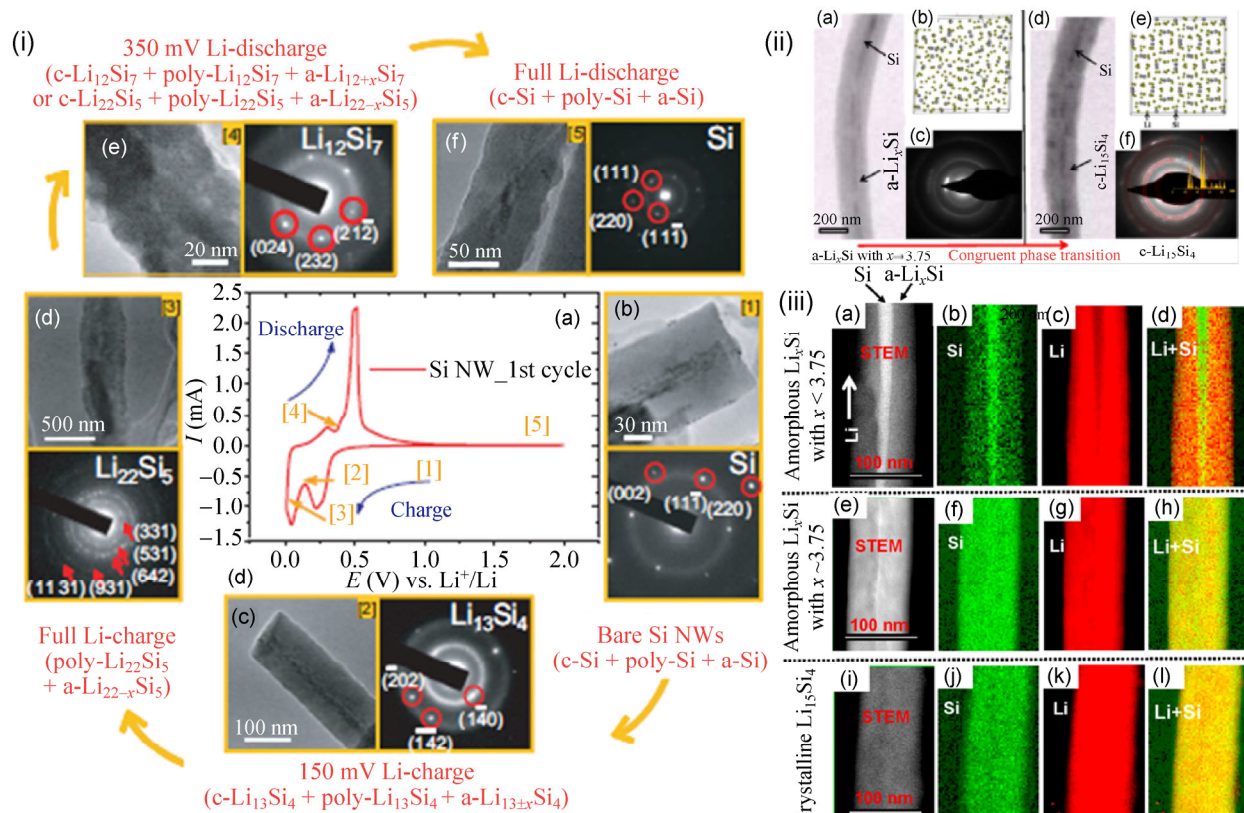


Figure 18 (i) A representative CV of the Si NW anodic cell. (i)(b)–(f) TEM images and the corresponding diffraction patterns from the NW samples extracted at given potentials, marked in (a). Reproduced with permission from Ref. [204], © 2010 American Institute of Physics. (ii) STEM bright-field images, electron diffraction patterns, and the sequence of atomic arrangements revealing the spontaneous crystallization of a-Li_xSi to c-Li₁₅Si₄ when x reaches the critical value of 3.75. (iii) STEM annular dark-field image and EELS elemental distribution maps showing the phase transition characteristics of the a-Li_{3.75}Si to c-Li₁₅Si₄: (a)–(d) for progression of lithiation from bottom to top, (e)–(h) as x approaches 3.75 in a-Li_xSi, and (i)–(l) following the crystallization of a-Li_xSi to c-Li₁₅Si₄. Reproduced with permission from Ref. [239], © 2013 American Chemical Society.

lithiation (Figs. 18(iii)(i)–(l)), the whole NW spontaneously transforms to crystalline Li₁₅Si₄ and shows no fluctuations in chemical composition.

In this section the use of VLS Si NWs as anodes for LIBs were discussed, and there were contradictory reports as to whether the Au tips negatively impact the performance of the Si anodes or not. The influence of the diameter of the Si NW was also shown to be crucial in the performance of the Si NW anode. The problem that arises with doping VLS Si NWs and the lack of control of the material's inherent electrical conductivity motivates options for mass-production of Si NWs and related structures through alternative routes. Recent investigations suggest that a beneficial contribution to performance, including improvement of the C-rate, from Si–Sn [240] and Ge–Sn metal–metalloid composites, which can often be easier to

grow in large quantities using bottom-up VLS and related synthesis methods, compared to the top-down MAC of silicon wafers, where in-diffusion of Li-alloying metals such as Sn is more difficult. Some bottom-up methods also have the benefit of being grown directly on current collectors.

4.3 Core–shell Si nanostructures

Recent investigations have involved the use of hollow structures and so-called “clamped” structures (the structures have a SiO_x coating layer that prevents the Si from expanding outward while still allowing Li ions to pass through) in an effort to improve cycleability and SEI layer formation and their influence, as shown in Figs. 19(a)–19(c) [210]. Figure 19(a) shows the formation of an SEI layer on a Si NW, but when the NW expands and contracts the SEI layer breaks down and

reforms, and with cycling this will lead to a large SEI layer being formed around the NW. Figure 19(b) shows a similar process occurring on a Si NT. However, in Fig. 19(c), the use of a mechanical restraint prevents the Si NT from expanding; therefore, a thin and stable SEI layer can be formed.

Cui's group [208] developed crystalline–amorphous core–shell Si NWs for use as a LIB anode. Their approach exploited the fact that amorphous Si (a-Si) has a superior cycling performance compared to crystalline Si (c-Si) [146, 241, 242] owing to the more homogenous volume expansion of a-Si upon Li insertion. The homogenous expansion causes less pulverization than in the crystalline material [133, 241] and also leads to lithiation at slightly higher potential (~220 mV) [146, 151] compared to c-Si (~120 mV) [71, 243]. Li insertion was limited by limiting the charge potential to allow only the amorphous shell material to participate in Li^+ storage while the crystalline

core remained pristine as a mechanical support and also allowed for efficient electron transport pathways. The core–shell NWs demonstrated a high charge storage capacity ($\sim 1,000 \text{ mAh}\cdot\text{g}^{-1}$) with ~90% capacity retention over 100 cycles. The group further developed core–shell structures that employ double-walled silicon nanotube battery anodes to offer superior stability during charge–discharge operations. This was achieved through solid–electrolyte interphase control [210]. The cycleability of the Si NT anode with the mechanical restraint is shown in Fig. 19(d), exhibiting a capacity of $\sim 600 \text{ mAh}\cdot\text{g}^{-1}$ after an incredible 6,000 cycles.

The core–shell system can also employ different elements as the core and shell structures, and can therefore exploit the different properties of various elements as either the core or the shell structure. A-Si was deposited on Cu nanopillars with varying diameters and on a Cu film, as shown in Fig. 20(i). These were then investigated as anodes for LIBs, and

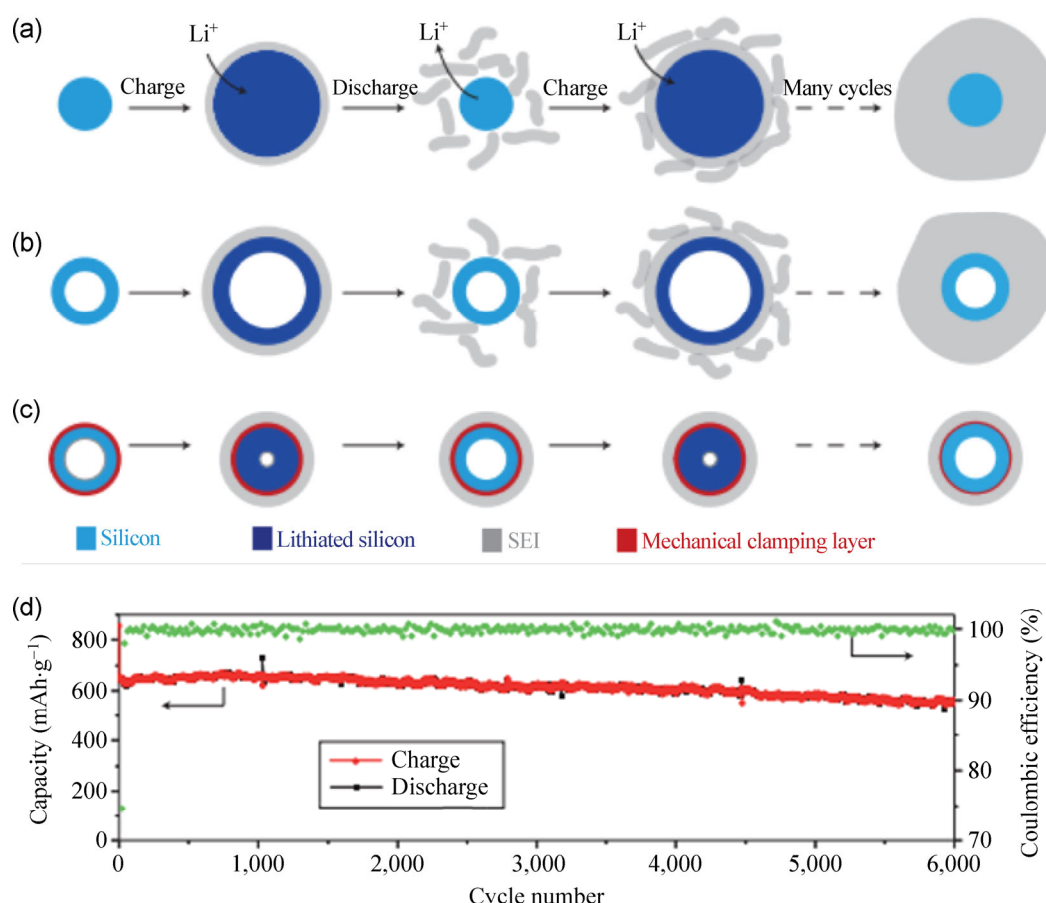


Figure 19 (a)–(c) Schematic of SEI formation on Si surfaces showing the importance of a mechanical constraint on the Si anodes. (d) The capacity retention of Si NTs with an SiO_x outer clamping layer over 6,000 cycles. Reproduced with permission from Ref. [210], © 2012 Nature Publishing Group.

it was shown that the Cu nanopillars with a diameter of 250 nm retained the greatest capacity after 100 cycles when compared to 500-nm-diameter nanopillars and an a-Si–Cu film. The reason for this was that the 250-nm-diameter pillars had sufficient space between each other in which to expand and contract freely, whereas the 500-nm-diameter nanopillar exhibited slight cracking and the film had widespread cracking after 100 cycles [244].

Cui et al. [207] synthesized C–Si core–shell NWs via CVD of a-Si onto carbon nanofibers (CNF). The C core acted as an electron transport pathway and as a mechanical support. However, C, owing to its small capacity, had almost no structure or volume change as a result of Li⁺ insertion. These NWs were shown to have a high Li storage capacity of ~2,000 mAh·g⁻¹ and good cycling life.

As mentioned earlier, porous silicon electrodes and their preparation can influence the performance of LIB anodes [183, 245]. This was demonstrated by a synthetic method that allowed the formation of mesoporous Si–C core–shell NWs using a SBA-15 template. The as-synthesized NWs had a diameter of 6.5 nm and well-ordered mesopores of 2.3 nm in size. Due to this alignment, excellent capacity retention was maintained after 60 cycles, the initial capacity was 3,163 mAh·g⁻¹, and the capacity retention after 80 cycles was 87%.

The core–shell structure can be used on NPs as well as NWs, and Si–C core–shell NPs were synthesized [246]. The initial capacity of the Si–C electrode was 1,328 mAh·g⁻¹ and a high retention of 97% was obtained after 30 cycles at a current density of 50 mA·g⁻¹. It was also demonstrated that the conductive C shell reduced the cell impedance and allowed buffering of the volume changes in Si. High cycle stability and a consistently high CE (> 96%) were exhibited owing to the existence of a C shell.

Various techniques can be used to form core–shell structures and Jung et al. [181], by modifying the resorcinol-formaldehyde microemulsion polymerization technique, prepared a Si–C core–shell structure [101, 247]. The Si–C core–shell powder exhibited an improved performance when compared to bare Si. Core–shell Si–SiO_x nanocomposites have also been synthesized using a sol–gel method and a heat-treatment process, and their electrochemical properties

as anode materials for LIBs were investigated. It was shown that the capacity retention of the core Si NPs was improved with the presence of the SiO shell. This was due to the SiO layer acting as a barrier to prevent the aggregation of the Si NPs and also acting as a buffer to the volume change of the Si particles [248].

The influence of shell thickness in a core–shell system was investigated by Li et al. [57], who fabricated Si–Ge core–shell nanoarrays. Here, the Ge film was deposited on Si nanorods via radio frequency (RF) magnetron sputtering using a Ge target. The Si nanorods that had Ge deposited at higher powers (hence having a thicker Ge layer) exhibited higher capacities than the Si nanorods that had Ge deposited at a lower power (having a thinner Ge layer). This is due to the higher Li ion diffusivity and electronic conductivity of Ge compared to Si and the Ge restricting the formation of SEI layers on Si [249].

A Si-polyaniline core–shell composite was synthesized [250]. The initial charge capacity was shown to be ~4,370 mAh·g⁻¹ at a rate of 0.1C. For over 100 cycles, the capacity remained steady at ~890 mAh·g⁻¹. The polyaniline content in the electrodes was varied and it was found that the charge and discharge capacity increases with increasing polyaniline content. This increase in capacity was attributed to the polyaniline being able to accommodate the Si expansion and contraction and hence improving capacity retention.

More than two elements can be used in the core–shell structure and Wang et al. [251] investigated this and fabricated Cu–Si/Ge core–shell NWs by depositing a Si/Ge film onto the surface of Cu NW arrays via a co-sputtering method. The ratio of Si to Ge could be varied by changing the sputtering power of the Si and Ge targets and the Cu acted as a conducting pathway. The authors observed that the capacity retention of the NWs increased as the content of Ge increases to 40%, but decreased when the Ge content rose above this value. The Si_{0.6}Ge_{0.4} electrode was cycled at a rate of 4 A·g⁻¹ for 75 cycles, and the initial capacity was ~4,000 mAh·g⁻¹ but this fell quickly and plateaued at 1,600 mAh·g⁻¹ for 75 cycles.

Si NPs wrapped by crumpled graphene shells were investigated and electrochemically compared to unwrapped Si NPs [252]. The CE during the first cycle was shown to be ~73% for the wrapped Si compared



to ~37% for the unwrapped Si. The capacity of the wrapped Si at a charge rate of $1 \text{ A}\cdot\text{g}^{-1}$ was shown to be $\sim 900 \text{ mAh}\cdot\text{g}^{-1}$ after 250 cycles, compared to $\sim 150 \text{ mAh}\cdot\text{g}^{-1}$ for the unwrapped Si. The difference in the performances of the electrodes was attributed to the graphene shell, which accommodates the expansion of the Si particles during the charging process, thus protecting the Si.

Chen et al. [253] electrodeposited Si onto a tobacco mosaic virus/nickel (TMV1cys/Ni) anode. This anode exhibited an initial capacity of $2,300 \text{ mAh}\cdot\text{g}^{-1}$ and a capacity of $1,200 \text{ mAh}\cdot\text{g}^{-1}$ after 173 cycles. These values represent superior cycling to other Si NTs reported in the literature [254]. The authors stated that the superior capacity retention and CE demonstrated that the nickel core can greatly improve the structural integrity and conductivity of the anode. The high electronic conductivity of nickel and the large contact area between Si and nickel in the TMV1cys/Ni/Si structure allowed for uniform Li insertion and extraction within the Si and reduced stress on the Si NWs.

Different elements can be compared as prospective shell materials. Mitlin's group [116] coated Si NTs with TiO_2 , Al_2O_3 , and TiN via atomic layer deposition (ALD). After 100 cycles at a charge rate of 0.2C , the uncoated Si NTs exhibited a capacity of $1,665 \text{ mAh}\cdot\text{g}^{-1}$, compared to $1,774 \text{ mAh}\cdot\text{g}^{-1}$, $1,921 \text{ mAh}\cdot\text{g}^{-1}$, and $1,936 \text{ mAh}\cdot\text{g}^{-1}$ for Si/TiN, Si/ Al_2O_3 , and Si/ TiO_2 NT electrodes, respectively. The authors stated that the high ionic conductivity and electrical conductivity of TiO_2 were the reasons for the improved performance of that anode compared to the other anodes. Figure 20(ii) shows TEM images and elemental mapping of (a) Si NTs, (b) Si NTs coated in TiO_2 , and (c) Si NTs coated on both sides by TiO_2 . The line scan profile in Fig. 20(ii)(d) shows the hollow structure of the Si NTs while Fig. 20(ii)(e) shows the Ti signals on the diameter of the Si NTs. TiN has also been used as a coating to improve the performance of other Si electrodes, where the performance of Si NPs was enhanced as a result of increased conductivity due to a TiN coating and a more stable SEI layer was formed compared to bulk Si NPs [255].

The use of core–shell architectures represents a versatile platform for improving the performance

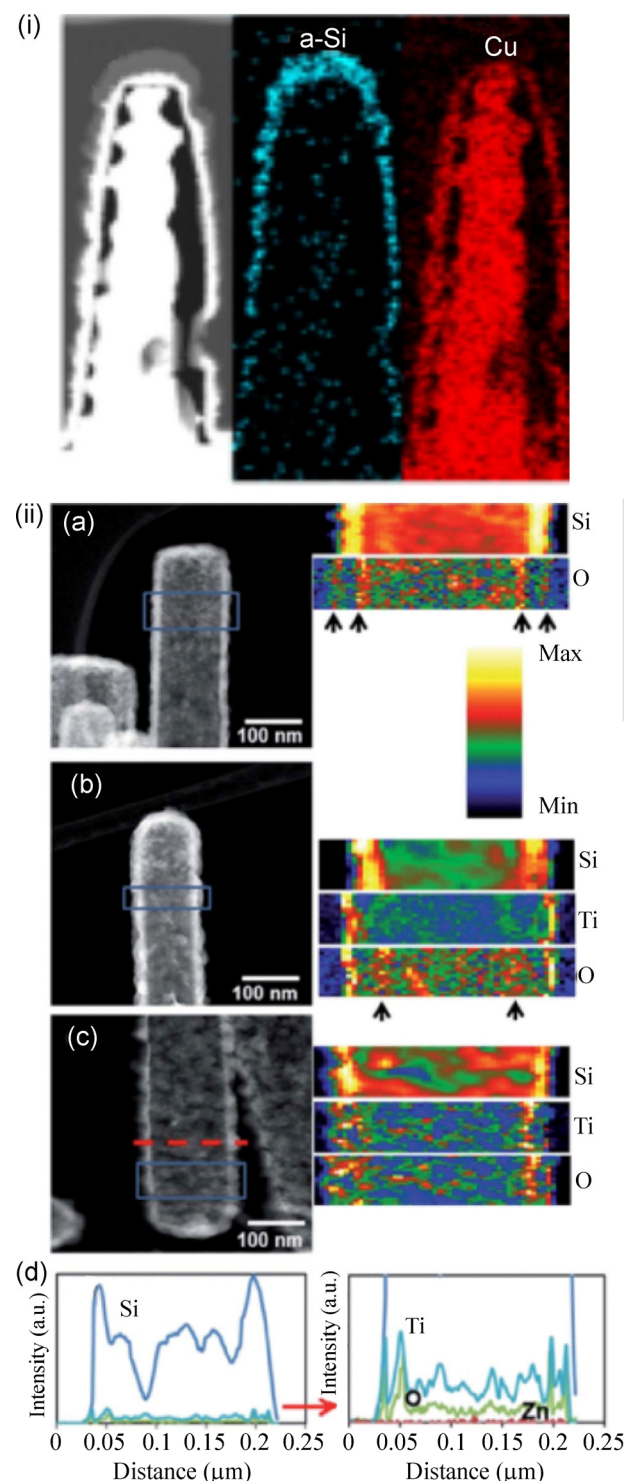


Figure 20 (i) EDX elemental mapping images of a-Si coated Cu NWs. Reproduced with permission from Ref. [244], © 2014 American Chemical Society. (ii) HAADF images and EELS maps of (a) uncoated Si NTs, (b) Si NTs/ TiO_2 , and (c) TiO_2 /Si NTs/ TiO_2 ; (d) a line scan profile along the nanotube diameter (red dashed line) showing the hollow core–shell structure for TiO_2 /Si NTs/ TiO_2 . Reproduced with permission from Ref. [116], © 2013 Royal Society of Chemistry.

of LIB anode materials. For alloying materials that undergo large volume changes during Li insertion/extraction, the use of inactive scaffold materials may impart increased mechanical stability and thus improve performance. However, it should be noted that the addition of inactive materials will decrease gravimetric capacities with a trade-off between initial capacity and cycle life. Nevertheless, the use of core–shell architectures is extremely useful as it can be used to form materials that allow control over SEI formation and that also possess increased conductivity and cycling stability.

4.4 MAC-etched Si NWs for Li-ion batteries

Si NWs formed using top-down approaches have also been probed for LIB applications. Peng et al. [78] investigated large area, wafer-scale Si NW arrays, prepared by MAC etching, for use as anode materials for rechargeable LIBs. They showed that the conductivity of a single NW is greater than that of the original wafer and attributed this to surface defects on the NW. The greater conductivity of the single NW versus that of the bulk is significant in terms of Li insertion and capacity retention. They achieved a capacity of $0.55 \text{ mAh} \cdot \text{cm}^{-2}$, which faded with cycling. The peak current response in the CV scans was also reduced with cycling.

Using a similar approach, MAC-etched single crystal p-type (100) Si wafers were used to create Si NWs, which demonstrated an initial charge capacity of $3,653 \text{ mAh} \cdot \text{g}^{-1}$ and an initial discharge capacity of $2,409 \text{ mAh} \cdot \text{g}^{-1}$ when cycled between 2 and 0.02 V [192]. A stable reversible capacity of $\sim 1,000 \text{ mAh} \cdot \text{g}^{-1}$ was maintained after 30 cycles and the CE was above 90% after the first cycle. The current response from the CV cycles increased with cycling, indicating an activation effect. The CV results are shown in Fig. 21(i).

Porous MAC-etched Si NWs were shown to perform electrochemically better than their non-porous equivalents, as shown in Fig. 21(ii) [256]. The superior cycling of the porous Si NWs (red squares) over the non-porous Si NWs (blue circles) was attributed to the nanosized pores in the NWs. The pores were said to act as a buffer layer that can alleviate the volume changes during Li insertion and extraction and hence improved the capacity retention of the Si NWs over many cycles.

Materials with a defined porosity can potentially compensate for large swing changes in the morphology of the active material [257]. Theoretical and experimental studies were performed using porous doped MAC-etched Si NWs for LIB applications. The simulations showed that porous Si with a large pore size and high porosity can maintain its structure after Li^+ insertion while experiencing low stress. Having Si maintain its structure is crucial in achieving a high capacity and long cycle retention. The capacity remained stable above $2,000$, $1,600$, and $1,100 \text{ mAh} \cdot \text{g}^{-1}$ at varying charge rates, even after 250 cycles. The transition from c-Si to a-Si by Li insertion peaks on the first and second cycles was illustrated using CV measurements. The second CV cycle showed a Li insertion peak at 0.15 V, indicating a crystalline to amorphous transition [142, 158]. TEM images of the NWs (a) before and (b)–(d) after lithiation are shown in Fig. 21(iii). The NWs are crystalline before cycling but are shown to have regions of both amorphous and crystalline Si post cycling.

A Li-polymer Si NW battery concept called LIPOSIL was demonstrated by Vlad et al. [141]. Precise design of Si NWs was achieved through controlled MAC etching. The conformal Cu-wrapped Si NWs exhibited improved capacity retention and rate capabilities as compared to pristine NWs. The approach provides a solution for electronics waste management by allowing a second life for Si via LIPOSIL anodes recycled from end-of-life Si chips.

MAC etching has also been used in combination with block copolymer patterning to form diameter-controlled non-porous and porous Si NWs. The porous Si NWs exhibited excellent cycling retention over 50 cycles and a high storage capacity of $\sim 1,500 \text{ mAh} \cdot \text{g}^{-1}$. The nanoporous Si anode materials retained their initial morphology after 50 cycles by alleviating the large volume expansion during the lithiation/delithiation process [256].

Wang et al. [258] MAC-etched Si wafers to produce Si NWs and then deposited graphitic C sheets on the Si NWs. The Si–C hybrid was then delaminated through NaOH treatment. The pristine Si NW electrode had an initial capacity of $\sim 2,500 \text{ mAh} \cdot \text{g}^{-1}$, but this fell to $500 \text{ mAh} \cdot \text{g}^{-1}$ after 200 cycles at rate of 0.2C. The Si NW anode with a C coating retained a capacity of



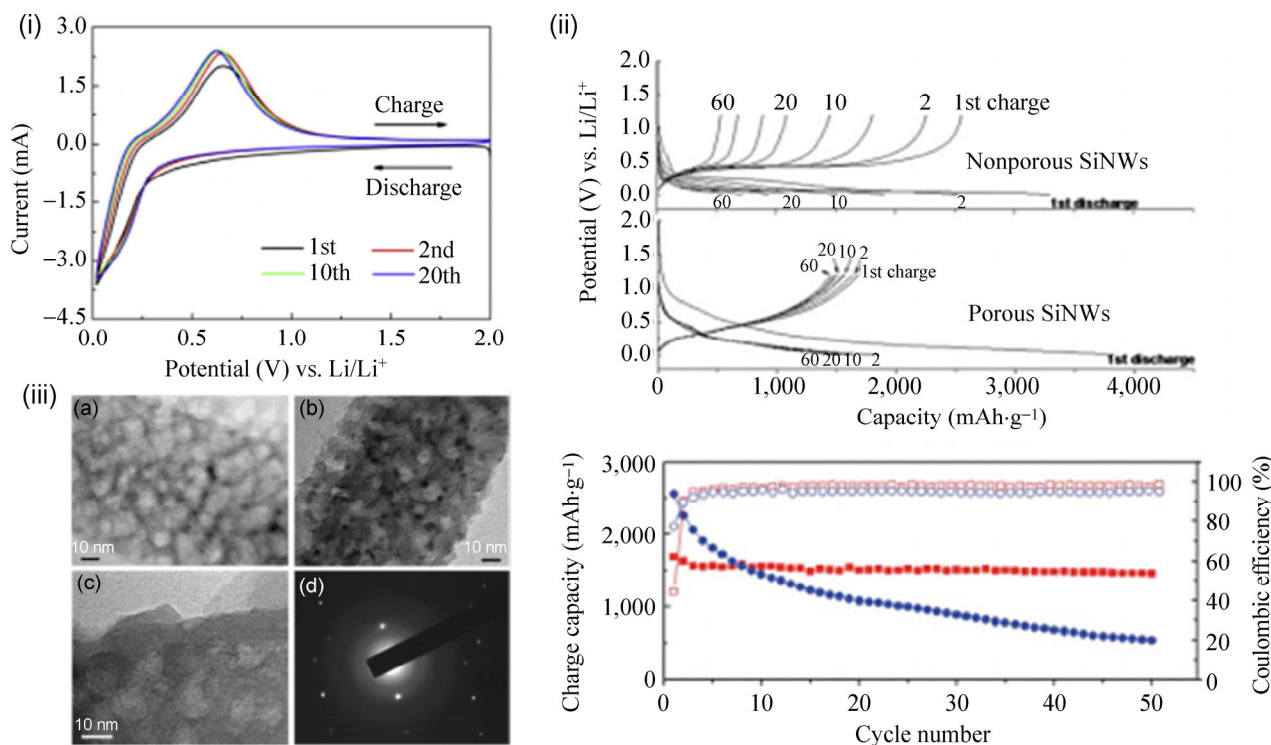


Figure 21 (i) CV for the Si NW electrode at a scan rate of $1 \text{ mV}\cdot\text{s}^{-1}$. Reproduced with permission from Ref. [192], © 2010 Elsevier B.V. (ii) Voltage profiles of (top) nonporous and (bottom) nanoporous Si NW electrodes at a rate of 0.1C . (b) Charge capacity and CE of the porous and non-porous electrodes (squares: porous Si NWs; circles: nonporous Si NWs). Reproduced with permission from Ref. [256], © 2011 Royal Society of Chemistry. (iii) TEM images of Si NWs (a) before and (b) after lithiation after 10 cycles; (c) enlarged TEM image of (b) showing the amorphous Si structure; (d) electron diffraction pattern showing that the black spots in (b) are crystalline Si. Reproduced with permission from Ref. [158], © 2012 American Chemical Society.

800 mAh·g⁻¹ after 200 cycles. The authors stated that the improved capacity was due to the increased conductivity supplied by the C coating. The influence of coating electrodes with C will be discussed in Section 4.6.

A mesoporous Si sponge was fabricated by etching heavily doped Si wafers in a HF:ethanol solution, and extensions to metallurgical-grade low-cost silicon can be MAC-etched by utilizing the inherent metal impurities within the material [259]. The expansion of the anode was limited to 30%, which enabled the Si anodes to retain a capacity of $> 400 \text{ mAh}\cdot\text{g}^{-1}$ for 1,000 cycles. It was also shown that pre-lithiating the Si anodes prior to electrochemical testing reduces the irreversible capacity loss during the first cycle [81]. More recent investigations propose silicon sponges based on micro- or nanoporous silicon from particles as a dedicated anti-pulverization material [109], but further work is required to assess its general application in a wider range of electrolytes and paired cathode materials.

There have been a limited number of studies on the utilization of MAC-etched Si NWs, in spite of the inherent benefits of nanostructuring Si with the control of doping density, conductivity, and degree of porosity. Porous Si NWs have been shown to perform better in some systems than non-porous Si NWs, and it has been shown that a Cu or C coating on the NW improves capacity retention with cycling.

4.5 Si nanostructures: The effect of doping on the performance of LIB anodes

The influence of doping on the performance of bulk and non-nanosized Si anodes was discussed in Section 3.4, with there being some contradictions as to whether doping improves the performance of the Si anode or not. The influence of doping on the performance of nanostructured Si anodes is discussed in this section.

It was found that one could better retain the capacity of Si NWs, particularly at higher C-rates,

when they are doped (and thus made more conductive), while the charge capacity is kept almost the same, as shown in Fig. 22(a) [204]. It was speculated that the observed capacity retention characteristics for doped Si NWs at various C-rates signified that the conductivity of Si NWs was closely related to the reaction kinetics of Li-charge/discharge with Si NWs, rather than thermodynamics. Also shown in Fig. 22(a) is the higher resistivity of several undoped Si NWs compared to doped Si NWs.

Doped and undoped Si NWs were grown via CVD with an Au catalyst on stainless steel current collectors [260]. The initial capacity exhibited by the undoped

NWs was $2,014 \text{ mAh}\cdot\text{g}^{-1}$ and retained a capacity of $>1,500 \text{ mAh}\cdot\text{g}^{-1}$ after 20 cycles at a C/20 rate. When limiting the discharge capacity (by limiting the discharge potential) and using C-rates varying between C/20 and C/10, a capacity of $321 \text{ mAh}\cdot\text{g}^{-1}$ for ~600 cycles was achieved, whereas the doped NWs achieved a capacity of $\sim 1,000 \text{ mAh}\cdot\text{g}^{-1}$ for 200 cycles at a C/10 rate at limited discharge. It was also shown that n-type Si NWs performed better than undoped Si NWs, which in turn performed better than p-type Si NWs, as shown in Fig. 22(b). This is in agreement with the work of Peng et al. [194], who calculated a high energy barrier (0.88 eV) of Li surface intercalation for undoped and

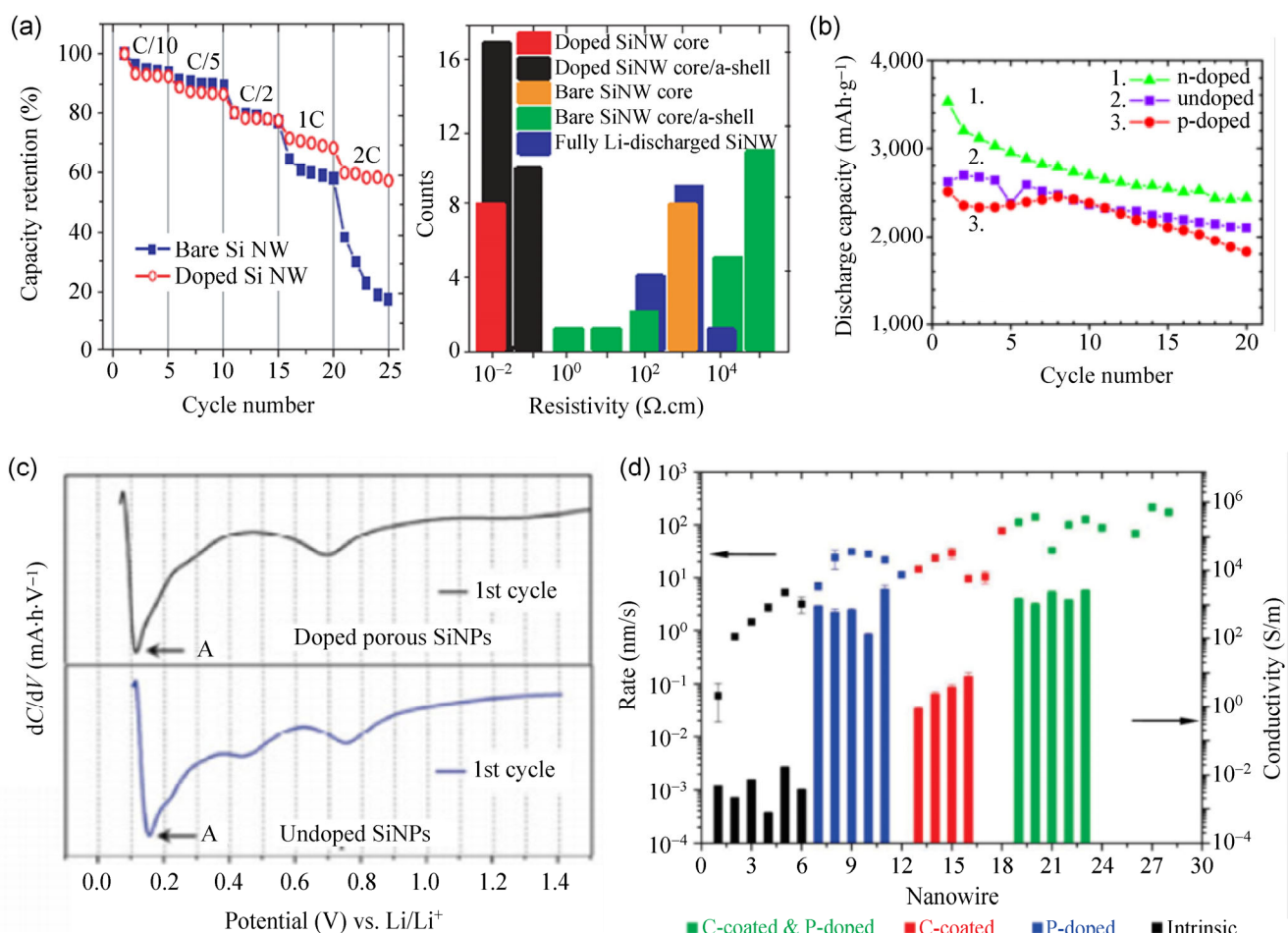


Figure 22 (a) The capacity retention in terms of the percentage of bare Si NWs and P-doped Si NWs over 25 cycles. The statistics for the resistivity of various individual Si NWs are measured in the inset. Reproduced with permission from Ref. [204], © 2010 American Institute of Physics. (b) The effect of doping (n- and p-type) on the capacity and cycle life of the Si NW anode in an organic electrolyte. The performance of the nominally undoped NWs is shown for comparison. Reproduced with permission from Ref. [260], © 2012 Elsevier B.V. (c) Differential capacity curves of doped porous Si NPs and undoped nonporous Si NPs in the charge branch of the first cycle. Reproduced with permission from Ref. [185], © 2013 Tsinghua University Press and Springer-Verlag Berlin Heidelberg. (d) Lithiation speed and kinetics for different Si NWs. Comparison of reaction front propagation speeds and conductivities of the intrinsic, P-doped, C-coated Si NWs and C-coated, P-doped Si NWs. The charging rate was improved by the enhanced electronic conductivity from doping and C coating. Reproduced with permission from Ref. [261], © 2011 American Chemical Society.

B-doped Si that retards fast Li ion transport.

Ge et al. [185] electrochemically tested doped Si NPs against undoped Si NPs. They found that the intercalation voltage was 0.03 V lower for the doped Si than for the undoped Si, as shown in Fig. 22(c). They attributed the lower intercalation voltage in doped Si to the higher conductivity of particles due to B doping and the relatively lower intercalation energy of Li in doped Si, which they derived from a first-principles density functional theory calculation.

Liu et al. [261] demonstrated an ultrafast and full electrochemical lithiation of individual Si NWs by applying C, or a dopant (in this instance P), or combining both doping and C coating. While the lithiation of the doped or coated NWs was fast, the lithiation of intrinsic Si NWs was slow and incomplete. The C-coated and/or P-doped Si NWs exhibited a charging rate 1–2 orders of magnitude faster than for the undoped Si NWs. Figure 22(d) compares the axial charging rates (defined as the reaction front speed in the first charging process) for four types of Si NWs. The average speeds were 2.3, 20.5, 27.5, and 117.4 nm·s⁻¹, respectively, and the average conductivities were 5.95×10^{-3} , 1.05×10^3 , 3.76, and 1.77×10^3 S·m⁻¹, respectively, for the four samples. It is clear that either doping the NWs or coating the NWs with C can improve the first cycle charging rate with respect to the intrinsic Si NWs.

P-doped and undoped Si NWs have also been grown via a radio-frequency plasma-enhanced CVD method. After 30 cycles at a 2C rate, the undoped Si NWs had a capacity of 1,170 mAh·g⁻¹, whereas the doped Si NWs had a capacity of >1,900 mAh·g⁻¹. When varying the C-rate between 0.1C and 2C, the doped NWs exhibited a higher capacity and a higher CE than the undoped NWs in each instance. The authors speculated that the presence of the dopant may help to maintain the structural stability of Si NWs during Li insertion and extraction, leading to a better electrochemical response to reversible alloying with Li compared to the undoped Si NWs.

The doping of Si anodes has been shown to lower the Li insertion potential in Si anodes (which would improve the power in a full LIB). It was also shown to improve capacity retention over undoped Si anodes, especially at higher applied currents. N-type NWs were

shown to perform better than undoped NWs but, curiously, it was shown that p-type NWs performed worse than undoped NWs (which are intrinsically n-type). In p-type electrodes, electron (minority carrier) withdrawal from the conduction band is less efficient at positive cell potentials (forward biased) and implies that doping of NWs with certain dopants would worsen the performance of the Si anode.

In effect, the doping level and type (donor or acceptor) strongly controls the charge transfer processes, including those that result in reversible alloying with cations such as lithium in battery anodes. For a given electrolyte (redox potential) and cathode pairing (or indeed versus lithium metal), the knowledge summarized here from tests conducted using wafer-scale silicon with a defined resistivity, doping density, and surface crystal orientation is invaluable when transposed to nanoscale systems where the doping, orientation, and resistivity can be uniquely different between similar structures (such as NWs) depending on their growth methods. Bottom-up methods that are practical for many laboratories have inherent difficulties in controlling the orientation of the primary surface area facets in the countless billions of wires grown during each time step in many laboratories, making rational assessment of their response a statistical function, although they are somewhat reproducible owing to the large number of nanostructures in the composite electrode. Additionally, even in pristine NWs, doping levels vary radially from center to outer surface, making doping level control at the surface between n-type and p-type more difficult to control than for top-down NWs etched using MAC etching, for example. Controlling the electrical characteristics of semiconducting anode materials is as important as the benefits of size reduction, because the semiconductor–solution interface dominates the charge transfer mechanisms.

4.6 Si nanostructures: The influence of conductive additives

For intrinsic Si-based nanostructures, the addition of conductive additives is an important step in improving LIB anode performance. Carbon is widely used in negative electrodes to reduce the inner electrical resistance of the anode [179]. Carbon has

high electrical conductivity, is non-toxic, and is available in high purity and large quantity. Xu et al. [190] demonstrated composite LIB anodes (graphite with 15% Si NWs by weight) with initial capacities of $\sim 800 \text{ mAh}\cdot\text{g}^{-1}$. A reversible capacity of approximately $512 \text{ mAh}\cdot\text{g}^{-1}$ was observed after 10 cycles for the composite anode. The authors showed that the NWs within the graphite matrix grew in diameter upon lithiation and remained intact after several charge/discharge cycles without agglomeration or pulverization. Voltammetric analysis indicated a crystalline to amorphous transition on the first cycle, and comparisons with pure graphite anodes suggested that the majority of capacity loss was associated with losses in Si capacity.

Another Si/C composite study examined a C-coated nanosized Si/graphite composite (nano-Si/C). This composite was dried in an oven at 80°C (Si/C) and a bare Si electrode (bare Si) was used as an anode for the LIB [262]. The initial charge capacities of the nano-Si/C, Si/C, and bare Si anodes were 2,009, 1,757, and $2,540 \text{ mAh}\cdot\text{g}^{-1}$, respectively (Fig. 23(a)). However, the bare Si exhibited a CE of only 30% on the first cycle and its discharge capacity was lower than the other two electrodes. The authors attributed this to poor electrical conductivity between the Si particles. After 20 cycles, the nano-Si/C anode had a capacity of $1,076 \text{ mAh}\cdot\text{g}^{-1}$, compared to $\sim 400 \text{ mAh}\cdot\text{g}^{-1}$ for the Si/C anode and $\sim 100 \text{ mAh}\cdot\text{g}^{-1}$ for the bare Si anode, and it also had a higher CE.

Composite electrodes composed of Si NWs, amorphous C, and carbon nanotubes (CNT) were synthesized using an SFLS method [205]. The uncoated SFLS-grown Si NWs and those mixed with the CB electrode performed poorly electrochemically. The SFLS Si NWs that were C-coated and mixed with CB also suffered from fast degradation, but retained higher capacities than the uncoated Si NWs. The C-coated NWs and those mixed with multiwalled CNTs (MWCNT) with an additional NT overcoating layer electrode were found to display even higher capacities, as shown in Fig. 23(b). After 45 cycles, the electrode with the MWCNT overcoat had a higher charge capacity of $1,300 \text{ mAh}\cdot\text{g}^{-1}$ when compared to the electrode without the overcoating, which had a capacity of $\sim 1,200 \text{ mAh}\cdot\text{g}^{-1}$.

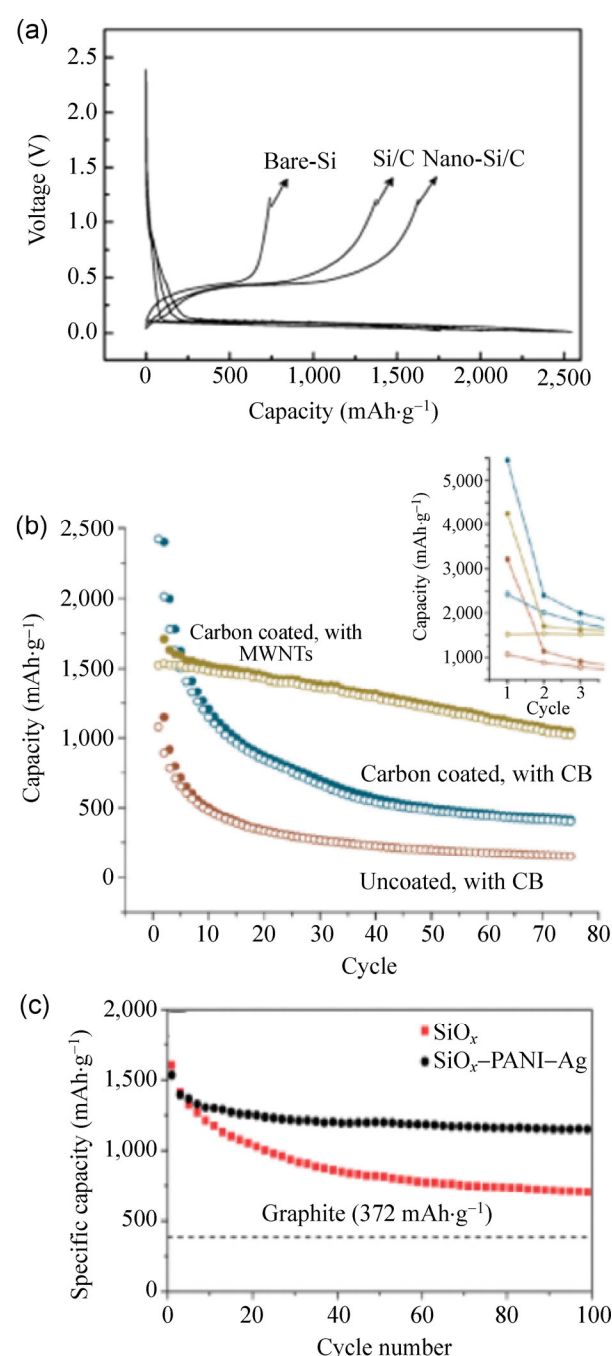


Figure 23 (a) The first charge and discharge curves of the nano-Si/C, Si/C, and bare Si electrodes. Reproduced with permission from Ref. [262], © 2013 Tsinghua University Press and Springer-Verlag Berlin Heidelberg. (b) Capacity vs. cycling data for SFLS-grown Si NWs uncoated and mixed with CB, C-coated and mixed with CB, and C-coated and mixed with MWCNTs with an additional nanotube overcoat layer. Reproduced with permission from Ref. [205], © 2010 American Chemical Society. (c) Performances (charge capacities) of $\text{SiO}_x\text{-PANI-Ag}$ electrodes after a large number of cycles at $100 \text{ mAh}\cdot\text{g}^{-1}$. Reproduced with permission from Ref. [264], © 2013 Royal Society of Chemistry.

VLS-grown NWs were then compared to SFLS-grown NWs with the MWCNT coating. The VLS NWs retained a capacity of ~3,000 mAh·g⁻¹ after 30 cycles, whereas the SFLS NWs only retained 1,500 mAh·g⁻¹. The author suggested the VLS-grown NWs performed better because the quality of the SFLS-grown Si NWs may be less than that of the VLS-grown Si NWs and the SFLS-grown NWs have a polymeric phenylsilane coating that may act as a barrier to Li-ion insertion.

In a similar approach aimed at improving the conductivity of Si-based anodes, Zhou et al. [263] designed a Si NP–C NP/graphene composite. The initial discharge and charge capacities were 2,959 and 4,572 mAh·g⁻¹, respectively based on the mass of Si. The anode retained a capacity of 1,521 mAh·g⁻¹ after 200 cycles. Two other electrodes were tested; Si/graphene electrodes and Si/graphene + C electrodes formed via a different method whose capacities faded to ~0 mAh·g⁻¹ after 50 cycles, which was attributed to large volume change.

In an alternative to the use of conductive C, nanoporous SiO_x microparticles were coated with a polyaniline (PANI)-Ag shell by Zhange et al. [264]. They were electrochemically examined and compared to bare nanoporous SiO_x microparticles. After 100 cycles, the SiO_x–PANI–Ag electrode retained a capacity of 1,150 mAh·g⁻¹, whereas the bare SiO_x electrode only had a capacity of 700 mAh·g⁻¹, as shown in Fig. 23(c). The author attributed the difference in performances to the high electronic conductivity of the PANI–Ag shell.

Porous Si–C nanorods were prepared as an anode for LIBs [265]. This electrode was compared to mesoporous Si and bare C electrodes. The initial capacities were shown to be ~800 mAh·g⁻¹, ~1,400 mAh·g⁻¹, and ~2,500 mAh·g⁻¹ for the bare C, Si–C, and mesoporous electrodes, respectively. The initial CE was higher for the Si–C electrode compared to the other two electrodes. At a current density of 100 mA·g⁻¹, the Si–C electrode exhibited a capacity of ~600 mAh·g⁻¹ after 225 cycles. In comparison, the mesoporous Si and bare C electrodes fell to capacities of < 450 mAh·g⁻¹ after 30 and 50 cycles, respectively. It was stated that the improved performance was due to the intimate contact between the Si and C at nanoscale dimensions, which afforded excellent accessibility to the active materials.

Graphene-wrapped Si NWs were shown to have a superior capacity retention compared to Si NWs that were not wrapped in graphene [266]. The graphene coating improved electron diffusion and conductivity of the Si NWs, and the core/shell structure accommodated the Si expansion during Li insertion and extraction, thus improving the capacity retention when compared to uncoated Si anodes.

Ag/PEDOT was also used as a conductive polymer surface on Si NWs to improve their performance. After 100 cycles, there was an 80% capacity retention for the PEDOT Si NWs versus a 30% capacity retention for the bare Si NWs. The PEDOT coating was proposed to improve capacity retention of the Si NWs by mechanically and electrically binding the porous Si/Li_xSi structure together during lithiation/delithiation.

A Si oxycarbide (SiCO) powder was investigated for use as an LIB anode and two different conductive additives (CB and CNTs) were used [267]. For the first cycle, the SiCO–CB electrode had a capacity of 1,050 mAh·g⁻¹, whereas the SiCO–CNT electrode exhibited a capacity of 1,466 mAh·g⁻¹. After 40 cycles, the SiCO–CB electrode retained a capacity of 630 mAh·g⁻¹ compared to 846 mAh·g⁻¹ for the SiCO–CNT electrode, with the SiCO–CNT electrode exhibiting a higher CE than the SiCO–CB electrode. The SiCO–CNT electrode also exhibited superior reversible capacities when the applied current was increased in comparison to the SiCO–CB electrode. The higher capacity and superior performance of SiCO–CNT electrodes was attributed to the intimate contact between the CNTs and the surface of the SiCO particles and the low electronic conductivity of CB.

Electrodes containing a mixture of Si NPs, CNFs, multiwalled nanotubes (MWNT), and polyacrylonitrile (PAN) were carbonized [94]. These electrodes were electrochemically tested against a similar electrode that was not carbonized, and with a carbonized electrode that did not contain the CNFs and MWNTs. It was found that the carbonized electrode without MWNTs/CNFs exhibited the best capacity retention and had a capacity of 1,550 mAh·g⁻¹ after 120 cycles. In that work, charge transfer resistances of both electrodes with MWNTs/CNFs constantly increased during the cycling tests. The addition of MWNTs/CNFs increased the electrode capacity in early cycles but had a negative

impact on the long-term cycling stability of the Si–C electrodes. This study shows that the addition of conductive additives may not always improve the capacity of Si anodes and that careful thought must be put into what type of additives to add into a system.

Reduced graphene oxide (RGO) has also been used to improve the cycling performance of Si-based anodes. A Si monoxide-C-RGO nanocomposite was fabricated by Guo et al. [268]. The anodes were electrochemically tested against nanocomposites not containing RGO. After 100 cycles, the electrode containing RGO had a capacity of $1,284 \text{ mAh}\cdot\text{g}^{-1}$, whereas the electrode without the RGO exhibited a capacity of $757 \text{ mAh}\cdot\text{g}^{-1}$. The authors stated that the improvement was due to RGO creating a 3D conducting network. RGO was also used in a Si honeycomb electrode, which exhibited an impressive electrochemical performance. It retained a capacity of $>1,000 \text{ mAh}\cdot\text{g}^{-1}$ after 50 cycles. This performance was attributed to the honeycomb and RGO structure, which increases the conductivity of the anode [63].

It was shown for several Si structures that the addition of a conductive additive improves the electrochemical performance of the Si anode. Recent *in situ* transmission electron microscopy (TEM) observations revealed that carbon skins enhance the lithiation rate with Si and constrain the final volume expansion [269]. The improved performance is believed to result from the direct influence on the rate of reversible alloying reactions and the mitigation of volume changes, which in composites are reduced for the volume fraction comprising alloys with materials other than silicon.

5 Future directions

In energy storage applications, particularly as a possible alternative for LIB anodes, the low dimensionality and porosity afforded by (electro)chemical etching is in principle beneficial for accommodating volumetric expansion and contraction of the Si lattice during Li insertion [270] and extraction, and with electronic transport theoretically unaffected, an improvement in battery anode performance has been found using nanoscale Si [11, 271, 272]. Knowledge acquired from the study of bulk-scale silicon and its alloys has

proven invaluable in assessing the primary parameters that influence the overall electrochemical response. Many of these characteristics are applicable to nanoscale silicon, but some still need to be proven in full cell configurations.

Many challenges still face the proliferation of Si-based anodes in LIBs, although some lower cost forms of silicon have been commercialized. Power sources are also needed to store energy from photovoltaics and smaller devices such as sensors and electronics. The cell pairing of LiCoO_2 and Si has one of the highest volumetric energy densities possible ($\sim 3,300 \text{ Wh/L}$) for any Li-ion or Li–S technology, but is rarely covered in the literature. Some important considerations that remain open topics for the lithium-ion battery nano-materials community, particularly for nanoscale silicon material systems and related anode investigations, include:

1. The determination of important material pairings to use for anode/cathode pairs for systems that do not use the standard lithiated graphite anodes. The dearth of nanostructured Si anodes in the literature matched with currently emerging cathode materials [111, 273] indicates the level of research and development that will be necessary.

2. In a particular electrolyte, the influence of surface chemical reactivity, electronic conductivity via the doping profile, the exposure of silicon facets with lower chemical potentials for Li (de)alloying, and contributions from surface-bound ligands, shape-influencing species, or Li-conductive coatings that are stable in electrolytes, are important for low-voltage anodes. These factors also become important for new metal–Si alloys formed by VLS and other bottom-up growth methods.

3. Detailed knowledge of how the individuality of nanoscale silicon structures can be optimized for new electrolytes and additives and their pairings with higher voltage ($> 4 \text{ V}$) positive electrode materials, particularly for nanoscale structures designed with complex compositions and geometries. Furthermore, as anodes comprise random mixtures of active materials, conductive additives, binders, and a large number of nanoscale materials, another question is whether high-quality scientific investigations of more and more complex nanostructures and compositional



control can really be effective in alleviating the remaining challenges to Li-ion technology, which is reaching maturity in useful power delivery and cycle life.

4. An understanding of SEI formation processes in new electrolytes in the myriad of forms of nanoscale silicon with various surface free energies, the influence of additives on new Si-metal (Sn, Ge, etc.) alloy nanostructures, and the true long-term cycling behavior in cathode–anode cells.

5. The adaption of MAC and related etching techniques to influence fundamental charge transfer processes and to create large-area nanoscale silicon and related compounds from thin films deposited on choice current collectors. Such porosity control allows for infilling with other materials that enhance conductivity, provide reversible alloying or intercalation, or indeed have a reduced degree of volumetric expansion with lithium.

6. Accelerated life-time testing of silicon anodes containing cells with a range of possible cathode materials and electrolytes are needed, while quantification of the effects of composition, size, conductivity, and structure on charge rates and long-term cycling in variable power-demand applications are also important.

7. When semiconducting anode materials are electrochemically etched, a depletion or space charge layer overlap can limit the etched features or minimum feature size (in the absence of surface or other states that facilitate long diffusion-length holes that promote further etching). Thus, electrically dead capacitors and pseudocapacitors are possible when etched silicon is used without a metallic current collector, benefiting from potential-controlled charge transfer and the use of double-layer capacitances without the reversible alloying that affects the silicon structure.

Due to its high theoretical capacity, Si is likely to remain an anode of choice for eventual adaption to some future LIBs. The nanostructuring of Si has alleviated some issues experienced with bulk Si as an anode, and the optimization of Si nanostructures as a LIB anode will likely drive further research for the foreseeable future. Theoretical methods may help speed up the development of new chemistries and aid in understanding the response of new materials or alternatively structured materials to Li-, Na-, or

Mg-ion insertion for multiple electron redox events during charging and discharging—for semiconducting anodes, high-density electron extraction from the anode will benefit from high conductivity and n-type materials for higher charge and discharge rates. However, it remains to be seen if insertion of greater amounts of cations at higher rates is possible in some forms of nanostructured silicon without exacerbated swelling or fracturing during cycling.

6 Conclusions

In this paper, the metal-assisted chemical (MAC) etching of silicon (Si) and the investigation of bulk and nanostructured Si for use as anodes for Li-ion batteries (LIBs) was reviewed. Many parameters influence how Si nanowires (NW) form from MAC etching, including the orientation of the Si, the doping density of the Si, and the etching conditions under which the NWs are formed. Moreover, the concentrations of HF, H₂O₂, and AgNO₃, the etching temperature, and the use of anodic aluminum oxide masks in conjunction with etching all influence the structures formed. Thin films and powder electrodes were researched and it is apparent that the use of composite electrodes and the addition of carbon (C) or another conductive element improves the performance of these Si anodes. The response to reversible (de)alloying with lithium and the use of bulk- or wafer-scale silicon, with conductive additives, alloys with other phases, and crystalline and bulk structure forms, offer useful insight into the comparative response of nanoscale analogues, especially when the nanostructures and their various derivatives are formed directly from these bulk forms of silicon.

Nanostructured Si greatly improves on the performance of bulk Si by accommodating for the expansion and contraction of Si, which hinders the utilization of bulk Si as a LIB anode. The performance of nanostructured Si anodes has been shown to be influenced by the addition of a C or a binder, the use of core–shell structures, the addition of additional conductive components, and by the actual size of the Si structures. Doping of the Si anodes has also been shown to improve their electrochemical performance in LIBs. From an in-depth analysis of recent findings,

the mechanism for the varied response of both compositionally, structurally, and electronically different forms of nanoscale silicon has become very clear, with evidence for considerable performance enhancement and a greater depth of understanding that has yielded predicted improvements.

Acknowledgements

WMS acknowledges support under the framework of the INSPIRE programme, funded by the Irish Government's Programme for Research in Third Level Institutions, Cycle 4, National Development Plan 2007-2013. COD acknowledges support from Science Foundation Ireland under Award No. 07/SK/B1232a-STTF11 from the UCC Strategic Research Fund.

References

- [1] Scrosati, B.; Garche, J. Lithium batteries: Status, prospects and future. *J. Power Sources* **2010**, *195*, 2419–2430.
- [2] Goodenough, J. B.; Kim, Y. Challenges for rechargeable Li batteries. *Chem. Mater.* **2010**, *22*, 587–603.
- [3] Tarascon, J. M.; Armand, M. Issues and challenges facing rechargeable lithium batteries. *Nature* **2001**, *414*, 359–367.
- [4] McDowell, M. T.; Lee, S. W.; Nix, W. D.; Cui, Y. 25th anniversary article: Understanding the lithiation of silicon and other alloying anodes for lithium-ion batteries. *Adv. Mater.* **2013**, *25*, 4966–4985.
- [5] Lee, C. L.; Tsujino, K.; Kanda, Y.; Ikeda, S.; Matsumura, M. Pore formation in silicon by wet etching using micrometre-sized metal particles as catalysts. *J. Mater. Chem.* **2008**, *18*, 1015–1020.
- [6] Wei, J.; Buriak, J. M.; Siuzdak, G. Desorption/ionization mass spectrometry on porous silicon. *Nature* **1999**, *399*, 243–246.
- [7] Lehmann, V.; Foll, H. Formation mechanism and properties of electrochemically etched trenches in n-type silicon. *J. Electrochem. Soc.* **1990**, *137*, 653–659.
- [8] Canham, L. T. Silicon quantum wire array fabrication by electrochemical and chemical dissolution of wafers. *Appl. Phys. Lett.* **1990**, *57*, 1046–1048.
- [9] Hochbaum, A. I.; Gargas, D.; Hwang, Y. J.; Yang, P. D. Single crystalline mesoporous silicon nanowires. *Nano Lett.* **2009**, *9*, 3550–3554.
- [10] Chazalviel, J. N. *Porous Silicon Science and Technology*; Springer: Berlin, 1995.
- [11] Chan, C. K.; Peng, H. L.; Liu, G.; McIlwrath, K.; Zhang, X. F.; Huggins, R. A.; Cui, Y. High-performance lithium battery anodes using silicon nanowires. *Nat. Nanotechnol.* **2008**, *3*, 31–35.
- [12] Tsirlina, T.; Cohen, S.; Cohen, H.; Sapir, L.; Peisach, M.; Tenne, R.; Matthaeus, A.; Tiefenbacher, S.; Jaegermann, W.; Ponomarev, E. A. et al. Growth of crystalline WSe₂ and WS₂ films on amorphous substrate by reactive (van der Waals) rheotaxy. *Sol. Energ. Mat. Sol. C.* **1996**, *44*, 457–470.
- [13] Stewart, M. P.; Buriak, J. M. Chemical and biological applications of porous silicon technology. *Adv. Mater.* **2000**, *12*, 859–869.
- [14] Holmes, J. D.; Johnston, K. P.; Doty, R. C.; Korgel, B. A. Control of thickness and orientation of solution-grown silicon nanowires. *Science* **2000**, *287*, 1471–1473.
- [15] Cui, Y.; Lieber, C. M. Functional nanoscale electronic devices assembled using silicon nanowire building blocks. *Science* **2001**, *291*, 851–853.
- [16] Smith, R. L.; Collins, S. D. Porous silicon formation mechanisms. *J. Appl. Phys.* **1992**, *71*, R1–R22.
- [17] Lehman, V. *Electrochemistry of Silicon*; Wiley-VCH: Weinheim, Germany, 2002.
- [18] Kolasinski, K. W. Silicon nanostructures from electroless electrochemical etching. *Curr. Opin. Solid State Mater. Sci.* **2005**, *9*, 73–83.
- [19] Beale, M. I. J.; Benjamin, J. D.; Uren, M. J.; Chew, N. G.; Cullis, A. G. An experimental and theoretical study of the formation and microstructure of porous silicon. *J. Cryst. Growth* **1985**, *73*, 622–636.
- [20] Uhlir, A. Electrolytic shaping of germanium and silicon. *Bell Syst. Tech. J.* **1956**, *35*, 333–347.
- [21] Quiroga-González, E.; Carstensen, J.; Glynn, C.; O'Dwyer, C.; Föll, H. Pore size modulation in electrochemically etched macroporous p-type silicon monitored by FFT impedance spectroscopy and Raman scattering. *Phys. Chem. Chem. Phys.* **2014**, *16*, 255–263.
- [22] Cullis, A. G.; Canham, L. T. Visible light emission due to quantum size effects in highly porous crystalline silicon. *Nature* **1991**, *353*, 335–338.
- [23] Canham, L. *Properties of Porous Silicon*. Institution of Electrical Engineers, 1997.
- [24] O'Dwyer, C.; Buckley, D. N.; Sutton, D.; Newcomb, S. B. Anodic formation and characterization of nanoporous InP in aqueous KOH electrolytes. *J. Electrochem. Soc.* **2006**, *153*, G1039–G1046.
- [25] O'Dwyer, C.; Buckley, D. N.; Sutton, D.; Serantoni, M.; Newcomb, S. B. An investigation by AFM and TEM of the mechanism of anodic formation of nanoporosity in n-InP in KOH. *J. Electrochem. Soc.* **2007**, *154*, H78–H85.

- [26] Tiginyanu, I.; Ursaki, V.; Monaico, E.; Foca, E.; Föll, H. Pore etching in III–V and II–VI semiconductor compounds in neutral electrolyte. *Electrochim. Solid ST.* **2007**, *10*, D127–D129.
- [27] O’Dwyer, C.; Buckley, D. N.; Newcomb, S. B. Simultaneous observation of current oscillations and porous film growth during anodization of InP. *Langmuir* **2005**, *21*, 8090–8095.
- [28] Lynch, R.; O’Dwyer, C.; Sutton, D.; Newcomb, S. B.; Buckley, D. N. Nanoporous domains in n-InP anodized in KOH. *ECS Trans.* **2007**, *6*, 355–366.
- [29] Lynch, R.; O’Dwyer, C.; Quill, N.; Nakahara, S.; Newcomb, S. B.; Buckley, D. N. Pore propagation directions and nanoporous domain shape in n-InP anodized in KOH. *J. Electrochim. Soc.* **2013**, *160*, D260–D270.
- [30] Lynch, R. P.; Quill, N.; O’Dwyer, C.; Nakahara, S.; Buckley, D. N. Propagation of nanopores during anodic etching of n-InP in KOH. *Phys. Chem. Chem. Phys.* **2013**, *15*, 15135–15145.
- [31] Sun, D.; Riley, A. E.; Cadby, A. J.; Richman, E. K.; Korlann, S. D.; Tolbert, S. H. Hexagonal nanoporous germanium through surfactant-driven self-assembly of Zintl clusters. *Nature* **2006**, *441*, 1126–1130.
- [32] Armatas, G. S.; Kanatzidis, M. G. Hexagonal mesoporous germanium. *Science* **2006**, *313*, 817–820.
- [33] Mohanan, J. L.; Arachchige, I. U.; Brock, S. L. Porous semiconductor chalcogenide aerogels. *Science* **2005**, *307*, 397–400.
- [34] Bag, S.; Trikalitis, P. N.; Chupas, P. J.; Armatas, G. S.; Kanatzidis, M. G. Porous semiconducting gels and aerogels from chalcogenide clusters. *Science* **2007**, *317*, 490–493.
- [35] Kato, S.; Kurokawa, Y.; Watanabe, Y.; Yamada, Y.; Yamada, A.; Ohta, Y.; Niwa, Y.; Hirota, M. Optical assessment of silicon nanowire arrays fabricated by metal-assisted chemical etching. *Nanoscale Res. Lett.* **2013**, *8*, 1–6.
- [36] Wen, X. M.; Van Dao, L.; Hannaford, P. Temperature dependence of photoluminescence in silicon quantum dots. *J. Phys. D: Appl. Phys.* **2007**, *40*, 3573–3578.
- [37] Li, X. Metal assisted chemical etching for high aspect ratio nanostructures: A review of characteristics and applications in photovoltaics. *Curr. Opin. Solid ST. M.* **2012**, *16*, 71–81.
- [38] Li, X. P.; Xiao, Y. J.; Bang, J. H.; Lausch, D.; Meyer, S.; Miclea, P. T.; Jung, J. Y.; Schweizer, S. L.; Lee, J. H.; Wehrspohn, R. B. Upgraded silicon nanowires by metal-assisted etching of metallurgical silicon: A new route to nanostructured solar-grade silicon. *Adv. Mater.* **2013**, *25*, 3187–3191.
- [39] Lin, V. S. Y.; Motesharei, K.; Dancil, K. P. S.; Sailor, M. J.; Ghadiri, M. R. A porous silicon-based optical interferometric biosensor. *Science* **1997**, *278*, 840–843.
- [40] Hochbaum, A. I.; Fan, R.; He, R. R.; Yang, P. D. Controlled growth of Si nanowire arrays for device integration. *Nano Lett.* **2005**, *5*, 457–460.
- [41] Li, Y. Y.; Cunin, F.; Link, J. R.; Gao, T.; Betts, R. E.; Reiver, S. H.; Chin, V.; Bhatia, S. N.; Sailor, M. J. Polymer replicas of photonic porous silicon for sensing and drug delivery applications. *Science* **2003**, *299*, 2045–2047.
- [42] Hochbaum, A. I.; Chen, R. K.; Delgado, R. D.; Liang, W. J.; Garnett, E. C.; Najarian, M.; Majumdar, A.; Yang, P. D. Enhanced thermoelectric performance of rough silicon nanowires. *Nature* **2008**, *451*, 163.
- [43] Ghossoub, M.; Valavalal, K.; Seong, M.; Azeredo, B.; Hsu, K.; Sadhu, J.; Singh, P.; Sinha, S. Spectral phonon scattering from sub-10 nm surface roughness wavelengths in metal-assisted chemically etched Si nanowires. *Nano Lett.* **2013**, *13*, 1564–1571.
- [44] Feser, J. P.; Sadhu, J. S.; Azeredo, B. P.; Hsu, K. H.; Ma, J.; Kim, J.; Seong, M.; Fang, N. X.; Li, X. L.; Ferreira, P. M. Thermal conductivity of silicon nanowire arrays with controlled roughness. *J. Appl. Phys.* **2012**, *112*, 114306.
- [45] Lim, J. W.; Hippalgaonkar, K.; Andrews, S. C.; Majumdar, A.; Yang, P. D. Quantifying surface roughness effects on phonon transport in silicon nanowires. *Nano Lett.* **2012**, *12*, 2475–2482.
- [46] Oskam, G.; Long, J. G.; Natarajan, A.; Pearson, P. C. Electrochemical deposition of metals onto silicon. *J. Phys. D: Appl. Phys.* **1998**, *31*, 1927–1949.
- [47] Dawood, M. K.; Tripathy, S.; Dolman, S. B.; Ng, T. H.; Tan, H.; Lam, J. Influence of catalytic gold and silver metal nanoparticles on structural, optical, and vibrational properties of silicon nanowires synthesized by metal-assisted chemical etching. *J. Appl. Phys.* **2012**, *112*, 073509.
- [48] Chattopadhyay, S.; Li, X. L.; Bohn, P. W. In-plane control of morphology and tunable photoluminescence in porous silicon produced by metal-assisted electroless chemical etching. *J. Appl. Phys.* **2002**, *91*, 6134–6140.
- [49] Kato, Y.; Adachi, S. Synthesis of Si nanowire arrays in AgO/HF solution and their optical and wettability properties. *J. Electrochim. Soc.* **2011**, *158*, K157–K163.
- [50] Hochbaum, A. I.; Yang, P. D. Semiconductor nanowires for energy conversion. *Chem. Rev.* **2009**, *110*, 527–546.
- [51] Peng, K. Q.; Yan, Y. J.; Gao, S. P.; Zhu, J. Synthesis of large-area silicon nanowire arrays via self-assembling nanoelectrochemistry. *Adv. Mater.* **2002**, *14*, 1164–1167.
- [52] Peng, K. Q.; Hu, J. J.; Yan, Y. J.; Wu, Y.; Fang, H.; Xu, Y.; Lee, S. T.; Zhu, J. Fabrication of single-crystalline silicon nanowires by scratching a silicon surface with catalytic metal particles. *Adv. Funct. Mater.* **2006**, *16*, 387–394.

- [53] Huang, Z. P.; Geyer, N.; Werner, P.; De Boor, J.; Gösele, U. Metal-assisted chemical etching of silicon: A review. *Adv. Mater.* **2011**, *23*, 285–308.
- [54] Li, X. Metal assisted chemical etching for high aspect ratio nanostructures: A review of characteristics and applications in photovoltaics. *Curr. Opin. Solid. St. M.* **2012**, *16*, 71–81.
- [55] Hochbaum, A. I.; Chen, R. K.; Delgado, R. D.; Liang, W. J.; Garnett, E. C.; Najarian, M.; Majumdar, A.; Yang, P. D. Enhanced thermoelectric performance of rough silicon nanowires. *Nature* **2008**, *451*, 163–167.
- [56] Zhang, M. L.; Peng, K. Q.; Fan, X.; Jie, J. S.; Zhang, R. Q.; Lee, S. T.; Wong, N. B. Preparation of large-area uniform silicon nanowires arrays through metal-assisted chemical etching. *J. Phys. Chem. C* **2008**, *112*, 4444–4450.
- [57] Li, J.; Yue, C.; Yu, Y.; Chui, Y. S.; Yin, J.; Wu, Z.; Wang, C.; Zang, Y.; Lin, W.; Li, J. et al. Si/Ge core–shell nanoarrays as the anode material for 3D lithium ion batteries. *J. Mater. Chem. A* **2013**, *1*, 14344–14349.
- [58] Li, X.; Bohn, P. W. Metal-assisted chemical etching in HF/H₂O₂ produces porous silicon. *Appl. Phys. Lett.* **2000**, *77*, 2572–2574.
- [59] Peng, K. Q.; Fang, H.; Hu, J. J.; Wu, Y.; Zhu, J.; Yan, Y. J.; Lee, S. Metal-particle-induced, highly localized site-specific etching of Si and formation of single-crystalline Si nanowires in aqueous fluoride solution. *Chem. Eur. J.* **2006**, *12*, 7942–7947.
- [60] Peng, K.; Wu, Y.; Fang, H.; Zhong, X.; Xu, Y.; Zhu, J. Uniform, axial-orientation alignment of one-dimensional single-crystal silicon nanostructure arrays. *Angew. Chem. Int. Edit.* **2005**, *44*, 2737–2742.
- [61] Teerlinck, I.; Mertens, P. W.; Schmidt, H. F.; Meuris, M.; Heyns, M. M. Impact of the electrochemical properties of silicon wafer surfaces on copper outplating from HF solutions. *J. Electrochem. Soc.* **1996**, *143*, 3323–3327.
- [62] Gorostiza, P.; Díaz, R.; Servat, J.; Sanz, F.; Morante, J. R. Atomic force microscopy study of the silicon doping influence on the first stages of platinum electroless deposition. *J. Electrochem. Soc.* **1997**, *144*, 909–914.
- [63] Tang, H.; Tu, J.; Liu, X.; Zhang, Y.; Huang, S.; Li, W.; Wang, X.; Gu, C. Self-assembly of Si/honeycomb reduced graphene oxide composite film as a binder-free and flexible anode for Li-ion batteries. *J. Mater. Chem. A* **2014**, *2*, 5834–5840.
- [64] Li, Z. C.; Zhao, L.; Diao, H. W.; Zhou, C. L.; Li, H. L.; Wang, W. J. Macroporous silicon formation on low-resistivity p-type c-Si substrate by metal-catalyzed electrochemical etching. *Int. J. Electrochem. Sci.* **2013**, *8*, 1163–1169.
- [65] Kolasinski, K. W. Etching of silicon in fluoride solutions. *Surf. Sci.* **2009**, *603*, 1904–1911.
- [66] Peng, K. Q.; Hu, J. J.; Yan, Y. J.; Wu, Y.; Fang, H.; Xu, Y.; Lee, S. T.; Zhu, J. Fabrication of single-crystalline silicon nanowires by scratching a silicon surface with catalytic metal particles. *Adv. Funct. Mater.* **2006**, *16*, 387–394.
- [67] Trucks, G. W.; Raghavachari, K.; Higashi, G. S.; Chabal, Y. J. Mechanism of HF etching of silicon surfaces: A theoretical understanding of hydrogen passivation. *Phys. Rev. Lett.* **1990**, *65*, 504–507.
- [68] Uhlig Jr, A. Electrolytic shaping of germanium and silicon. *Bell System Tech. J.* **1956**, *35*, 333–347.
- [69] Wagner, R. S.; Ellis, W. C. Vapor–liquid–solid mechanism of single crystal growth. *Appl. Phys. Lett.* **1964**, *4*, 89.
- [70] Morales, A. M.; Lieber, C. M. A laser ablation method for the synthesis of crystalline semiconductor nanowires. *Science* **1998**, *279*, 208–211.
- [71] Chan, C. K.; Peng, H. L.; Liu, G.; McIlwrath, K.; Zhang, X. F.; Huggins, R. A.; Cui, Y. High-performance lithium battery anodes using silicon nanowires. *Nature Nanotech.* **2008**, *3*, 31–35.
- [72] Ruffo, R.; Hong, S. S.; Chan, C. K.; Huggins, R. A.; Cui, Y. Impedance analysis of silicon nanowire lithium ion battery anodes. *J. Phys. Chem. C* **2009**, *113*, 11390–11398.
- [73] Wang, Y.; Lew, K. K.; Ho, T. T.; Pan, L.; Novak, S. W.; Dickey, E. C.; Redwing J. M.; Mayer, T. S. Use of phosphine as an n-type dopant source for vapor–liquid–solid growth of silicon nanowires. *Nano Lett.* **2005**, *5*, 2139–2143.
- [74] Schmidt, V.; Senz, S.; Gösele, U. Diameter-dependent growth direction of epitaxial silicon nanowires. *Nano Lett.* **2005**, *5*, 931–935.
- [75] Choi, W. K.; Liew, T. H.; Dawood, M. K.; Smith, H. I.; Thompson, C. V.; Hong, M. H. Synthesis of silicon nanowires and nanofin arrays using interference lithography and catalytic etching. *Nano Lett.* **2008**, *8*, 3799–3802.
- [76] de Boor, J.; Geyer, N.; Wittemann, J. V.; Gösele, U.; Schmidt, V. Sub-100 nm silicon nanowires by laser interference lithography and metal-assisted etching. *Nanotechnology* **2010**, *21*, 095302.
- [77] Wang, N.; Tang, Y. H.; Zhang, Y. F.; Lee, C. S.; Lee, S. T. Nucleation and growth of Si nanowires from silicon oxide. *Phys. Rev. B* **1998**, *58*, R16024–R16026.
- [78] Peng, K. Q.; Jie, J. S.; Zhang, W. J.; Lee, S. T. Silicon nanowires for rechargeable lithium-ion battery anodes. *Appl. Phys. Lett.* **2008**, *93*, 033105.
- [79] Azaredo, B. P.; Sadhu, J.; Ma, J.; Jacobs, K.; Kim, J.; Lee, K.; Eraker, J. H.; Li, X.; Sinha S.; Fang, N. et al. Silicon nanowires with controlled sidewall profile and roughness fabricated by thin-film dewetting and metal-assisted chemical etching. *Nanotechnology* **2013**, *24*, 225305.

- [80] Peng, K.; Lu, A.; Zhang, R.; Lee, S. T. Motility of metal nanoparticles in silicon and induced anisotropic silicon etching. *Adv. Funct. Mater.* **2008**, *18*, 3026–3035.
- [81] Zhang, M. L.; Peng, K. Q.; Fan, X.; Jie, J. S.; Zhang, R. Q.; Lee, S. T.; Wong, N. B. Preparation of large-area uniform silicon nanowires arrays through metal-assisted chemical etching. *J. Phys. Chem. C* **2008**, *112*, 4444–4450.
- [82] Peng, K. Q.; Fang, H.; Hu, J. J.; Wu, Y.; Zhu, J.; Yan, Y. J.; Lee, S. Metal-particle-induced, highly localized site-specific etching of Si and formation of single-crystalline Si nanowires in aqueous fluoride solution. *Chem. Eur. J.* **2006**, *12*, 7942–7947.
- [83] Lotty, O.; Petkov, N.; Georgiev, Y. M.; Holmes, J. D. Porous to nonporous transition in the morphology of metal assisted etched silicon nanowires. *Jpn. J. Appl. Phys.* **2012**, *51*, 11PE03-1.
- [84] McSweeney, W.; Lotty, O.; Mogili, N. V. V.; Glynn, C.; Geaney, H.; Tanner, D.; Holmes, J. D.; O'Dwyer, C. Doping controlled roughness and defined mesoporosity in chemically etched silicon nanowires with tunable conductivity. *J. Appl. Phys.* **2013**, *114*, 034309.
- [85] Hochbaum, A. I.; Gargas, D.; Hwang, Y. J.; Yang, P. D. Single crystalline mesoporous silicon nanowires. *Nano Lett.* **2009**, *9*, 3550–3554.
- [86] Liu, G. L.; Young, K. L.; Liao, X.; Personick, M. L.; Mirkin, C. A. Anisotropic nanoparticles as shape-directing catalysts for the chemical etching of silicon. *J. Am. Chem. Soc.* **2013**, *135*, 12196–12199.
- [87] Geyer, N.; Fuhrmann, B.; Huang, Z. P.; de Boor, J.; Leipner, H. S.; Werner, P. Model for the mass transport during metal-assisted chemical etching with contiguous metal films as catalysts. *J. Phys. Chem. C* **2012**, *116*, 13446.
- [88] Güder, F.; Yang, Y.; Küçükbayrak, U. M.; Zacharias, M. Tracing the migration history of metal catalysts in metal-assisted chemically etched silicon. *ACS Nano* **2013**, *7*, 1583–1590.
- [89] Bang, B. M.; Kim, H.; Song, H. K.; Cho, J.; Park, S. Scalable approach to multi-dimensional bulk Si anodes via metal-assisted chemical etching. *Energ. Environ. Sci.* **2011**, *4*, 5013–5019.
- [90] Chiappini, C.; Liu, X. W.; Fakhoury, J. R.; Ferrari, M. Biodegradable porous silicon barcode nanowires with defined geometry. *Adv Funct. Mater.* **2010**, *20*, 2231–2239.
- [91] Chern, W.; Hsu, K.; Chun, I. S.; de Azeredo, B. P.; Ahmed, N.; Kim, K. H.; Zuo, J. M.; Fang, N.; Ferreira, P.; Li, X. L. Nonlithographic patterning and metal-assisted chemical etching for manufacturing of tunable light-emitting silicon nanowire arrays. *Nano Lett.* **2010**, *10*, 1582–1588.
- [92] Zhong, X.; Qu, Y. Q.; Lin, Y. C.; Liao, L.; Duan, X. F. Unveiling the formation pathway of single crystalline porous silicon nanowires. *ACS Appl. Mater. Inter.* **2011**, *3*, 261–270.
- [93] Qu, Y. Q.; Liao, L.; Li, Y. J.; Zhang, H.; Huang, Y.; Duan, X. F. Electrically conductive and optically active porous silicon nanowires. *Nano Lett.* **2009**, *9*, 4539–4543.
- [94] Guo, J.; Sun, A.; Chen, X.; Wang, C.; Manivannan, A. Cyclability study of silicon–carbon composite anodes for lithium-ion batteries using electrochemical impedance spectroscopy. *Electrochim. Acta* **2011**, *56*, 3981–3987.
- [95] Lee, D. H.; Kim, Y.; Doerk, G. S.; Laborante, I.; Maboudian, R. Strategies for controlling Si nanowire formation during Au-assisted electroless etching. *J. Mater. Chem.* **2011**, *21*, 10359–10363.
- [96] Chartier, C.; Bastide, S.; Lévy-Clément, C. Metal-assisted chemical etching of silicon in HF–H₂O₂. *Electrochim. Acta* **2008**, *53*, 5509–5516.
- [97] Li, S.; Ma, W.; Zhou, Y.; Chen, X.; Xiao, Y.; Ma, M.; Zhu, W.; Wei, F. Fabrication of porous silicon nanowires by MACE method in HF/H₂O₂/AgNO₃ system at room temperature. *Nanoscale Res. Lett.* **2014**, *9*, 196.
- [98] Balasundaram, K.; Sadhu, J. S.; Shin, J. C.; Azeredo, B.; Chanda, D.; Malik, M.; Hsu, K.; Rogers, J. A.; Ferreira, P.; Sinha, S. et al. Porosity control in metal assisted chemical etching of degenerately doped silicon. *Nanotechnology* **2012**, *23*, 305304.
- [99] Liu, R.; Zhang, F.; Con, C.; Cui, B.; Sun, B. Lithography-free fabrication of silicon nanowire and nanohole arrays by metal-assisted chemical etching. *Nanoscale Res. Lett.* **2013**, *8*, 1–8.
- [100] Choi, H. J.; Baek, S.; Jang, H. S.; Kim, S. B.; Oh, B. Y.; Kim, J. H. Optimization of metal-assisted chemical etching process in fabrication of p-type silicon wire arrays. *Curr. Appl. Phys.* **2011**, *11*, S25–S29.
- [101] Lu, Y. T.; Barron, A. R. Nanopore-type black silicon anti-reflection layers fabricated by a one-step silver-assisted chemical etching. *Phys. Chem. Chem. Phys.* **2013**, *15*, 9862–9870.
- [102] Smith, Z. R.; Smith, R. L.; Collins, S. D. Mechanism of nanowire formation in metal assisted chemical etching. *Electrochim. Acta* **2013**, *92*, 139–147.
- [103] Qi, Y.; Wang, Z.; Zhang, M.; Yang, F.; Wang, X. A processing window for fabricating heavily doped silicon nanowires by metal-assisted chemical etching. *J. Phys. Chem. C* **2013**, *117*, 25090–25096.
- [104] Huang, Z. P.; Shimizu, T.; Senz, S.; Zhang, Z.; Geyer, N.; Gösele, U. Oxidation rate effect on the direction of metal-assisted chemical and electrochemical etching of silicon. *J. Phys. Chem. C* **2010**, *114*, 10683–10690.

- [105] Zuo, Z.; Cui, G.; Shi, Y.; Liu Y.; Ji, G Gold-thickness-dependent Schottky barrier height for charge transfer in metal-assisted chemical etching of silicon. *Nanoscale Res. Lett.* **2013**, *8*, 193.
- [106] Ge, S.; Jiang, K.; Lu, X.; Chen, Y.; Wang, R.; Fan, S. Orientation-controlled growth of single-crystal silicon nanowire arrays. *Adv. Mater.* **2005**, *17*, 56–61.
- [107] He, R.; Gao, D.; Fan, R.; Hochbaum, A. I.; Carraro, C.; Maboudian, R.; Yang, P. Si nanowire bridges in micro-trenches: Integration of growth into device fabrication. *Adv. Mater.* **2005**, *17*, 2098–2102.
- [108] Hochbaum, A. I.; Fan, R.; He, R.; Yang, P. Controlled growth of Si nanowire arrays for device integration. *Nano Lett.* **2005**, *5*, 457–460.
- [109] Li, X. L.; Gu, M.; Hu, S. Y.; Kennard, R.; Yan, P. F.; Chen, X. L.; Wang, C. M.; Sailor, M. J.; Zhang, J. G.; Liu, J. Mesoporous silicon sponge as an anti-pulverization structure for high-performance lithium-ion battery anodes. *Nature Commun.* **2014**, *5*, 4105.
- [110] Shimizu, T.; Xie, T.; Nishikawa, J.; Shingubara, S.; Senz, S.; Gösele, U. Synthesis of vertical high-density epitaxial Si(100) nanowire arrays on a Si(100) substrate using an anodic aluminum oxide template. *Adv. Mater.* **2007**, *19*, 917–920.
- [111] Nassiopoulou, A. G.; Gianneta, V.; Katsogridakis, C. Si nanowires by a single-step metal-assisted chemical etching process on lithographically defined areas: Formation kinetics. *Nanoscale Res. Lett.* **2011**, *6*, 597.
- [112] Chang, S. W.; Chuang, V. P.; Boles, S. T.; Ross, C. A.; Thompson, C. V. Densely packed arrays of ultra-high-aspect-ratio silicon nanowires fabricated using block-copolymer lithography and metal-assisted etching. *Adv. Funct. Mater.* **2009**, *19*, 2495–2500.
- [113] Huang, Z. P.; Zhang, X. X.; Reiche, M.; Liu, L. F.; Lee, W.; Shimizu, T.; Senz, S.; Gösele, U. Extended arrays of vertically aligned sub-10 nm diameter [100] Si nanowires by metal-assisted chemical etching. *Nano Lett.* **2008**, *8*, 3046–3051.
- [114] Huang, J.; Chiam, S. Y.; Tan, H. H.; Wang, S.; Chim, W. K. Fabrication of silicon nanowires with precise diameter control using metal nanodot arrays as a hard mask blocking material in chemical etching. *Chem. Mater.* **2010**, *22*, 4111–4116.
- [115] Huang, Z. P.; Shimizu, T.; Senz, S.; Zhang, Z.; Zhang, X. X.; Lee, W.; Geyer, N.; Gösele, U. Ordered arrays of vertically aligned [110] silicon nanowires by suppressing the crystallographically preferred <100> etching directions. *Nano Lett.* **2009**, *9*, 2519–2525.
- [116] Lotfabad, E. M.; Kalisvaart, P.; Kohandehghan, A.; Cui, K.; Kupsta, M.; Farbod B.; Mitlin, D. Si nanotubes ALD coated with TiO₂, TiN or Al₂O₃ as high performance lithium ion battery anodes. *J. Mater. Chem. A* **2014**, *2*, 2504–2516.
- [117] Cho, J. H.; Picraux, S. T. Enhanced lithium ion battery cycling of silicon nanowire anodes by template growth to eliminate silicon underlayer islands. *Nano Lett.* **2013**, *13*, 5740–5747.
- [118] Peng, K. Q.; Wu, Y.; Fang, H.; Zhong, X. Y.; Xu, Y.; Zhu, J. Uniform, axial-orientation alignment of one-dimensional single-crystal silicon nanostructure arrays. *Angew. Chem. Inter. Edit.* **2005**, *44*, 2737–2742.
- [119] Kim, J. G.; Shi, D. Q.; Park, M. S.; Jeong, G.; Heo, Y. U.; Seo, M.; Kim, Y. J.; Kim, J. H.; Dou, S. X. Controlled Ag-driven superior rate-capability of Li₄Ti₅O₁₂ anodes for lithium rechargeable batteries. *Nano Res.* **2013**, *6*, 365–372.
- [120] Chen, C. Y.; Wu, C. S.; Chou, C. J.; Yen, T. J. Morphological control of single-crystalline silicon nanowire arrays near room temperature. *Adv. Mater.* **2008**, *20*, 3811–3815.
- [121] Chen, H.; Wang, H.; Zhang, X. H.; Lee, C. S.; Lee, S. T. Wafer-scale synthesis of single-crystal zigzag silicon nanowire arrays with controlled turning angles. *Nano Lett.* **2010**, *10*, 864–868.
- [122] Bai, F.; To, W. K.; Huang, Z. Porosification-induced back-bond weakening in chemical etching of n-Si(111). *J. Phys. Chem. C* **2013**, *117*, 2203–2209.
- [123] Tsujino, K.; Matsumura, M. Morphology of nanoholes formed in silicon by wet etching in solutions containing HF and H₂O₂ at different concentrations using silver nanoparticles as catalysts. *Electrochim. Acta* **2007**, *53*, 28–34.
- [124] Tsujino, K.; Matsumura, M. Boring deep cylindrical nanoholes in silicon using silver nanoparticles as a catalyst. *Adv. Mater.* **2005**, *17*, 1045–1047.
- [125] Whittingham, M. S. Lithium batteries and cathode materials. *Chem. Rev.* **2004**, *104*, 4271–4302.
- [126] Armand, M.; Tarascon, J. M. Building better batteries. *Nature* **2008**, *451*, 652–657.
- [127] Dahn, J. R.; Zheng, T.; Liu, Y.; Xue, J. S. Mechanisms for lithium insertion in carbonaceous materials. *Science* **1995**, *270*, 590–593.
- [128] Winter, M.; Besenhard, J. O.; Spahr, M. E.; Novak, P. Insertion electrode materials for rechargeable lithium batteries. *Adv. Mater.* **1998**, *10*, 725–763.
- [129] Linden, D.; Reddy, T. B. *Handbook of Batteries*, 3rd edn; McGraw-Hill, 2002.
- [130] Liu, C.; Li, F.; Ma, L. P.; Cheng, H. M. Advanced materials for energy storage. *Adv. Mater.* **2010**, *22*, E28–E62.

- [131] Yang, Y.; Jeong, S.; Hu, L. B.; Wu, H.; Lee, S. W.; Cui, Y. Transparent lithium-ion batteries. *P. Natl. Acad. Sci. USA* **2011**, *108*, 13013–13018.
- [132] Rolison, D. R.; Long, J. W.; Lytle, J. C.; Fischer, A. E.; Rhodes, C. P.; McEvoy, T. M.; Bourga, M. E.; Lubers, A. M. Multifunctional 3D nanoarchitectures for energy storage and conversion. *Chem. Soc. Rev.* **2009**, *38*, 226–252.
- [133] Beaulieu, L. Y.; Eberman, K. W.; Turner, R. L.; Krause, L. J.; Dahn, J. R. Colossal reversible volume changes in lithium alloys. *Electrochem. Solid ST.* **2001**, *4*, A137–A140.
- [134] Huggins, R. A. Lithium alloy negative electrodes. *J. Power Sources* **1999**, *81*, 13–19.
- [135] Wen, C. J.; Huggins, R. A. Chemical diffusion in intermediate phases in the lithium–silicon system. *J. Solid State Chem.* **1981**, *37*, 271–278.
- [136] Boukamp, B. A.; Lesh, G. C.; Huggins, R. A. All-solid lithium electrodes with mixed conductor matrix. *J. Electrochem. Soc.* **1981**, *128*, 725–729.
- [137] Shodai, T.; Okada, S.; Tobishima, S. I.; Yamaki, J. I. Study of $\text{Li}_{3-x}\text{M}_x\text{N}$ (M: Co, Ni or Cu) system for use as anode material in lithium rechargeable cells. *Solid State Ionics* **1996**, *86–88, Part 2*, 785–789.
- [138] Poizot, P.; Laruelle, S.; Gruegeon, S.; Dupont, L.; Tarascon, J. M. Nano-sized transition-metal oxides as negative-electrode materials for lithium-ion batteries. *Nature* **2000**, *407*, 496–499.
- [139] Su, D. W.; Dou, S. X.; Wang, G. X. Mesocrystal Co_3O_4 nanoplatelets as high capacity anode materials for Li-ion batteries. *Nano Res.* **2014**, *7*, 794–803.
- [140] Kim, S. W.; Lee, H. W.; Muralidharan, P.; Seo, D. H.; Yoon, W. S.; Kim, D. K.; Kang, K. Electrochemical performance and *ex situ* analysis of ZnMn_2O_4 nanowires as anode materials for lithium rechargeable batteries. *Nano Res.* **2011**, *4*, 505–510.
- [141] Vlad, A.; Reddy, A. L. M.; Ajayan, A.; Singh, N.; Gohy, J. F.; Melinte, S.; Ajayan, P. M. Roll up nanowire battery from silicon chips. *P. Natl. Acad. Sci. USA* **2012**, *109*, 15168–15173.
- [142] Li, J.; Dahn, J. R. An *in situ* X-ray diffraction study of the reaction of Li with crystalline Si. *J. Electrochem. Soc.* **2007**, *154*, A156–A161.
- [143] Beaulieu, L. Y.; Hatchard, T. D.; Bonakdarpour, A.; Fleischauer, M. D.; Dahn, J. R. Reaction of Li with alloy thin films studied by *in situ* AFM. *J. Electrochem. Soc.* **2003**, *150*, A1457–A1464.
- [144] Zhang, X. W.; Patil, P. K.; Wang, C. S.; Appleby, A. J.; Little, F. E.; Cocke, D. L., Electrochemical performance of lithium ion battery, nano-silicon-based, disordered carbon composite anodes with different microstructures. *J. Power Sources* **2004**, *125*, 206–213.
- [145] Maranchi, J. P.; Hepp, A. F.; Evans, A. G.; Nuhfer, N. T.; Kumta, P. N. Interfacial properties of the a-Si/Cu: Active–inactive thin-film anode system for lithium-ion batteries. *J. Electrochem. Soc.* **2006**, *153*, A1246–A1253.
- [146] Maranchi, J. P.; Hepp, A. F.; Kumta, P. N. High capacity, reversible silicon thin-film anodes for lithium-ion batteries. *Electrochem. Solid ST.* **2003**, *6*, A198–A201.
- [147] Park, M. S.; Lee, Y. J.; Rajendran, S.; Song, M. S.; Kim, H. S.; Lee, J. Y. Electrochemical properties of Si/Ni alloy–graphite composite as an anode material for Li-ion batteries. *Electrochim. Acta* **2005**, *50*, 5561–5567.
- [148] Szczech, J. R.; Jin, S. Nanostructured silicon for high capacity lithium battery anodes. *Energ. Environ. Sci.* **2011**, *4*, 56–72.
- [149] Jung, H. J.; Park, M.; Yoon, Y. G.; Kim, G. B.; Joo, S. K. Amorphous silicon anode for lithium-ion rechargeable batteries. *J. Power Sources* **2003**, *115*, 346–351.
- [150] Ohara, S.; Suzuki, J.; Sekine, K.; Takamura, T. A thin film silicon anode for Li-ion batteries having a very large specific capacity and long cycle life. *J. Power Sources* **2004**, *136*, 303–306.
- [151] Obrovac, M. N.; Krause, L. J. Reversible cycling of crystalline silicon powder. *J. Electrochem. Soc.* **2007**, *154*, A103–A108.
- [152] Ryu, J. H.; Kim, J. W.; Sung, Y. E.; Oh, S. M. Failure modes of silicon powder negative electrode in lithium secondary batteries. *Electrochem. Solid ST.* **2004**, *7*, A306–A309.
- [153] Liu, X. H.; Zhong, L.; Huang, S.; Mao, S. X.; Zhu, T.; Huang, J. Y. Size-dependent fracture of silicon nanoparticles during lithiation. *ACS Nano* **2012**, *6*, 1522–1531.
- [154] McDowell, M. T.; Lee, S. W.; Harris, J. T.; Korgel, B. A.; Wang, C. M.; Nix, W. D.; Cui, Y. *In situ* TEM of two-phase lithiation of amorphous silicon nanospheres. *Nano Lett.* **2013**, *13*, 758–764.
- [155] Chon, M. J.; Sethuraman, V. A.; McCormick, A.; Srinivasan, V.; Guduru, P. R. Real-time measurement of stress and damage evolution during initial lithiation of crystalline silicon. *Phys. Rev. Lett.* **2011**, *107*, 045503.
- [156] Ge, M.; Fang, X.; Rong, J.; Zhou, C. Review of porous silicon preparation and its application for lithium-ion battery anodes. *Nanotechnology* **2013**, *24*, 422001.
- [157] Yang, H.; Huang, S.; Huang, X.; Fan, F. F.; Liang, W. T.; Liu, X. H.; Chen, L. Q.; Huang, J. Y.; Li, J.; Zhu, T. et al. Orientation-dependent interfacial mobility governs the anisotropic swelling in lithiated silicon nanowires. *Nano Lett.* **2012**, *12*, 1953–1958.
- [158] Ge, M. Y.; Rong, J. P.; Fang, X.; Zhou, C. W. Porous doped silicon nanowires for lithium ion battery anode with long cycle life. *Nano Lett.* **2012**, *12*, 2318–2323.

- [159] Armstrong, M. J.; O'Dwyer, C.; Macklin, W. J.; Holmes, J. D. Evaluating the performance of nanostructured materials as lithium-ion battery electrodes. *Nano Res.* **2014**, *7*, 1–62.
- [160] Ohara, S.; Suzuki, J.; Sekine, K.; Takamura, T. Li insertion/extraction reaction at a Si film evaporated on a Ni foil. *J. Power Sources* **2003**, *119*, 591–596.
- [161] Uehara, M.; Suzuki, J.; Tamura, K.; Sekine, K.; Takamura, T. Thick vacuum deposited silicon films suitable for the anode of Li-ion battery. *J. Power Sources* **2005**, *146*, 441–444.
- [162] Takamura, T.; Ohara, S.; Uehara, M.; Suzuki, J.; Sekine, K. A vacuum deposited Si film having a Li extraction capacity over 2,000 mAh/g with a long cycle life. *J. Power Sources* **2004**, *129*, 96–100.
- [163] Li, F.; Yue, H.; Yang, Z.; Li, X.; Qin, Y.; He, D. Flexible free-standing graphene foam supported silicon films as high capacity anodes for lithium ion batteries. *Mater. Lett.* **2014**, *128*, 132–135.
- [164] Zhao, G. Y.; Meng, Y. F.; Zhang, N. Q.; Sun, K. N. Electrodeposited Si film with excellent stability and high rate performance for lithium-ion battery anodes. *Mater. Lett.* **2012**, *76*, 55–58.
- [165] Goldman, J. L.; Cason, M. W.; Wetzel, D. J.; Vieker, H.; Beyer, A.; Gölzhäuser, A.; Gewirth, A. A.; Nuzzo, R. G. Directed transport as a route to improved performance in micropore-modified encapsulated multilayer silicon electrodes. *J. Electrochem. Soc.* **2013**, *160*, A1746–A1752.
- [166] Hatchard, T. D.; Topple, J. M.; Fleischauer, M. D.; Dahn, J. R. Electrochemical performance of SiAlSn films prepared by combinatorial sputtering. *Electrochem. Solid-State Lett.* **2003**, *6*, A129–A132.
- [167] Hwang, C. M.; Lim, C. H.; Park, J. W. Evaluation of Si/Ge multi-layered negative film electrodes using magnetron sputtering for rechargeable lithium ion batteries. *Thin Solid Films* **2011**, *519*, 2332–2338.
- [168] Wilson, A. M.; Dahn, J. R. Lithium insertion in carbons containing nanodispersed silicon. *J. Electrochem. Soc.* **1995**, *142*, 326–332.
- [169] Li, H.; Huang, X. J.; Chen, L. Q.; Wu, Z. G.; Liang, Y. A high capacity nano-Si composite anode material for lithium rechargeable batteries. *Electrochim. Solid ST.* **1999**, *2*, 547–549.
- [170] Li, H.; Huang, X. J.; Chen, L. Q.; Zhou, G. W.; Zhang, Z.; Yu, D. P.; Mo, Y. J.; Pei, N. The crystal structural evolution of nano-Si anode caused by lithium insertion and extraction at room temperature. *Solid State Ionics* **2000**, *135*, 181–191.
- [171] Lee, H. Y.; Lee, S. M. Graphite–FeSi alloy composites as anode materials for rechargeable lithium batteries. *J. Power Sources* **2002**, *112*, 649–654.
- [172] Weydanz, W. J.; Wohlfahrt-Mehrens, M.; Huggins, R. A. A room temperature study of the binary lithium–silicon and the ternary lithium–chromium–silicon system for use in rechargeable lithium batteries. *J. Power Sources* **1999**, *81*, 237–242.
- [173] Hwang, S. M.; Lee, H. Y.; Jang, S. W.; Lee, S. M.; Lee, S. J.; Baik, H. K.; Lee, J. Y. Lithium insertion in SiAg powders produced by mechanical alloying. *Electrochem. Solid-State Lett.* **2001**, *4*, A97–A100.
- [174] Kim, I. S.; Blomgren, G. E.; Kumta, P. N. Nanostructured Si/TiB₂ composite anodes for Li-ion batteries. *Electrochem. Solid-State Lett.* **2003**, *6*, A157–A161.
- [175] Dimov, N.; Kugino, S.; Yoshio, M. Carbon-coated silicon as anode material for lithium ion batteries: Advantages and limitations. *Electrochim. Acta* **2003**, *48*, 1579–1587.
- [176] Yang, J.; Wang, B. F.; Wang, K.; Liu, Y.; Xie, J. Y.; Wen, Z. S. Si/C composites for high capacity lithium storage materials. *Electrochim. Solid ST.* **2003**, *6*, A154–A156.
- [177] Beaulieu, L. Y.; Hewitt, K. C.; Turner, R. L.; Bonakdarpour, A.; Abdo, A. A.; Christensen, L.; Eberman, K. W.; Krause, L. J.; Dahn, J. R. The electrochemical reaction of Li with amorphous Si–Sn alloys. *J. Electrochem. Soc.* **2003**, *150*, A149–A156.
- [178] Kim, J. W.; Ryu, J. H.; Lee, K. T.; Oh, S. M. Improvement of silicon powder negative electrodes by copper electroless deposition for lithium secondary batteries. *J. Power Sources* **2005**, *147*, 227–233.
- [179] Kim, H. S.; Chung, K. Y.; Cho, L. W. Effect of carbon-coated silicon/graphite composite anode on the electrochemical properties. *B. Korean Chem. Soc.* **2008**, *29*, 1965–1968.
- [180] Dong, H.; Ai, X. P.; Yang, H. X. Carbon/Ba–Fe–Si alloy composite as high capacity anode materials for Li-ion batteries. *Electrochim. Commun.* **2003**, *5*, 952–957.
- [181] Jung, Y. S.; Lee, K. T.; Oh, S. M. Si–carbon core–shell composite anode in lithium secondary batteries. *Electrochim. Acta* **2007**, *52*, 7061–7067.
- [182] Xu, Y. H.; Yin, G. P.; Ma, Y. L.; Zuo, P. J.; Cheng, X. Q. Nanosized core/shell silicon@carbon anode material for lithium ion batteries with polyvinylidene fluoride as carbon source. *J. Mater. Chem.* **2010**, *20*, 3216–3220.
- [183] Kim, H.; Cho, J. Superior lithium electroactive mesoporous Si@carbon core–shell nanowires for lithium battery anode material. *Nano Lett.* **2008**, *8*, 3688–3691.
- [184] Magasinski, A.; Dixon, P.; Hertzberg, B.; Kvit, A.; Ayala, J.; Yushin, G. High-performance lithium-ion anodes using a hierarchical bottom-up approach. *Nat. Mater.* **2010**, *9*, 353–358.
- [185] Ge, M. Y.; Rong, J. P.; Fang, X.; Zhang, A. Y.; Lu, Y. H.; Zhou, C. W. Scalable preparation of porous silicon nanoparticles and their application for lithium-ion battery anodes.

- Nano Res.* **2013**, *6*, 174–181.
- [186] Arie, A. A.; Chang, W.; Lee, J. K. Electrochemical characteristics of semi conductive silicon anode for lithium polymer batteries. *J. Electroceram.* **2010**, *24*, 308–312.
- [187] Kong, M. H.; Noh, J. H.; Byun, D. J.; Lee, J. K. Electrochemical characteristics of phosphorus doped silicon and graphite composite for the anode materials of lithium secondary batteries. *J. Electroceram.* **2009**, *23*, 376–381.
- [188] Garnett, E. C.; Tseng, Y. C.; Khanal, D. R.; Wu, J. Q.; Bokor, J.; Yang, P. D. Dopant profiling and surface analysis of silicon nanowires using capacitance–voltage measurements. *Nat. Nanotechnol.* **2009**, *4*, 311–314.
- [189] Xu, W. L.; Vegunta, S. S. S.; Flake, J. C. Surface-modified silicon nanowire anodes for lithium-ion batteries. *J. Power Sources* **2011**, *196*, 8583–8589.
- [190] Xu, W. L.; Flake, J. C. Composite silicon nanowire anodes for secondary lithium-ion cells. *J. Electrochem. Soc.* **2010**, *157*, A41–A45.
- [191] Huang, J. Y.; Zhong, Li.; Wang, C. M.; Sullivan, J. P.; Xu, W.; Zhang, L. Q.; Mao, S. X.; Hudak, N. S.; Liu, X. H.; Sabramanian, A. et al. *In situ* observation of the electrochemical lithiation of a single SnO₂ nanowire electrode. *Science* **2010**, *330*, 1515–1520.
- [192] Huang, R.; Zhu, J. Silicon nanowire array films as advanced anode materials for lithium-ion batteries. *Mater. Chem. Phys.* **2010**, *121*, 519–522.
- [193] Zhang, Q. F.; Zhang, W. X.; Wan, W. H.; Cui, Y.; Wang, E. G. Lithium insertion in silicon nanowires: An *ab initio* study. *Nano Lett.* **2010**, *10*, 3243–3249.
- [194] Peng, B.; Cheng, F. Y.; Tao, Z. L.; Chen, J. Lithium transport at silicon thin film: Barrier for high-rate capability anode. *J. Chem. Phys.* **2010**, *133*, 034701.
- [195] Long, B. R.; Chan, M. K. Y.; Greeley, J. P.; Gewirth, A. A. Dopant modulated Li insertion in Si for battery anodes: Theory and experiment. *J. Phys. Chem. C* **2011**, *115*, 18916–18921.
- [196] Rousselot, S.; Gauthier, M.; Mazouzi, D.; Lestriez, B.; Guyomard, D.; Roué, L. Synthesis of boron-doped Si particles by ball milling and application in Li-ion batteries. *J. Power Sources* **2012**, *202*, 262–268.
- [197] McSweeney, W.; Lotty, O.; Glynn, C.; Geaney, H.; Holmes, J. D.; O'Dwyer, C. The influence of carrier density and doping type on lithium insertion and extraction processes at silicon surfaces. *Electrochim. Acta* **2014**, *135*, 356–367.
- [198] Wang, G. X.; Sun, L.; Bradhurst, D. H.; Zhong, S.; Dou, S. X.; Liu, H. K. Innovative nanosize lithium storage alloys with silica as active centre. *J. Power Sources* **2000**, *88*, 278–281.
- [199] Zuo, P.; Yang, W.; Cheng, X.; Yin, G. Enhancement of the electrochemical performance of silicon/carbon composite material for lithium ion batteries. *Ionics* **2011**, *17*, 87–90.
- [200] Graetz, J.; Ahn, C. C.; Yazami, R.; Fultz, B. Highly reversible lithium storage in nanostructured silicon. *Electrochem. Solid ST.* **2003**, *6*, A194–A197.
- [201] Takamura, T.; Uehara, M.; Suzuki, J.; Sekine, K.; Tamura, K. High capacity and long cycle life silicon anode for Li-ion battery. *J. Power Sources* **2006**, *158*, 1401–1404.
- [202] Green, M.; Fielder, E.; Scrosati, B.; Wachtler, M.; Moreno, J. S. Structured silicon anodes for lithium battery applications. *Electrochem. Solid-State Lett.* **2003**, *6*, A75–A79.
- [203] Xu, W. L.; Flake, J. C. Composite silicon nanowire anodes for secondary lithium-ion cells. *J. Electrochem. Soc.* **2010**, *157*, A41–A45.
- [204] Kang, K.; Lee, H. S.; Han, D. W.; Kim, G. S.; Lee, D.; Lee, G.; Kang, Y. M.; Jo, M. H. Maximum Li storage in Si nanowires for the high capacity three-dimensional Li-ion battery. *Appl. Phys. Lett.* **2010**, *96*, 053110.
- [205] Chan, C. K.; Patel, R. N.; O'Connell, M. J.; Korgel, B. A.; Cui, Y. Solution-grown silicon nanowires for lithium-ion battery anodes. *ACS Nano* **2010**, *4*, 1443–1450.
- [206] Wan, J.; Kaplan, A. F.; Zheng, J.; Han, X.; Chen, Y.; Weadock, N. J.; Faenza, N.; Lacey, S.; Li, T.; Guo, J. et al. Two dimensional silicon nanowalls for lithium ion batteries. *J Mater. Chem. A* **2014**, *2*, 6051–6057.
- [207] Cui, L. F.; Yang, Y.; Hsu, C. M.; Cui, Y., Carbon–silicon core–shell nanowires as high capacity electrode for lithium ion batteries. *Nano Lett.* **2009**, *9*, 3370–3374.
- [208] Cui, L. F.; Ruffo, R.; Chan, C. K.; Peng, H. L.; Cui, Y., Crystalline–amorphous core–shell silicon nanowires for high capacity and high current battery electrodes. *Nano Lett.* **2009**, *9*, 491–495.
- [209] Xie, J.; Wang, G.; Huo, Y.; Zhang, S.; Cao, G.; Zhao, X. Nanostructured silicon spheres prepared by a controllable magnesiothermic reduction as anode for lithium ion batteries. *Electrochim. Acta* **2014**, *135*, 94–100.
- [210] Wu, H.; Chan, G.; Choi, J. W.; Ryu, I.; Yao, Y.; McDowell, M. T.; Lee, S. W.; Jackson, A.; Yang, Y.; Hu, L. B. et al. Stable cycling of double-walled silicon nanotube battery anodes through solid-electrolyte interphase control. *Nat. Nanotechnol.* **2012**, *7*, 310–315.
- [211] Liu, N.; Lu, Z. D.; Zhao, J.; McDowell, M. T.; Lee, H. W.; Zhao, W. T.; Cui, Y. A pomegranate-inspired nanoscale design for large-volume-change lithium battery anodes. *Nat. Nanotechnol.* **2014**, *9*, 187–192.
- [212] Hu, L. B.; Wu, H.; Hong, S. S.; Cui, L. F.; McDonough, J. R.; Bohy, S.; Cui, Y. Si nanoparticle-decorated Si nanowire

- networks for Li-ion battery anodes. *Chem. Commun.* **2011**, *47*, 367–369.
- [213] Huang, R.; Fan, X.; Shen, W. C.; Zhu, J. Carbon-coated silicon nanowire array films for high-performance lithium-ion battery anodes. *Appl. Phys. Lett.* **2009**, *95*, 133119.
- [214] Yang, Y.; McDowell, M. T.; Jackson, A.; Cha, J. J.; Hong, S. S.; Cui, Y. New nanostructured Li₂S/silicon rechargeable battery with high specific energy. *Nano Lett.* **2010**, *10*, 1486–1491.
- [215] Osiak, M.; Geaney, H.; Armstrong, E.; O'Dwyer, C. Structuring materials for lithium-ion batteries: Advancements in nanomaterial structure, composition, and defined assembly on cell performance. *J. Mater. Chem. A* **2014**, *2*, 9433–9460.
- [216] Foell, H.; Hartz, H.; Ossei-Wusu, E.; Carstensen, J.; Riemenschneider, O. Si nanowire arrays as anodes in Li ion batteries. *Phys. Status Solidi RRL.* **2010**, *4*, 4–6.
- [217] Díaz, C.; Valenzuela, M. L.; Bravo, D.; Lavayen, V.; O'Dwyer, C., Synthesis and characterization of cyclotriphosphazene containing silicon as single solid state precursors for the formation of silicon/phosphorus nanostructured materials. *Inorg. Chem.* **2008**, *47*, 11561–11569.
- [218] Diaz, C.; Valenzuela, M. L.; Ushak, S.; Lavayen, V.; O'Dwyer, C. Nanostructured silicon-containing materials derived from solid-state pyrolysis of sililated polyphosphazene derivatives. *J. Nanosci. Nanotechnol.* **2009**, *9*, 1825–1831.
- [219] Wagner, M. W.; Schmied, M.; Preishuber-Pflugl, P.; Stelzer, F.; Besenhard, J. O.; Winter, M. In *10th International Meeting of Lithium Batteries*, Como, Italy, 2000.
- [220] Wu, M.; Sabisch, J. E. C.; Song, X.; Minor, A. M.; Battaglia, V. S.; Liu, G. In situ formed Si nanoparticle network with micron-sized Si particles for lithium-ion battery anodes. *Nano Lett.* **2013**, *13*, 5397–5402.
- [221] Jeong, Y. K.; Kwon, T. W.; Lee, I.; Kim, T. S.; Coskun, A.; Choi, J. W. Hyperbranched β-cyclodextrin polymer as an effective multidimensional binder for silicon anodes in lithium rechargeable batteries. *Nano Lett.* **2014**, *14*, 864–870.
- [222] Hwa, Y.; Kim, W. S.; Hong, S. H.; Sohn, H. J. High capacity and rate capability of core–shell structured nano-Si/C anode for Li-ion batteries. *Electrochim. Acta* **2012**, *71*, 201–205.
- [223] Kuksenko, S.; Konovalenko, I. Silicon nanopowder as active material for hybrid electrodes of lithium-ion batteries. *Russ. J. Appl. Chem.* **2011**, *84*, 1179–1187.
- [224] Lai, J.; Guo, H. J.; Wang, Z. X.; Li, X. H.; Zhang, X. P.; Wu, F. X.; Yue, P., Preparation and characterization of flake graphite/silicon/carbon spherical composite as anode materials for lithium-ion batteries. *J. Alloys Compd.* **2012**, *530*, 30–35.
- [225] Chan, C. K.; Ruffo, R.; Hong, S. S.; Huggins, R. A.; Cui, Y. Structural and electrochemical study of the reaction of lithium with silicon nanowires. *J. Power Sources* **2009**, *189*, 34–39.
- [226] Chan, C. K.; Zhang, X. F.; Cui, Y. High capacity Li ion battery anodes using Ge nanowires. *Nano Lett.* **2008**, *8*, 307–309.
- [227] Wu, Y.; Yang, P. Direct observation of vapor–liquid–solid nanowire growth. *J. Am. Chem. Soc.* **2001**, *123*, 3165–3166.
- [228] Du, N.; Zhang, H.; Fan, X.; Yu, J. X.; Yang, D. R. Large-scale synthesis of silicon arrays of nanowire on titanium substrate as high-performance anode of Li-ion batteries. *J. Alloys Compd.* **2012**, *526*, 53–58.
- [229] Cho, J. H.; Picraux, S. T. Enhanced lithium ion battery cycling of silicon nanowire anodes by template growth to eliminate silicon underlayer islands. *Nano Lett.* **2013**, *13*, 5740–5747.
- [230] Gohier, A.; Laik, B.; Pereira-Ramos, J. P.; Cojocaru, C. S.; Tran-Van, P. Influence of the diameter distribution on the rate capability of silicon nanowires for lithium-ion batteries. *J. Power Sources* **2012**, *203*, 135–139.
- [231] Perea, D. E.; Hemesath, E. R.; Schwalbach, E. J.; Lensch-Falk, J. L.; Voorhees, P. W.; Lauhon, L. J. Direct measurement of dopant distribution in an individual vapour–liquid–solid nanowire. *Nat. Nanotechnol.* **2009**, *4*, 315–319.
- [232] Chockla, A. M.; Klavetter, K. C.; Mullins, C. B.; Korgel, B. A. Tin-seeded silicon nanowires for high capacity li-ion batteries. *Chem. Mater.* **2012**, *24*, 3738–3745.
- [233] He, R. R.; Gao, D.; Fan, R.; Hochbaum, A. I.; Carraro, C.; Maboudian, R.; Yang, P. D. Si nanowire bridges in microtrenches: Integration of growth into device fabrication. *Adv. Mater.* **2005**, *17*, 2098–2102.
- [234] Heitsch, A. T.; Akhavan, V. A.; Korgel, B. A., Rapid SFLS synthesis of Si nanowires using Trisilane with in situ alkyl-amine passivation. *Chem. Mat.* **2011**, *23*, 2697–2699.
- [235] Bogart, T. D.; Lu, X.; Korgel, B. A. Precision synthesis of silicon nanowires with crystalline core and amorphous shell. *Dalton Trans.* **2013**, *42*, 12675–12680.
- [236] Mullane, E.; Kennedy, T.; Geaney, H.; Dickinson, C.; Ryan, K. M. Synthesis of tin catalyzed silicon and germanium nanowires in a solvent–vapor system and optimization of the seed/nanowire interface for dual lithium cycling. *Chem. Mater.* **2013**, *25*, 1816–1822.
- [237] Geaney, H.; Kennedy, T.; Dickinson, C.; Mullane, E.; Singh, A.; Laffir, F.; Ryan, K. M. High density growth of indium seeded silicon nanowires in the vapor phase of a high boiling point solvent. *Chem. Mater.* **2012**, *24*, 2204–2210.
- [238] Zhao, X.; Rui, X.; Zhou, W.; Tan, L.; Yan, Q.; Lu, Z.; Hng, H. H. Growth of Si nanowires in porous carbon with

- enhanced cycling stability for Li-ion storage. *J. Power Sources* **2014**, *250*, 160–165.
- [239] Gu, M.; Wang, Z. G.; Connell, J. G.; Perea, D. E.; Lauhon, L. J.; Gao, F.; Wang, C. M. Electronic origin for the phase transition from amorphous Li_xSi to crystalline $\text{Li}_{15}\text{Si}_4$. *ACS Nano* **2013**, *7*, 6303–6309.
- [240] Bogart, T. D.; Lu, X. T.; Gu, M.; Wang, C. M.; Korgel, B. A. Enhancing the lithiation rate of silicon nanowires by the inclusion of tin. *RSC Adv.* **2014**, *4*, 42022–42028.
- [241] Yin, J. T.; Wada, M.; Yamamoto, K.; Kitano, Y.; Tanase, S.; Sakai, T. Micrometer-scale amorphous Si thin-film electrodes fabricated by electron-beam deposition for Li-ion batteries. *J. Electrochem. Soc.* **2006**, *153*, A472–A477.
- [242] Ohara, S.; Suzuki, J. J.; Sekine, K.; Takamura, T. Attainment of high rate capability of Si film as the anode of Li-ion batteries. *Electrochemistry* **2003**, *71*, 1126–1128.
- [243] Limthongkul, P.; Jang, Y. I.; Dudney, N. J.; Chiang, Y. M., Electrochemically-driven solid-state amorphization in lithium–silicon alloys and implications for lithium storage. *Acta Mater.* **2003**, *51*, 1103–1113.
- [244] Kim, G.; Jeong, S.; Shin, J. H.; Cho, J.; Lee, H. 3D amorphous silicon on nanopillar copper electrodes as anodes for high-rate lithium-ion batteries. *ACS Nano* **2014**, *8*, 1907–1912.
- [245] Li, X. P.; Xiao, Y. J.; Yan, C. L.; Zhou, K. Y.; Miclea, P. T.; Meyer, S.; Schweizer, S. L.; Sprafke, A.; Lee, J. H.; Wehrspohn, R. B. Self-purification model for metal-assisted chemical etching of metallurgical silicon. *Electrochim. Acta* **2014**, *138*, 476–480.
- [246] Xu, Y. H.; Yin, G. P.; Ma, Y. L.; Zuo, P. J.; Cheng, X. Q. Nanosized core/shell silicon@carbon anode material for lithium ion batteries with polyvinylidene fluoride as carbon source. *J. Mater. Chem.* **2010**, *20*, 3216–3220.
- [247] Lee, K. T.; Jung, Y. S.; Oh, S. M. Synthesis of tin-encapsulated spherical hollow carbon for anode material in lithium secondary batteries. *J. Am. Chem. Soc.* **2003**, *125*, 5652–5653.
- [248] Zhang, T.; Gao, J.; Zhang, H. P.; Yang, L. C.; Wu, Y. P.; Wu, H. Q. Preparation and electrochemical properties of core–shell Si/SiO nanocomposite as anode material for lithium ion batteries. *Electrochem. Commun.* **2007**, *9*, 886–890.
- [249] Wang, D.; Yang, Z.; He, D. Electrochemical performances of nanorod structured $\text{Si}_{1-x}\text{Ge}_x$ anodes. *Mater. Lett.* **2014**, *128*, 163–166.
- [250] Tu, J.; Hu, L.; Wang, W.; Hou, J.; Zhu, H.; Jiao, S. *In-situ* synthesis of silicon/polyaniline core/shell and its electrochemical performance for lithium-ion batteries. *J. Electrochem. Soc.* **2013**, *160*, A1916–A1921.
- [251] Wang, J. Z.; Du, N.; Zhang, H.; Yu, J. X.; Yang, D. R. $\text{Cu}-\text{Si}_{1-x}\text{Ge}_x$ core–shell nanowire arrays as three-dimensional electrodes for high-rate capability lithium-ion batteries. *J. Power Sources* **2012**, *208*, 434–439.
- [252] Luo, J.; Zhao, X.; Wu, J.; Jang, H. D.; Kung, H. H.; Huang, J. Crumpled graphene-encapsulated Si nanoparticles for lithium ion battery anodes. *J. Phys. Chem. Lett.* **2012**, *3*, 1824–1829.
- [253] Chen, X. L.; Gerasopoulos, K.; Guo, J. C.; Brown, A.; Wang, C. S.; Ghodssi, R.; Culver, J. N. A patterned 3D silicon anode fabricated by electrodeposition on a virus-structured current collector. *Adv. Funct. Mater.* **2011**, *21*, 380–387.
- [254] Song, T.; Xia, J. L.; Lee, J. H.; Lee, D. H.; Kwon, M. S.; Choi, J. M.; Wu, J.; Doo, S. K.; Chang, H.; Park, W. I. Arrays of sealed silicon nanotubes as anodes for lithium ion batteries. *Nano Lett.* **2010**, *10*, 1710–1716.
- [255] Hwang, C. M.; Lim, C. H.; Park, J. W. Evaluation of Si/Ge multi-layered negative film electrodes using magnetron sputtering for rechargeable lithium ion batteries. *Thin Solid Films* **2011**, *519*, 2332–2338.
- [256] Bang, B. M.; Kim, H.; Lee, J. P.; Cho, J.; Park, S. Mass production of uniform-sized nanoporous silicon nanowire anodes via block copolymer lithography. *Energy Environ. Sci.* **2011**, *4*, 3395–3399.
- [257] Wu, H.; Cui, Y. Designing nanostructured Si anodes for high energy lithium ion batteries. *Nano Today* **2012**, *7*, 414–429.
- [258] Wang, B.; Li, X.; Qiu, T.; Luo, B.; Ning, J.; Li, J.; Zhang, X.; Liang, M.; Zhi, L. High volumetric capacity silicon-based lithium battery anodes by nanoscale system engineering. *Nano Lett.* **2013**, *13*, 5578–5584.
- [259] Chadwick, E. G.; Mogili, V.; O’Dwyer, C.; Moore, J.; Fletcher, J.; Laffir, F.; Armstrong, G.; Tanner, D. A. Compositional characterization of metallurgical grade silicon and porous silicon nanospunge particles. *RSC Adv.* **2013**, *3*, 19393–19402.
- [260] Chakrapani, V.; Rusli, F.; Filler, M. A.; Kohl, P. A., Silicon nanowire anode: Improved battery life with capacity-limited cycling. *J. Power Sources* **2012**, *205*, 433–438.
- [261] Liu, X. H. et al. Ultrafast electrochemical lithiation of individual Si nanowire anodes. *Nano Lett.* **2011**, *11*, 2251–2258.
- [262] Ge, M.; Rong, J.; Fang, X.; Zhang, A.; Lu, Y.; Zhou, C. Scalable preparation of porous silicon nanoparticles and their application for lithium-ion battery anodes. *Nano Res.* **2013**, *6*, 174–181.
- [263] Zhou, X. S.; Yin, Y. X.; Cao, A. M.; Wan, L. J.; Guo, Y. G. Efficient 3D conducting networks built by graphene sheets

- and carbon nanoparticles for high-performance silicon anode. *ACS Appl. Mater. Interfaces* **2012**, *4*, 2824–2828.
- [264] Zhang, P.; Wang, L.; Xie, J.; Su, L.; Ma, C. A. Micro/nano-complex-structure SiO_x -PANI-Ag composites with homogeneously-embedded Si nanocrystals and nanopores as high-performance anodes for lithium ion batteries. *J. Mater. Chem. A* **2014**, *2*, 3776–3782.
- [265] Tao, H. C.; Fan, L. Z.; Qu, X. Facile synthesis of ordered porous Si@C nanorods as anode materials for Li-ion batteries. *Electrochim. Acta* **2012**, *71*, 194–200.
- [266] Zhu, Y.; Liu, W.; Zhang, X.; He, J.; Chen, J.; Wang, Y.; Cao, T. Directing silicon-graphene self-assembly as a core/shell anode for high-performance lithium-ion batteries. *Langmuir* **2013**, *29*, 744–749.
- [267] Shen, J.; Ahn, D.; Raj, R. C-rate performance of silicon oxycarbide anodes for Li^+ batteries enhanced by carbon nanotubes. *J. Power Sources* **2011**, *196*, 2875–2878.
- [268] Guo, C.; Wang, D.; Liu, T.; Zhu J.; Lang, X. A three dimensional $\text{SiO}_x/\text{C}@\text{RGO}$ nanocomposite as a high energy anode material for lithium-ion batteries. *J. Mater. Chem. A* **2014**, *2*, 3521–3527.
- [269] Bogart, T. D.; Oka, D.; Lu, X.; Gu, M.; Wang, C.; Korgel, B. A. Lithium ion battery performance of silicon nanowires with carbon skin. *ACS Nano* **2013**, *8*, 915–922.
- [270] Wu, H.; Cui, Y. Designing nanostructured Si anodes for high energy lithium ion batteries. *Nano Today* **2012**, *7*, 414–429.
- [271] Magasinki, A.; Dixon, P.; Hertzberg, B.; Kvit, A.; Ayala, J.; Yushin, G. High-performance lithium-ion anodes using a hierarchical bottom-up approach. *Nat. Mater.* **2010**, *9*, 353.
- [272] Thakur, M.; Sinsabaugh, S.; Isaacson, M. J.; Wong, M. S.; Biswal, S. L. Inexpensive method for producing macroporous silicon particulates (MPSPs) with pyrolyzed polyacrylonitrile for lithium ion batteries. *Sci. Rep.* **2012**, *2*, 795.
- [273] Xiao, X.; Liu, X.; Wang, L.; Zhao, H.; Hu, Z.; He, X.; Li, Y. LiCoO_2 nanoplates with exposed (001) planes and high rate capability for lithium-ion batteries. *Nano Res.* **2012**, *5*, 395–401.